DEVELOPMENT OF NEW TECHNIQUES FOR SUBMILLIMETRE WAVE SPECTROSCOPY OF SOLIDS

CHE LOI MOK

A Thesis submitted for the internal Degree of Doctor of Philosophy (Ph D) in the Faculty of Science, University of London

March 1981

A B S T R A C T

A selection of free-standing fine-wire grids with different wire spacings have been wound for use as spectroscopic components at millimetre and submillimetre wavelengths. The performance of the grids has been investigated extensively and found to be in good overall agreement, both qualitatively and quantitatively, with calculations made using a least-squares method developed by Beunen. Where discrepancies occur they are attributed to the effect of uneven spacing of the wires.

A microcomputing system based on the Z80 8-bit microprocessor has been built to provide data acquisition and Fourier transformation for a Fourier spectrometer.

Measurements have been made of the far infrared optical constants of KCl and KBr crystals by dispersive Fourier transform spectroscopy at temperatures in the range 7-300K using instruments equipped with both mylar and wire grid beam dividers. The results have been used to calculate the dielectric functions and the anharmonic self energy functions of the $q \approx 0$ transverse optic modes in these crystals. The frequencies of the transversive optic (TO) and longitudinal optic (LO) modes determined from the dielectric functions are in good agreement with the accepted values, and in the case of KBr, the frequency-dependence of the anharmonic self-energy functions determined at room temperature is in good agreement with calculations made by Bruce.

ACKNOWLEDGEMENTS

I am sincerely grateful to Dr. T. J. Parker for supervising this research project and for his constant help, advice and encouragement. He has enlightened me through many discussions and guided me in numerous problems that I have laid before him.

Many thanks go to Dr. W. G. Chambers for his consistent help in many aspects of the computational work, and to Dr. G. A. Gledhill for thoughtful discussions from which I have greatly benefited.

I am greatly indebted to Dr. A. E. Costley of the National Physical Laboratory for the use of a wire grid winder, help with making wire grids and for providing facilities for making measurements on wire grids using an HCN laser.

I also thank Mr. P. Heaver, the Chief Technician, Messrs J. Oliver and W. Howard of the Physics workshop, and M. Curati and T. Brooks of the Electronic workshop for their invaluable assistance, and Mr. R. Collins for the difficult task of crystal polishing.

I am grateful for the support given to me by my family during the course of my studies.

I would finally like to acknowledge financial support from the Science Research Council in the form of a CASE award, from the National Physical Laboratory as the Co-operating Body on this CASE project, and from Westfield College in the form of a four months Studentship to complete this work.

CONTENTS

CHAPTER 1

INTRODUCTION

The technique of Fourier transform spectroscopy was initiated by Michelson [1880] when he first invented his interferometer. Since then the technique has been developed by many physicists, who have used it in many different applications.

With the advent of the computer age Fourier transform spectroscopy (FTS) using the Michelson type interferometer has become an extremely popular tool and has been used to measure the power spectra of numerous solids, liquids and gases.

One particular disadvantage of conventional power FTS is that it does not produce phase information. Hence, the phase spectrum has to be obtained by a Kramers-Kronig (KK) analysis of the power spectrum. However, the method is inadequate for studies where accurate phase values are required over a wide spectral range.

In recent years a new technique known as dispersive Fourier transform spectroscopy (DFTS) has been developed. The main difference in DFTS is that the specimen is placed in the optical path in one arm of the interferometer, and this gives the complex reflectivity or transmittivity, i.e. both amplitude and phase spectra. The optical constants can then be determined directly without using a KK analysis.

An outline discussion of the general theory of FTS is presented in Chapter 2, but detailed descriptions can readily be found in various books [eg. Bell 1972, Chamberlain 1979]. The technique of DFTS is described in Chapter 3, where the term complex insertion loss is

discussed. The techniques described are mainly those applicable to solid state measurements, and the relationships between the complex insertion loss and the optical constants for three types of configuration are also derived.

In most interferometers, a dielectric beam divider is normally used, but this has the limitation of poor performance in the low frequency spectral region. However, the introduction of polarising interferometry [Martin and Puplett 1970] has improved the performance of instruments in this region. The use of free-standing wire grids as beam dividers has removed the main draw-back of dielectric beam dividers, i.e. the interference fringes caused by the two interfaces. If a polarising modulation system is also used, then the Bessel function envelope of the phase modulation system is removed. Thus, this optimises the performance of the interferometer to the point where it is limited by the source and the detector.

As this involves the application of wire grids in the far infrared, it is important to understand the behaviour of these components. The performance of these grids has therefore been studied, and a general description of a theory based on the least-squares method is presented in Chapter 4. The least-squares method was first proposed by Davies [1973], and further developed by Beunen [1976] for application to wire grids. In order to verify the results of the theoretical calculations, a set of wire grids were wound from 10 μm and 5 μm diameter tungsten wires with wire spacings of 30-65 μm, and 25, 50 and 100 μm, respectively.

In the case of 10 μm wire grids, measurements have been made on a set of grids with spacings in the range 30-65 μm by using an HCN laser (ν =29.7 cm^{-1}). Calculations of the transmission coefficients were

also produced for comparison with the special case of normal incidence, with the electric vector, $\underset{\sim}{E}$, parallel to the wire direction, $\underset{\sim}{S}$ (i.e. $\underset{\sim}{E} \| \underset{\sim}{S}$) The next step in the investigation was to make a comparison of calculated and measured power transmission coefficients and phase spectra for the grids wound from 10 μm diameter tungsten wire with spacings in the range 35-55 μm for the special cases of normal incidence with $\underset{\sim}{E} \| \underset{\sim}{S}$ and $\underset{\sim}{E} \perp \underset{\sim}{S}$.

By improving the winding technique, wire grids of 5 μm diameter tungsten wire have been made. A selection of these grids with spacings of 25, 50, and 100 μm have been measured by using DFTS for comparison with calculated transmission coefficients and phase spectra for the special case of normal incidence with $\underset{\sim}{E} \| \underset{\sim}{S}$ and $\underset{\sim}{E} \perp \underset{\sim}{S}$. The experimental and theoretical results were in good overall agreement both qualitatively and quantitatively, and are presented in Chapter 7.

The technique of DFTS has been used by a number of workers [Bell 1965, Chamberlain et al 1965, etc] to make measurements on solids, liquids and gases at ambient temperature. The technique has further been developed to extend the measurements below room temperature. Instruments have been built by Parker et al [1978], who have performed DFTS studies down to 80K using a single pass instrument. However, for the reflection instrument [Parker et al 1978b], measurements down to 7K have been made successfully. The description of these two instruments and the general problems affecting the performance of these instruments are discussed in Chapter 5.

One important associated component which has to be used with all types of Fourier transform spectrometer is an electronic computer. The computer is needed for the numerical Fourier transformation and other associated data analysis. In the last few years, the introduction of

microprocessors has been revolutionary in the electronic world. Because of their compactness in size and programmability, they have been used in many applications where computing power is beneficial. A microcomputing system based on an 8-bit microprocessor has been built and used with a Fourier spectrometer. The system has been used to look after all the data acquisition and perform the Fourier transformation plus other data analysis. The system has provided a reasonable computing facility, and is described in Chapter 6.

The main application of the interferometers mentioned above is for measurements of the optical constants of solids. In principle, DFTS is the simplest way of determining optical constants in the far infrared. With the transmission instrument specimens can be measured with operating temperatures down to 80k, but with the reflection instrument measurements were extended to 7K. With a combination of transmission and reflection techniques, measurements over the spectral range 20-350 cm^{-1} have thus been made with good accuracy over a wide range of operating temperatures. Measurements of the optical constants of KCl and KBr crystals have been made, and the corresponding dielectric functions for each crystal are presented in Chapter 7.

The results for KBr obtained above were used for the determination of the frequency dependence of the real and imaginary parts of the anharmonic self-energy of the tranverse optic mode in the temperature range 300 - 100k. The room temperature measurements of the damping function are shown to be in good agreement with calculations by Bruce [1973].

CHAPTER 2

FOURIER TRANSFORM SPECTROSCOPY

2.1 INTRODUCTION

In most infrared measurements a black-body source of broad-band thermal radiation is employed. The power per unit frequency interval from such a source is inherently small and so an interferometer which makes optimum use of the energy available becomes more favourable than a grating spectrometer. In the interferometer the radiation is not divided up into quasi-monochromatic components by a grating or prism before or after traversal of a specimen, but instead the interferometer acts in such a way as to encode the spectrum as a function of the optical path difference between the interfering beams. An interferogram is recorded in the form of detected signal as a function of optical path difference in the interferometer. The spectrum is then recovered from the interference function by the process of Fourier transformation, hence the name Fourier transform spectrometry. The derivation of the basic equation of the relationship between the spectrum and the interferogram is described in this chapter. The terms resolution, apodization, aliasing, Fellgett and Jacquinot advantage are also defined and discussed. In the last section of this chapter the technique of polarising interferometry is also discussed.

2.2 THE BASIC INTEGRAL FOR FOURIER TRANSFORM SPECTROSCOPY

The physical operation of the interferometer can be understood easily if we consider a beam of monochromatic radiation (frequency ν or wavelength λ) incident upon the interferometer (see fig.2.1). For simplicity we can regard this beam as divided into two equal partial beams which are recombined after a phase delay. If the phase delay in the interferometer is zero, the partial beams recombine constructively and the detector measures the resulting intensity. If the phase difference is changed by π radians (optical path difference $\lambda/2$) the returning partial beams will recombine destructively, and the detector will measure no signal. In fact, as optical path difference varies the detector will measure a cosinusoidally varying intensity. Different monochromatic components will give rise to cosinusoidal intensity variations at the detector which are in step at zero path difference but are out of step as optical path difference changes. The complicated interferogram pattern built up from a band spectrum of radiation is uniquely related to the spectral distribution of energy by a Fourier transformation.

Consider a partial beam (e.g. in one arm of a Michelson interferometer) which travels a distance which exceeds that travelled by the beam in the other arm by an amount δx, which we call the optical path difference. By assuming the interferometer to be symmetrical and evacuated, then, because of the path difference δx, the two beams arrive at the detector with a phase difference $2\pi\nu\delta x$ for any component ν and show interference which is governed by this delay. The electric field from the two arms can be expressed as

$$E_1(x) = \int_{-\infty}^{\infty} f(\nu)\ \exp\ (2\ i\pi\nu\ x)\ d\nu$$

and $$E_2(x) = \int_{-\infty}^{\infty} f(\nu)\ \exp\ [2\ i\pi\nu\ (x+\delta x)]\ d\nu \qquad (2.1)$$

where x is the parameter defining position in the interferometer arms.

The principle of linear superposition can be applied to define the resultant field of the recombined waves in terms of the amplitude $f(\nu)$ [Bell 1972].

The power at the detector is

$$I(x)\ d\nu = P(\nu)\ d\nu + P(\nu)\ \cos(2\pi\nu\delta x)\ d\nu \qquad (2.2)$$

for each spectral component of power $P(\nu)\ d\nu$ in the interval ν to $\nu+d\nu$, and we also assume that the contribution from each arm is the same. i.e. $P(\nu)d\nu$

When the source is strictly monochromatic and of a wave-number ν_o, then the amplitude from each arm is A_o, so that

$$I(x) = A_o^2\ [\ 1 + \cos(\ 2\pi\nu_o\ \delta x)]$$
$$= 2\ A_o^2\ \cos^2(\ \pi\nu_o\delta x)$$

is the interference function. It has the familiar form of cosine fringes, which extend to infinite values of δx without change in magnitude. If however, the source is of finite but small spectral width $\Delta\nu$ the fringes are still basically cosinusiodal and of period
The interference between components from either arm of the interferometer is now constructive at $\delta x=0$, but becomes increasingly destructive as δx increases. This has the effect of modulating the fringes whose magnitude falls to zero at about $\delta x = \Delta\nu^{-1}$.

If the source has a broad bandwidth, such as is the case for most spectroscopic measurements, all components are in phase at x=0, but

the detected intensity fluctuates rapidly to zero as δx is increased. The detected power is given by adding all the components represented individually by equation (2.2)

$$I(x) = \int_{-\infty}^{\infty} P(\nu)\, d\nu + \int_{-\infty}^{\infty} P(\nu) \cos(2\pi\nu\delta x)\, d\nu \qquad (2.4)$$

When $\delta x=0$, we have

$$I(0) = 2\int_{0}^{\infty} P(\nu)\, d\nu \qquad (2.5)$$

so that equation (2.4) becomes

$$I(x) = \frac{1}{2} I(0) + \int_{-\infty}^{\infty} P(\nu) \cos(2\pi\nu\delta x)\, d\nu \qquad (2.6)$$

for the interference function of the interferometer. If we write $F(x)=I(x)-1/2\ I(0)$, then

$$F(x) = \int_{0}^{\infty} P(\nu) \cos(2\pi\nu x)\, d\nu \qquad (2.7)$$

where $F(x)$ is the recorded function of the interferogram. This shows that the interferogram is related to the spectrum by a cosine Fourier integral. This relation may, by the use of the Fourier inversion theorem, be written as

$$P(\nu) = \int_{0}^{\infty} F(x) \cos(2\pi\nu x)\, dx \qquad (2.8)$$

which shows how the power spectrum may be calculated by the operation of Fourier transformation on the recorded interferogram $F(x)$.

2.3 RESOLUTION

Consider a purely monochromatic source which has a power distribution

$$P(\nu) = P_o \delta(\nu - \nu_o) \tag{2.9}$$

where P_o is the power of the line, and $\delta(\nu - \nu_o)$ is the Dirac delta function. From equ(2.7) it follows that the interferogram produced by this line is

$$I(x) = \int_o^\infty P_o \delta(\nu - \nu_o) \cos(2\pi\nu x)\, d\nu = P \cos(2\pi\nu_o x) \tag{2.10}$$

Due to the mechanical limitations of the Michelson interferometer, it is obviously impossible to record the interferogram to infinite path difference, and in practice we are restricted to a maximum displacement, D, of the moving mirror. Normally, double sided interferograms are recorded and hence we truncate the Fourier integral within the limits $\pm L$ where $L = D/2$. Then the recorded spectrum will be

$$P(\nu) = \int_{-L}^{L} P_o \cos(2\pi\nu_o x) \cos(2\pi\nu x)\, dx$$

$$= P_o L \left[\frac{\sin[2\pi(\nu+\nu_o)L]}{2\pi(\nu+\nu_o)L} + \frac{\sin[2\pi(\nu-\nu_o)L]}{2\pi(\nu-\nu_o)L} \right] \tag{2.11}$$

The first term in the expression is very small when compared with the second. Thus $P(\nu)$ can be expressed as

$$P(\nu) \approx P_o L \frac{\sin[2\pi(\nu-\nu_o)L]}{2\pi(\nu-\nu_o)L}, \tag{2.12}$$

$$= P_o L \operatorname{sinc}[2\pi(\nu-\nu_o)L]$$

This is a sinc function which has its first zero when

$$2\pi(\nu - \nu_0)L = \pm\pi \quad \text{or} \quad \nu = \nu_0 \pm \frac{1}{2L} \tag{2.13}$$

Notice that the major feature of the recovered spectrum is a peak with width $\Delta\nu = 1/L$.

This value $\Delta\nu$ may be taken as a measure of the resolution of the interferometer. However, there does not seem to be a precise definition of the resolution of a Michelson interferometer, although the resolution is inversely proportional to the maximum path difference.

One possible definition of resolution of the interferometer is obtained by the term "half-width", which is defined as the width of a line at half of its peak value. From equation(2.12) the intensity drops to half of its peak value at $2\pi(\nu - \nu_0)L = 0.607\pi$. Hence the full half width is $\approx 1.21\pi$, so we obtain the resolution

$$\Delta\nu = \frac{1.21}{2L} \tag{2.14}$$

Another possible definition is the Rayleigh criterion [Bell 1972] which defines the resolution in terms of the separation of two lines of equal intensity. If we consider that each of the recovered lines is described by a sinc function, then we can say that

$$\Delta\nu = \frac{1}{2L} \tag{2.15}$$

As the first and second definitions differ by only 20%, we shall use the simpler expression as a definition of the resolution achieved in an unapodized interferogram.

2.4 APODIZATION

The basic Fourier transform integrals have infinite limits for the optical path difference but the experimental limits are finite, and this truncation produces false sidelobes on the transformed spectra. The false sidelobes look like part of the spectrum, so modification must be made to the computation to either remove them or reduce their magnitude. The correction procedure for modifying the basic Fourier transform integral is called "apodization". To achieve this, the interferogram is usually multiplied by a function called the apodizing function.

To begin the discussion of apodization, first consider a monochromatic source. The interferogram produced by it is shown by equation (2.10), and the transformed spectrum obtained by taking a finite length of this is given by equation(2.12) i.e.

$$P(\nu) = 2 P_o L \operatorname{sinc} Z \quad \text{where} \quad Z = 2\pi(\nu - \nu_o)L \qquad (2.16)$$

Fig 2.2 shows a plot of the spectrum of a monochromatic source modified by a finite maximum path L, i.e. sinc Z. The sinc Z function is an approximation of the monochromatic line. The sidelobes drop about 22% below zero and that is rather large. One can tolerate the central peak of finite width as an approximation to an infinitely narrow band-width, but the sidelobes would appear as false sources of energy at nearby wavelengths.

If an apodizing function f(x) is introduced into the calculation of the Fourier integral to give the computed apodized spectrum, then

$$P(\nu) = \int_{-L}^{L} f(x)\ I(x)\ \cos(2\pi\nu x)\ dx \qquad (2.17)$$

is a closer approximation to the true spectrum than the unapodized one, i.e.

$$P(\nu) = \int_{-L}^{L} I(x) \cos(2\pi\nu x)\, dx \qquad (2.18)$$

Suppose one tries a triangular function for which $f(x) = 1 - |x|/L$, then we have

$$P(\nu) = P_0 \int_{-L}^{L} (1-|x|/L) \cos(2\pi\nu x) \cos(2\pi\nu_0 x)\, dx$$

$$P_0 \int_{-L}^{L} (1-|x|/L) \cos(2\pi(\nu-\nu_0) x)\, dx$$

$$= 2P_0\left\{1-\cos[2\pi(\nu-\nu_0)L]\right\} \Big/ \left[2\pi(\nu-\nu_0)\right]^2 L \qquad (2.19)$$

$$= P_0 L \operatorname{sinc}^2(Z/2) \qquad \text{where} \quad Z = 2\pi(\nu-\nu_0)L$$

as one can see from fig. 2.2, the sidelobes for equation (2.19) are reduced. The peaks of the sidelobes are reduced by a factor of about four. The width is increased somewhat, but not seriously. So one can modify the interferogram of a monochromatic source by multiplying it with the apodizing function $(1-|x|/L)$, knowing that we will obtain a spectrum which is a more acceptable approximation to the perfect monochromatic source. I have been considering triangular apodization. However, trapezoidal, Gaussian, cosine etc., functions are also used for apodization [Bell 1972].

2.5 THE JACQUINOT AND FELLGETT ADVANTAGES

The Jacquinot advantage [Girard & Jacquinot 1967] is that an interferometer, being an instrument possessing circular symmetry, has an angular admission advantage over a conventional spectrometer which employs slits and consequently has no such symmetry. When prism, grating and interference spectrometers are compared at equal resolving power, the radiant throughput of the interference spectrometer is much higher than that of the grating spectrometer.

The Fellgett advantage [Fellgett 1958] arises as a direct consequence of the fact that in an interferometer the whole of the spectral band is observed for the whole of the duration of the experiment, whereas in a grating spectrometer the spectral elements are observed sequentially for short periods which sum to give the total time of the experiment.

Suppose one is interested in measuring a broad spectrum between wave numbers ν_1 and ν_2 with a resolution $\delta\nu$. The number of spectral elements M in the broad band is

$$M = (\nu_2 - \nu_1)/\delta\nu = \Delta\nu/\delta\nu \qquad (2.20)$$

If a grating spectrometer is being used, each small band of width $\delta\nu$ can be observed for a time T/M, where T is the total time required for a scan from ν_1 to ν_2. The integrated signal received in a small band $\delta\nu$ is proportional to T/M. If the noise is random and independent of the signal level the noise should be proportional to $(T/M)^{1/2}$. Thus, for a grating instrument, the signal to noise ratio would be

$$(S/N)_g \propto (T/M)^{1/2} \qquad (2.21)$$

The interferometer detects in the broad band $\nu_1 - \nu_2$ all small bands of width $\delta\nu$ all the time, so the integrated signal in a small element $\delta\nu$ is proportional to T. The noise is proportional to $T^{1/2}$. Thus, for an interferometer, the signal to noise ratio would be

$$(S/N)_I \propto T^{1/2} \tag{2.22}$$

With the same proportionality constant for both cases, the ratio of $(S/N)_I$ for the interferometer to $(S/N)_g$ for the grating instrument is

$$(S/N)_I / (S/N)_g = M^{1/2} \tag{2.23}$$

where M is the number of spectral elements of width $\delta\nu$ in the broad band $\nu_1 - \nu_2$. Therefore, an interferometer is capable of recording a spectrum at a higher signal to noise ratio than a grating spectrometer in a given time interval, or alternatively it can record the spectrum at the same signal to noise ratio in a shorter time.

2.6 ALIASING

In most measurements in interferometric spectroscopy, the method for carrying out the numerical Fourier transformation of the interferograms is by sampling the interferogram at equal intervals of path difference. The reason for this practice is that the

interferogram is not a simple analytic function and the Fourier transformation has to be carried out in a finite time using an electronic computer. The computing program uses the Cooley-Tukey algorithm [Cooley et al 1965] which requires sampling points at regular intervals. For this reason the integration of the function is replaced by a summation. The concept of an infinite one-dimensional array of delta functions is extremely useful for the representation of the sampling function. The symbol "Shah" is used for the sampling function and is given by [Chamberlain 1979]

$$\text{Ш}(x) = \sum_{m=-\infty}^{\infty} \delta(x-m) \tag{2.24}$$

or, more generally

$$\text{Ш}(x/b) = \sum_{m=-\infty}^{\infty} b\,\delta(x-mb) \tag{2.25}$$

and multiplication of a function F(x) by Ш(x) effectively samples it at equal intervals. i.e.

$$F(x)\,\text{Ш}(x) = \sum_{m=-\infty}^{\infty} F(m) \tag{2.26}$$

The Fourier transform of the sampling function is especially interesting and important as the shah symbol is its own Fourier transform. Let

$$\begin{aligned} F(\nu) &= \int_{-\infty}^{\infty} \text{Ш}(x)\, \exp(-2\pi i \nu x)\, dx \\ &= \sum_{m=-\infty}^{\infty} \int_{-\infty}^{\infty} \delta(x-m)\, \exp(-2\pi i \nu x)\, dx \end{aligned} \tag{2.27}$$

By employing the definition of the Dirac delta function, one will have

$$F(\nu) = \sum_{m=-\infty}^{\infty} \exp(-2\pi i \nu m) \qquad (2.28)$$

Using Euler's formula

$$\sum_{m=-\infty}^{\infty} \exp(-2i\pi\nu m) = \sum_{m=-\infty}^{\infty} \cos(2\pi\nu m) - i \sum_{m=-\infty}^{\infty} \sin(2\pi\nu m) \qquad (2.29)$$

The second term in the right hand side of the equation will be zero, then

$$\sum_{m=-\infty}^{\infty} \exp(-2i\pi\nu m) = \sum_{m=-\infty}^{\infty} \cos(2\pi\nu m) \qquad (2.30)$$

For the cosine function, as ν is varied one would be summing over so many terms (infinite number) that when is not equal to an integer the cosine terms would essentially be adding with random phase and amplitude. As ν is varied, every time this value equals an integer, the sum over m would have an infinite, positive value. So this is just another shah function in terms of the Dirac delta function, then

$$\mathcal{F}\{\text{Ш}(x)\} = \sum_{m=-\infty}^{\infty} \delta(\nu-m) = \text{Ш}(\nu) \qquad (2.31)$$

$$\therefore f(\nu) = \text{Ш}(\nu)$$

While for $\text{Ш}(x/b)$

$$f(\nu) = \sum_{m=-\infty}^{\infty} \text{Ш}(x/b) \exp(-2\pi i \nu x)\, dx$$

$$= \sum_{m=-\infty}^{\infty} b\, \delta(x-mb) \exp(-2\pi i \nu x)\, dx$$

$$= \sum_{m=-\infty}^{\infty} b \exp(-2\pi i \nu mb) \qquad (2.32)$$

$$= \sum_{m=-\infty}^{\infty} b\,\delta(b\nu - m) = b\,\text{Ш}(b\nu)$$

From equations (2.31) and (2.32) it follows that the Fourier pairs for the shah function will be [see fig. 2.3]

$$\begin{aligned} &\text{Ш}(x) \rightleftharpoons \text{Ш}(\nu) \\ &\text{Ш}(x/b) \rightleftharpoons b\,\text{Ш}(b\nu) \end{aligned} \qquad (2.33)$$

The convolution of a function F(x) with the sampling comb gives a function

$$F(x) * \text{Ш}(x) = \sum_{m=-\infty}^{\infty} F(x) * \delta(x-m) = \sum_{m=-\infty}^{\infty} F(x-m) \qquad (2.34)$$

which is just the original function repeated at equal intervals to infinity in both positive and negative directions.

If we have an interferogram F(x) with the sampling function $\text{Ш}(x/\delta x)$ then the Fourier transform of this will be

$$\begin{aligned} &\int_{-\infty}^{\infty} F(x)\,\text{Ш}(x/\delta x)\,\exp(-2\pi i \nu x)\,dx \\ &\quad = \delta x\,\text{Ш}(\delta x\,\nu) * F(x) \\ &\quad = \sum_{m=-\infty}^{\infty} \delta(\nu - m/\delta x) * F(\nu) = \sum_{m=-\infty}^{\infty} F(\nu - m\,\delta\nu) \end{aligned} \qquad (2.35)$$

where $\delta\nu = 1/\delta x$.

Thus if we compute the inverse Fourier transform of the sampled interferogram, we obtain the complete spectrum every time ν equals $m\,\delta\nu$ for all integers m, i.e., we have a duplicate spectrum starting at $m\,\delta\nu$.

Due to this phenomenon the positions of the repeated spectra depend on the magnitude of δx. The repeated spectra will be well separated from the first order spectrum if δx is very small, i.e. $\delta \nu$ is very large. However, if δx is large then $\delta \nu$ becomes small, and overlapping between the real spectrum and the repeated spectra will occur. An example of the problem of the aliasing effect is shown in fig. 2.4.

In order to separate the spectra, $\delta \nu$ has to be large enough so that the negative imaged ν spectrum does not overlap the maximum frequency of the real spectrum. Then we obtain the condition as

$$\Delta \nu \geq 2 \nu_{max}$$

or (2.36)

$$\Delta x \leq 1/2 \nu_{max}$$

where ν_{max} is the maximum frequency of the measured spectrum and Δx is the step length. Thus, for a given step interval there is an upper band frequency limit if one wishes to avoid the problem of overlapping or aliasing.

2.7 POLARISING INTERFEROMETRY

In conventional interferometers dielectric thin film beam dividers are used. These are usually made of Mylar (Polyethylene terephthalate) and are stretched taut on a metal frame which locates precisely in the interferometer. Since the beam divider has parallel sides, the phenomenon of multiple internal reflection occurs. The destructive and constructive interference from these two surfaces

introduces a response envelope for the interferometer [Bell 1972]. Thus the thickness of the beam divider must be chosen to optimise the throughput energy in the spectral region of interest. By the use of thicker and thicker mylar the low frequency performance of the instrument may be improved, but the bandwidth of the first order interference fringe progressively narrows. Consequently, such dielectric beam dividers are far from ideal for long wavelength measurements below about 15 cm^{-1}.

To improve the performance of the interferometer in the long wavelength region polarised interferometric spectrometry was developed [Martin & Puplett 1970]. Instead of using a dielectric beam divider, a free-standing fine-wire grid is used as the beam divider, and this gives a large improvement in the long wavelength response of the interferometer. A schematic diagram of a Martin and Puplett instrument is shown in fig. 2.5.

To enable one to understand the principle of operation of such an interferometer, take a monochromatic source, with the E-vector of the polarisers P1 and P2 normal to the paper as shown in fig. 2.5, with unit vectors P. The electric field passing through the polariser P1 is

$$\underset{\sim}{E}(t) = a \cos(2\pi\nu ct)\ \hat{P} \qquad (2.37)$$

where a is the amplitude, and ν is the frequency.

The beam divider (BD) is orientated to give a projected angle of 45° to the vertical with respect to radiation incident from the polariser P1. Hence, the radiation which passes along the arm A of the interferometer is produced by reflection from the beam divider, and

$$\underset{\sim}{E}_a(t) = \frac{a}{\sqrt{2}} \cos(2\pi\nu ct + \delta_a)\ \hat{t} \qquad (2.38)$$

where $\hat{t}$ is a unit vector paralled to the wires of the grid. The value $\sqrt{2}$ comes from the fact that the unit vector $\hat{t}$ is at 45° with respect to the unit vector P. However, the radiation which passes along the arm B of the interferometer is that transmitted by the beam divider:

$$\underset{\sim}{E}_b(t) = \frac{a}{\sqrt{2}} \cos(2\pi\nu ct + \delta_b)\ \hat{n} \qquad (2.39)$$

where $\hat{n}$ is a unit vector normal to the wires of the grid, i.e. perpendicular to the unit vector $\hat{t}$. The roof top mirrors at the ends of both arms act as rotators for the electric vector of the incident radiation. That is, the electric vector of the radiation reflected from such a mirror will be rotated through 90° with respect to the incoming radiation. Therefore, the radiation reflected from arm A of the interferometer will be fully transmitted through the beam divider, and the radiation from arm B will be completely reflected from the beam divider. Thus both beams of the radiation will combine in the region X in the diagram, i.e. before reaching the polariser P2. Thus the electric field at X is

$$\underset{\sim}{E}(t) = \frac{a}{\sqrt{2}} \cos(2\pi\nu ct + \delta_a)\ \hat{t} + \frac{a}{\sqrt{2}} \cos(2\pi\nu ct + \delta_b)\ \hat{n} \qquad (2.40)$$

However, the unit vectors $\hat{t}$ and $\hat{n}$ are perpendicular to each other. Therefore, the two partial beams do not yet interfere, so the polariser P2 is needed to produce interference. The polarising vector of the polariser P2 is given by

$$\hat{P} = \frac{1}{\sqrt{2}}\hat{t} + \frac{1}{\sqrt{2}}\hat{n} \qquad (2.41)$$

Thus the electric field leaving the polariser P2 is

$$|E_o| = \underset{\sim}{E} \cdot \underset{\sim}{P} = \frac{a}{2}[\cos(2\pi\nu ct + \delta_a) + \cos(2\pi\nu ct + \delta_a)]$$

$$= a \cos(2\pi\nu ct + D) \cos\frac{\Delta}{2} \qquad (2.42)$$

where δ_a and δ_b are the phase shifts for radiation travelling along arms A and B respectively. D is the mean of δ_a and δ_b and Δ is the difference between the delays of the two arms, i.e.

$$\delta_a - \delta_b = 2\pi\nu x \quad ,$$

where x is the path difference. Thus the emergent intensity is

$$I_p = \langle |E_o|^2 \rangle = \frac{a^2}{2}\cos^2\frac{\Delta}{2} = \frac{a^2}{4}(1 + \cos\Delta) \quad . \qquad (2.43)$$

As one can see, the intensity depends on the path difference between the two arms, i.e. an interferogram of a monochromatic line will have a modulation of 1/2 of the input intensity on a background level of $a^2/4$. One interesting phenomenon pointed out by Martin and Puplett [1970] is that if one turns the polariser P2 through 90°, where the polarising vector changes to

$$\hat{P}' = \frac{1}{\sqrt{2}}\hat{t} - \frac{1}{\sqrt{2}}\hat{n} \qquad (2.44)$$

the electric field after the polariser will be

$$|E_o'| = \underset{\sim}{E} \cdot \underset{\sim}{\hat{P}}' = \frac{a}{2}[\cos(2\pi\nu ct + \delta_a) - \cos(2\pi\nu ct + \delta_b)]$$

$$= -a \sin(2\pi\nu ct + D) \sin\frac{\Delta}{2} \qquad (2.45)$$

Thus the emergent intensity is

$$I_{p'} = \langle |E_o'|^2 \rangle = \frac{a^2}{2}\sin^2\frac{\Delta}{2} = \frac{a^2}{4}(1 - \cos\Delta) \qquad (2.46)$$

So by switching the polarisation of the beam back and forth through 90°, i.e. modulating the polarisation of the radiation, the output will oscillate about a true zero level, that is, it will have no constant

off-set. Thus

$$I_p - I_{p'} = I \cos \Delta \qquad (2.47)$$

This forms the basis of the technique of polarisation modulation which will be discussed later.

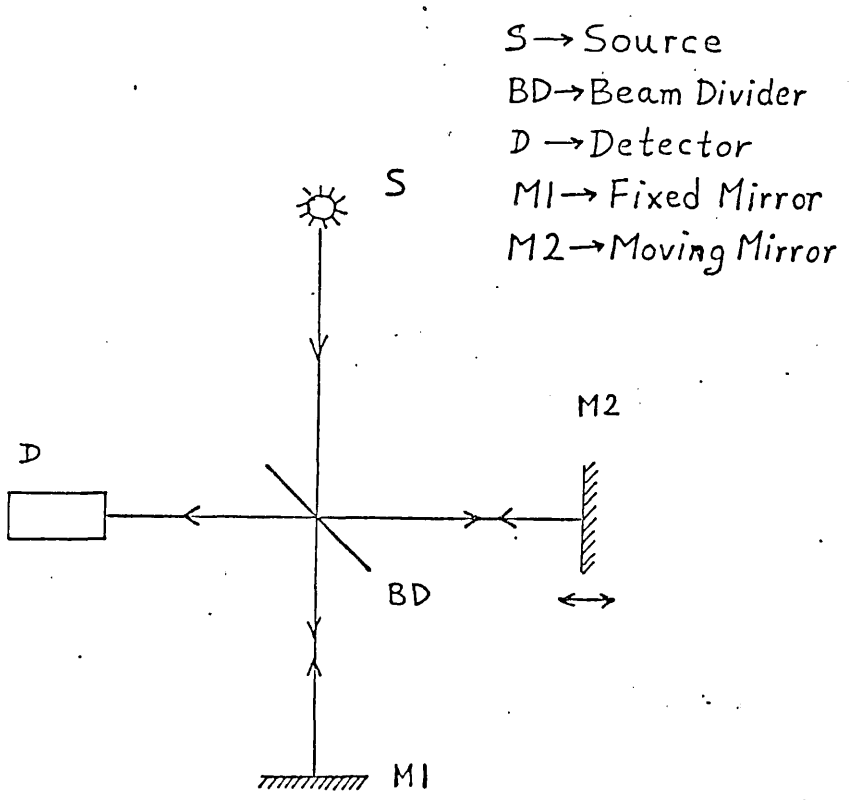

Fig. 2.1 A schematic diagram of a Michelson interferometer.

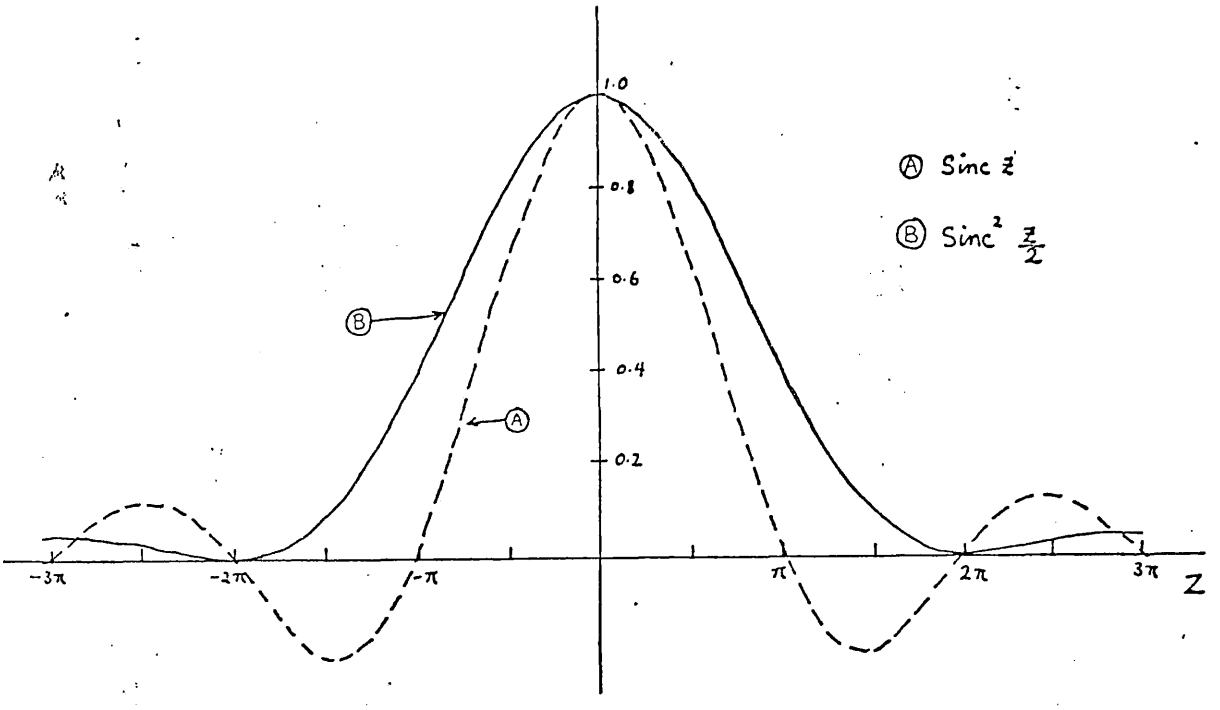

Fig. 2.2 An illustration of the result of triangular apodization.

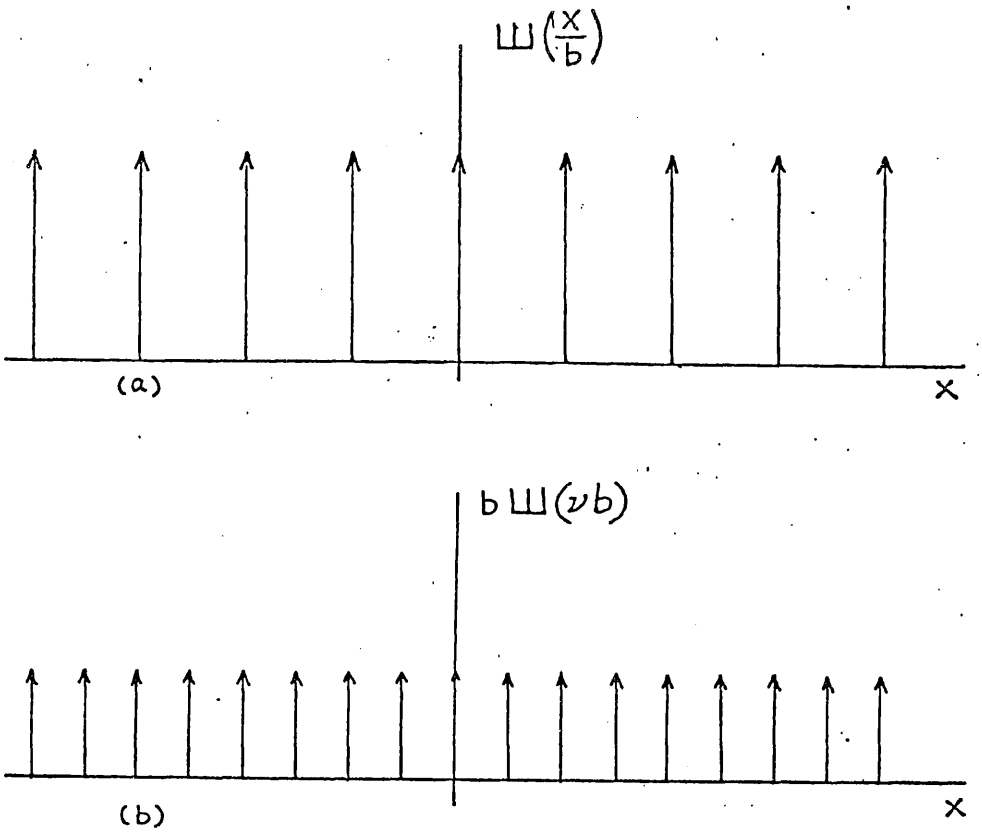

Fig. 2.3 The Shah function (a) and its Fourier transform (b).

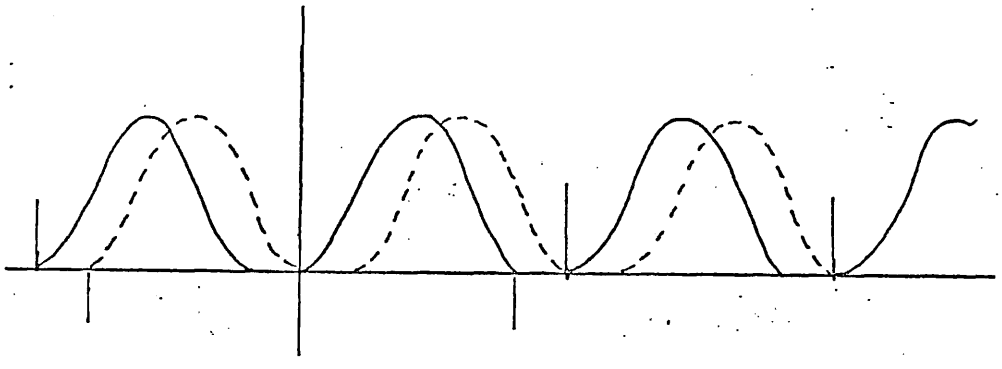

(a) The negative spectrum (dashed line) overlaps the positive spectra (solid line).

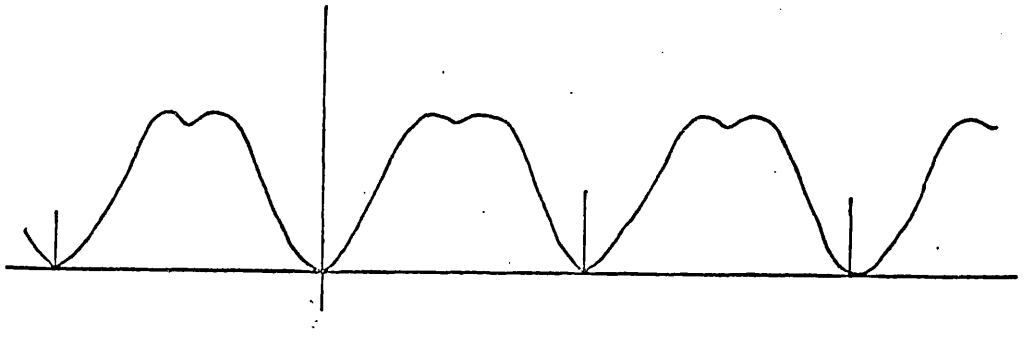

(b) The resultant spectrum is the sum of all spectral components.

Fig. 2.4 An illustration of the aliasing effect.

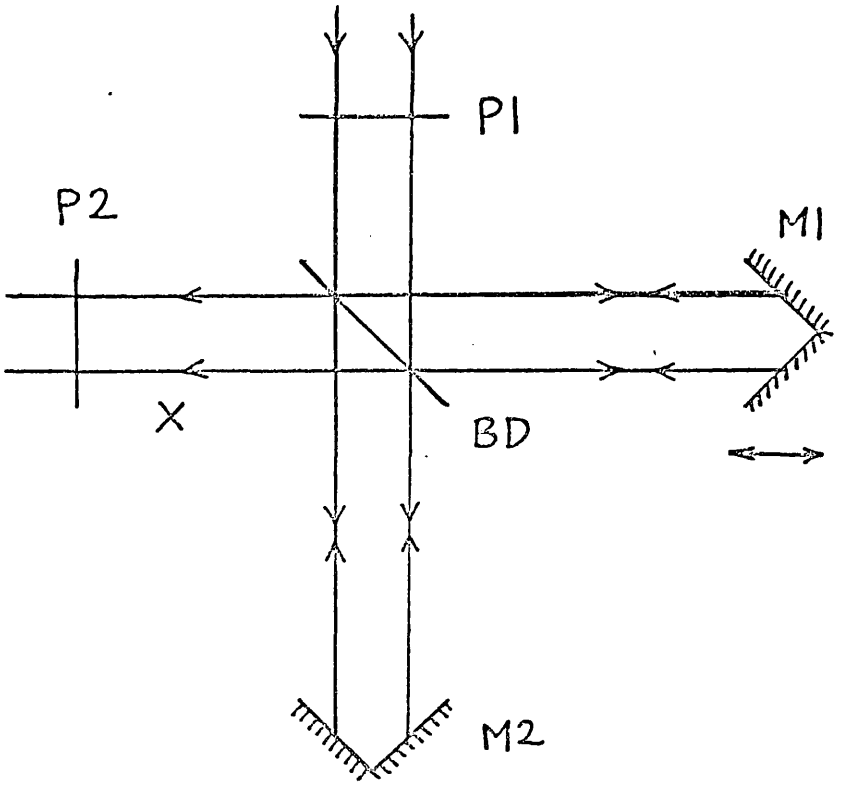

Fig. 2.5 A schematic diagram of a Martin and Puplett polarising interferometer.

CHAPTER 3

DISPERSIVE FOURIER TRANSFORM SPECTROCOPY

3.1 INTRODUCTION

With conventional Fourier transform spectroscopy, the specimen under investigation is put in the entrance or in the exit port of the interferometer. This technique will produce no phase information in the resulting spectrum of the sample [i.e. only intensity or power versus frequency]. The phase spectrum must be obtained from the power spectrum by using the Kramers-Kronig analysis, but this method of getting the phase spectrum is approximate due to the incompleteness of the experiment data.

To overcome this problem, dispersive Fourier transform spectroscopy (DFTS) has been developed to produce simultaneous amplitude and phase spectra of the sample on a single scan. The main difference between this and the conventional technique is that one beam of the interferometer is modified by either inserting the sample into the optical path, or by replacing a reference mirror with the sample. Hence, the dispersion in the refractive index of the sample will cause the interferogram to become asymmetric and shifted in optical path difference. It follows from this that both the amplitude and phase spectra of the sample may be recovered from the recorded interferograms, and this will be shown later.

The object of the DFTS measurement is to extract the optical constants of a sample from its measured complex transmission or reflection spectrum. Due to the range of samples available, there are,

essentially three basic dispersive techniques that have been used. These techniques are shown schematically in fig. 3.1 .

The configuration (a) is the simplest arrangement of the three, where the sample is just inserted into the optical path in the fixed arm of the interferometer. In this configuration the radiation passes through the sample twice, hence the name double-pass transmission measurement. If the sample is highly absorbing, then the single-pass configuration is better suited for the measurement. In this configuration the interferometer is arranged so that the radiation is offset by a certain amount from the axis, and the beam will only pass through the sample once [see (b)]. The advantage of this configuration is that the insertion loss measured is the square root of that measured in the double-pass configuration. So this gives us a factor of $\sqrt{T}$ advantage. The third configuration is for opaque samples, and it is essentially that the fixed mirror is replaced by the sample.

3.2 THE GENERAL THEORY OF DFTS

The term complex insertion loss was introduced by Chamberlain (1972) and is expressed as follows:

$$\tilde{L}(\nu) = L(\nu) \exp[i \phi(\nu)] \qquad (3.1)$$

where $\tilde{L}(\nu)$ is the complex insertion loss of the specimen, and this represents the complex factor by which the amplitude of a wave is modified when a specimen replaces vacuum or the reference mirror. The relationship between $\tilde{L}(\nu)$ and the optical constants of the sample is

different for different types of optical configuration. These relationships will be derived later in this chapter for the three optical configurations shown in fig. 3.1.

In order to understand the principles of DFTS [Birch and Parker 1979], let us consider a Michelson interferometer with a specimen of complex insertion loss $\tilde{L}(\nu)$ in one arm (fig. 3.2), say arm A, and a moving mirror in the other arm. To simplify the calculations, we will only take the electric field component of the electromagnetic wave, and this propagating electric field is expressed as a Fourier integral as

$$\tilde{\mathcal{E}} = \int_{-\infty}^{\infty} \tilde{E}_o(\nu) \exp[2\pi i\nu(z-ct)]\, d\nu \qquad (3.2)$$

where $\tilde{\mathcal{E}}$ is the Fourier integral of the electric vector $\tilde{E}_o(\nu)$. If we consider the radiation beams propagated into each arm of the interferometer , and assume the system is symmetrical, then the output from the moving mirror arm (e.g. arm B) will be

$$\tilde{\mathcal{E}}_b = \int_{-\infty}^{\infty} \tilde{E}_o(\nu) \exp[2\pi i\nu(z+x-ct)]\, d\nu \qquad (3.3)$$

where x/2 is the displacement of the moving mirror from the position of zero optical path difference. The factor of two arises because radiation travels through this displacement twice. Hence the output beam from the fixed arm is

$$\tilde{\mathcal{E}}_a = \int_{-\infty}^{\infty} \tilde{E}_o(\nu) \exp[2\pi i\nu((z-ct)]\, d\nu \qquad (3.4)$$

This expression will only be right if the system is symmetrical, so when the specimen is inserted into the optical path, the expression

will become

$$\tilde{\mathcal{E}}_a = \int_{-\infty}^{\infty} \tilde{E}_o(\nu)\ L\ (\nu)\ \exp i[2\pi\nu(z-ct)+\phi\ (\nu)]\ d\nu \qquad (3.5)$$

From the principle of linear superposition, the resultant electric field at the detector will be the sum of these two outputs, i.e.

$$\begin{aligned}\tilde{\mathcal{E}}_R &= \tilde{\mathcal{E}}_a + \tilde{\mathcal{E}}_b \\ &= \int_{-\infty}^{\infty} \tilde{E}_o(\nu) \left\{ \exp[2\pi i\nu(z+x-ct)+L\ (\nu)\ \exp\ i[2\pi i\nu(z-ct)+\phi\ (\nu)]\ d\nu \right. \\ &= \int_{-\infty}^{\infty} \tilde{g}(\nu,x)\ \exp[2\pi i\nu(z-ct)]\ d\nu \qquad (3.6)\end{aligned}$$

where

$$\tilde{g}(\nu,x) = \tilde{E}_o(\nu)\,[L(\nu)\exp i\phi(\nu)+\exp\ 2\pi i\nu x] \qquad (3.7)$$

and $x=2d$.

The intensity of a wave is defined as

$$I = \mathcal{E}_R \cdot \mathcal{E}_R^{*} \qquad (3.8)$$

where * is the complex conjugate. Therefore the resultant beam intensity is

$$\begin{aligned}\int_{-\infty}^{\infty} \tilde{g}(\nu,x)\ \tilde{g}^{*}(\nu,x)\ d &= \int_{-\infty}^{\infty} \hat{E}_o(\nu)\ \hat{E}_o^{*}(\nu)\ [1+L^2(\nu)]\ d\nu \qquad (3.9) \\ &+ 2\int_{-\infty}^{\infty} \tilde{E}_o(\nu)\ \tilde{E}_o^{*}(\nu)\ \cos[\phi(\nu)-2\pi\nu x\ ]\ d\nu\end{aligned}$$

Notice that the first term on the right of the equation is constant, and independent of x, but the second term is dependent upon x and is

called the interference function. Then the interferogram which we are recording has the intensity function

$$I_s(x) = 2\int_{-\infty}^{\infty} \tilde{E}_o(\nu)\, \tilde{E}_o^*(\nu)\, L(\nu) \cos\,(\phi(\nu) - 2\pi x\nu)\, d\nu \qquad (3.10)$$

and this function can be expressed as the sum of even and odd parts

$$\begin{aligned} I_s(x) = &\int_{-\infty}^{\infty} 2\, \tilde{E}_o(\nu)\, \tilde{E}_o^*(\nu)\, L(\nu) \cos\phi(\nu) \cos(2\pi\nu x)\, d\nu \\ &+ \int_{-\infty}^{\infty} 2\, \tilde{E}_o(\nu)\, \tilde{E}_o^*(\nu)\, L(\nu) \sin\phi(\nu) \sin(2\pi\nu x)\, d\nu \end{aligned} \qquad (3.11)$$

If we take $$\rho(\nu) = 2\, \tilde{E}_o(\nu)\, \tilde{E}_o^*(\nu)\, L(\nu) \qquad (3.12)$$

then equation (3.11) becomes

$$\begin{aligned} I_s(x) = &\int_{-\infty}^{\infty} \rho(\nu) \cos\phi(\nu) \cos(2\pi\nu x)\, d \\ &+ \int_{-\infty}^{\infty} \rho(\nu) \sin\phi(\nu) \sin(2\pi\nu x)\, d \end{aligned} \qquad (3.13)$$

Now if we are taking the Fourier transform of this function by using sine and cosine transforms, then we have

$$p(\nu) = \int_{-\infty}^{\infty} I_s(x) \cos 2\pi\nu x\, dx = \rho(\nu) \cos\phi(\nu)$$

$$q(\nu) = \int_{-\infty}^{\infty} I_s(x) \sin 2\pi\nu x\, dx = \rho(\nu) \sin\phi(\nu)$$

From Fourier analysis the complex Fourier transform of the function I(x) is given as

$$\begin{aligned} FT\,\{I(x)\} &= p(\nu) + iq(\nu) \\ &= \rho(\nu) \exp i\phi(\nu) \end{aligned} \qquad (3.15)$$

so this has a modulus of

$$\rho(\nu) = [\, p^2(\nu) + q^2(\nu) \,]^{1/2} \qquad (3.16)$$

and the phase is given as

$$\phi(\nu) = \arctan\, (q(\nu)/p(\nu)) \qquad (3.17)$$

From equation (3.12) we have the complex insertion loss related to the complex Fourier transform of the interferogram:

$$\int_{-\infty}^{\infty} I_s(x) \exp 2\pi i\nu x \, dx = 2 \tilde{E}_o(\nu) \tilde{E}_o^*(\nu) L(\nu) \exp i\phi(\nu) \qquad (3.18)$$

Now if the specimen is removed from the interferometer, the output beams from the two arms will be expressed by equations 3.3 and 3.4. Then the intensity is recorded as

$$I_o(x) = \int_{-\infty}^{\infty} \rho(\nu) \cos(\phi_o(\nu) - 2\pi\nu x) \, d\nu \qquad (3.19)$$

This is normally called the background interferogram, which is very similar to Eq. 3.10, but with

$$\rho_o(\nu) = 2 \tilde{E}_o(\nu) \tilde{E}_o^*(\nu) \qquad (3.20)$$

Then the Fourier transform of this interferogram is

$$\int_{-\infty}^{\infty} I_o(x) \exp 2\pi i\nu x \, dx = 2 \tilde{E}_o(\nu) E_o^*(\nu) \exp i\phi_o(\nu) \qquad (3.21)$$

From equations 3.18 and 3.21, the insertion loss $\tilde{L}(\nu)$ can be obtained as the ratio of the two complex Fourier transforms

$$\tilde{L}(\nu) = \int_{-\infty}^{\infty} I_s(x) \exp 2\pi i\nu x \; dx \; / \int_{-\infty}^{\infty} I_o(x) \exp 2\pi i\nu x \; dx \tag{3.22}$$

$$= \text{FT}\left\{I_s(x)\right\} \; / \; \text{FT}\left\{I_o(x)\right\}$$

Thus, we can calculate the complex insertion loss of the specimen from the recording of the specimen and background interferograms. It will be shown in the next section that the complex optical constants of the specimen can be determined by using the relationships between the insertion loss and the optical constants for each particular configuration.

3.3 COMPLEX REFRACTIVE INDEX

Maxwell's equations for an electromagnetic field in a dielectric medium can be written as follows:

$$\begin{aligned} \nabla \cdot \underset{\sim}{D} &= \rho \\ \nabla \cdot \underset{\sim}{B} &= 0 \\ \nabla \wedge \underset{\sim}{H} &= \underset{\sim}{j} + \underset{\sim}{D} \\ \nabla \wedge \underset{\sim}{E} &= -\underset{\sim}{B} \end{aligned} \tag{3.23}$$

where $\underset{\sim}{E}$ is the electric field, $\underset{\sim}{H}$ is the magnetic field, $\underset{\sim}{D}$ is the electric displacement, $\underset{\sim}{B}$ is the magnetic induction, ρ is the charge density of the medium, and $\underset{\sim}{j}$ is the current density. From Ohm's law the current density can be expressed as

$$\underset{\sim}{j} = \sigma \underset{\sim}{E} \tag{3.24}$$

where σ is the electrical conductivity of the medium.

For an isotropic medium, $\underset{\sim}{D}$ and $\underset{\sim}{E}$ are parallel, Thus

$$\underset{\sim}{D} = \varepsilon \underset{\sim}{E} \tag{3.25}$$

where ε is the permittivity of the medium. Similarly, for the magnetic properties of the medium, $\underset{\sim}{H}$ can be expressed as

$$\mu \underset{\sim}{H} = \underset{\sim}{B} \tag{3.26}$$

where μ is the permeability of the medium. Furthermore, if the medium is homogeneously electrically neutral, there will be no net charge, i.e. $\rho = 0$. Then Maxwell's equations will become

$$\nabla \cdot \underset{\sim}{D} = \varepsilon \nabla \cdot \underset{\sim}{E} = 0 \tag{3.27}$$

$$\nabla \cdot \underset{\sim}{H} = 0 \tag{3.28}$$

$$\nabla \wedge \underset{\sim}{H} = \sigma \underset{\sim}{E} + \varepsilon \dot{\underset{\sim}{E}} \tag{3.29}$$

$$\nabla \wedge \underset{\sim}{E} = -\mu \dot{\underset{\sim}{H}} \tag{3.30}$$

By taking the curl of equation 3.30 and using equation 3.29 we can obtain the differential wave equation for the electric field in this type of medium. This equation is given as

$$\nabla^2 E = \mu \varepsilon \ddot{\underset{\sim}{E}} + \mu \sigma \dot{\underset{\sim}{E}} \tag{3.31}$$

where $\dot{\underset{\sim}{E}}$ is the time derivative of $\underset{\sim}{E}$, and a similar expression holds for the magnetic field vector, but we shall consider the electric field only. We assume that the material is non-magnetic so that the magnetic field has no interaction with it.

Let us take the plane wave solution of equation 3.31 in the form of

$$\underset{\sim}{E} = \underset{\sim}{E}_o \exp i(\underset{\sim}{k}.\underset{\sim}{r} - wt) \qquad (3.32)$$

where $\underset{\sim}{k}$ is the propagation wave vector, and w is the angular frequency.

If we take a simple example of a wave travelling in the positive x direction, the electric field vector will become

$$E = E_o \exp i[kx-wt] \qquad (3.33)$$

and substituting into the wave equation 3.31 , we have

$$\frac{\partial^2 E}{\partial x^2} = \mu\varepsilon\frac{\partial^2 E}{\partial t^2} + \mu\sigma\frac{\partial E}{\partial t} \qquad (3.34)$$

so that

$$K^2 = w^2\mu\left(\varepsilon + \frac{i\sigma}{\omega}\right) \qquad (3.35)$$

If we compare this equation with the situation for non-conducting media (i.e. $\sigma = 0$), where it has the form

$$K^2 = w^2\mu\varepsilon \qquad (3.36)$$

where ε in this case is real, then the dielectric constant can be expressed as a complex number, i.e.

$$\hat{\varepsilon} = \varepsilon + i\frac{\sigma}{\omega} \tag{3.37}$$

Hence $$k = w\sqrt{\mu\hat{\varepsilon}} = \frac{\omega}{V} \tag{3.38}$$

where V is the phase velocity of the wave front in the medium, i.e. the speed of light in the medium.

The general definition of the refractive index is the ratio of the speed of light in free space to the speed when travelling through a medium, thus, the refractive index is

$$\hat{N}(w) = \frac{c}{V} = \frac{c}{\omega}K = \frac{K}{\omega\sqrt{\mu_o\varepsilon_o}}$$

$$\hat{N}(w) = \left[\frac{\mu}{\mu_o\varepsilon_o}\left(\varepsilon + \frac{i\sigma}{\omega}\right)\right]^{1/2} \tag{3.39}$$

$$= n + ik \tag{3.40}$$

where n and k are the real and imaginary parts of the refractive index, respectively. If we introduce the symbols ε_1, and μ_1 to represent the relative permeability and relative permittivity of the medium, respectively, then the equation will become

$$\hat{N}(w) = n + ik = \frac{\mu_1\mu_o}{\mu_o\varepsilon_o}\left[\varepsilon_1\varepsilon_o + \frac{i\sigma}{\omega}\right]^{1/2} \tag{3.41}$$
$$= \mu_1\left(\varepsilon_1 + \frac{i\sigma}{\omega\varepsilon_o}\right)^{1/2}$$

Since we have assumed that the medium is non-magnetic, that is to say $\mu_1 = 1$, then the refractive index is

$$\tilde{N}(w) = \left(\varepsilon_1 + \frac{i\sigma}{\omega \varepsilon_o} \right)^{1/2} \qquad (3.42)$$

and the complex refractive index can also be written as

$$\hat{\varepsilon} = (\hat{N})^2 \qquad (3.43)$$

where $\hat{\varepsilon}$ is the complex dielectric function of the medium, and is expressed as follows:

$$\hat{\varepsilon} = \varepsilon_1 + \left(\frac{i\sigma}{\omega \varepsilon_o} \right) = \varepsilon' + i\varepsilon'' \qquad (3.44)$$

where ε' and ε'' are the real and imaginary parts of the dielectric constant, respectively.

Another useful parameter is the absorption coefficient of the medium. If we subsitute equation (3.39) and equation (3.40) into the equation for the plane wave, then we have

$$\underset{\sim}{E} = \underset{\sim}{E}_o \exp\left(- \frac{K\omega}{c} \tilde{\underset{\sim}{k}} . \underset{\sim}{r}\right) \exp iw\left[\frac{n}{c} \hat{\underset{\sim}{k}} . \underset{\sim}{r} - wt \right] \qquad (3.45)$$

where $\hat{\underset{\sim}{k}}$ is a unit vector in the direction of propagation.

This expression represents a plane wave with a velocity c/n which has an amplitude damped exponentially by the term

$$\exp\left(- \frac{k\omega}{c} \hat{\underset{\sim}{k}} . \underset{\sim}{r}\right) \qquad (3.46)$$

The intensity I is proportional to the product of $\underset{\sim}{E}$ and $\underset{\sim}{E}^*$. Thus

$$I \propto \underset{\sim}{E} \cdot \underset{\sim}{E}^*$$

and $I_o = E_o^2$

$$I = I_o \exp - \alpha (\hat{\underset{\sim}{k}} . \underset{\sim}{r}) \tag{3.47}$$

which is usually called Lambert's Law. Since

$$\frac{I}{I_o} = \frac{\underset{\sim}{E} \cdot \underset{\sim}{E}^*}{E_o^2} = \exp(- \frac{2k\omega}{c} \hat{\underset{\sim}{k}} . \underset{\sim}{r}) \tag{3.48}$$

$$\text{then} \quad \alpha = \frac{2k\omega}{c} = 4\pi\nu k \tag{3.49}$$

is called the power absorption coefficient per unit length of the medium.

A summary of the relationships between the complex refractive index and the complex dielectric constant is given below :

$$\varepsilon' = n^2 - k^2$$

$$\varepsilon'' = 2nk$$

$$n^2 = \frac{1}{2}\left\{ [(\varepsilon')^2 + (\varepsilon'')^2]^{1/2} + \varepsilon' \right\}$$

$$k^2 = \frac{1}{2}\left\{ [(\varepsilon')^2 + (\varepsilon'')^2]^{1/2} - \varepsilon' \right\}$$

and (3.50)

$$\alpha = 4\pi\nu k$$

3.4 FRESNEL'S EQUATIONS

Fresnel's equations [Born and Wolf 1970] express the relationships between the amplitude attenuation and phase shift of an electromagnetic wave passing through an interface between two different media and the optical constants of the two media. In general the equations assume that the complex optical constants for the two media are $\hat{n}_1$ and $\hat{n}_2$, respectively,

$$\begin{aligned}
\hat{r}_{\perp} &= (\hat{n}_1 \cos\hat{\theta}_1 - \hat{n}_2 \cos\hat{\theta}_2)/(\hat{n}_1 \cos\hat{\theta}_1 + \hat{n}_2 \cos\hat{\theta}_2) \\
\hat{r}_{\parallel} &= (\hat{n}_1 \cos\hat{\theta}_2 - \hat{n}_2 \cos\hat{\theta}_1)/(\hat{n}_1 \cos\hat{\theta}_2 + \hat{n}_2 \cos\hat{\theta}_1) \\
\hat{t}_{\perp} &= 2\,\hat{n}_1 \cos\hat{\theta}_1 \,/\, (\hat{n}_1 \cos\hat{\theta}_1 + \hat{n}_2 \cos\hat{\theta}_2) \\
\hat{t}_{\parallel} &= 2\,\hat{n}_1 \cos\hat{\theta}_1 \,/\, (\hat{n}_1 \cos\hat{\theta}_2 + \hat{n}_2 \cos\hat{\theta}_1)
\end{aligned} \qquad (3.51)$$

Notice that the equations given above are complex, and $\hat{r}$ is the amplitude reflection coefficient and $\hat{t}$ is the amplitude transmission coefficient of the incident wave. Each reflection and transmission has been separated into two components where $\perp$ represents perpendicular to and $\parallel$ represents parallel to the plane of incidence, where $\hat{\theta}_1$ and $\hat{\theta}_2$ are the complex angles of incidence for media 1 and 2 respectively. In most of our experiments the incident beam is arranged to be normal to the plane of the interface of the media, so that $\hat{\theta}_1$ and $\hat{\theta}_2$ equal zero. Thus we have

$$\begin{aligned}
\hat{r}_{\perp} &= \hat{r}_{\parallel} = \hat{r}_{12} = (\hat{n}_1 - \hat{n}_2)/(\hat{n}_1 + \hat{n}_2) \\
\hat{t}_{\perp} &= \hat{t}_{\parallel} = \hat{t}_{12} = 2\,\hat{n}_1/(\hat{n}_1 + \hat{n}_2)
\end{aligned} \qquad (3.52)$$

The subscript order indicates that incidence is from medium 1 into medium 2. Thus if we reverse the beam, i.e. the ray travels from medium 2 to medium 1, then we have

$$\hat{r}_{21} = (\hat{n}_2 - \hat{n}_1)/(\hat{n}_1 + \hat{n}_2) = -\hat{r}_{12}$$

$$\hat{t}_{21} = 2\hat{n}_2 / (\hat{n}_1 + \hat{n}_2) = \frac{\hat{n}}{\hat{n}_1}\hat{t}_{12} \qquad (3.53)$$

For transmission measurements, the samples are usually made as lamellar crystals, and this introduces the phenomenon of multiple reflections from the two interface planes. In order to obtain the relationship between $\hat{L}(\nu)$ and the optical constants of the specimen, one has to understand this problem of multiple reflections.

Now, suppose that a plane parallel specimen of refractive index $\hat{n}_2$ is placed in a medium of refractive index $\hat{n}_1$. In our measurements the medium is vacuum, i.e. $\hat{n}_1 = 1$. If a ray of light is incident onto this specimen, it will suffer multiple internal reflections at the two interfaces, as shown in fig. 3.3.

The total transmission of the ray is given by the infinite sums of all these partial waves. Therefore the complex amplitude transmission coefficient $\hat{T}$ is given by

$$\hat{T} = \hat{t}_{12}\hat{a}_2\hat{t}_{21} + \hat{t}_{12}\hat{a}_2^3\hat{r}_{21}^2\hat{t}_{21} + \hat{t}_{12}\hat{a}_2^5\hat{r}_2^4\hat{t}_{21} + \ldots\ldots \qquad (3.54)$$

and $\hat{R}$ is

$$\hat{R} = \hat{r}_{12} + \hat{t}_{12}\hat{a}_2^2\hat{r}_{21}\hat{t}_{21} + \hat{t}_{12}\hat{a}_2^4\hat{r}_{21}^3\hat{t}_{21} + \ldots \qquad (3.55)$$

where $\hat{a}_2$ is the complex attenuation of the specimen, and is given by

$$\hat{a}_2 = \exp(-\frac{\alpha}{2} x)\exp(i2\pi n \nu x) \qquad (3.56)$$

with $\alpha = 4\pi\nu k$ as the power absorption coefficient, and x is the distance travelled. The expressions for $\hat{T}$ and $\hat{R}$ can be simplified as shown by Bell [1972]

$$\hat{T} = \hat{a}_2(1-\hat{r}_{12}^2)/(1-\hat{a}_2^2\hat{r}_{12}^2)$$

$$\hat{R} = \hat{r}_{12}(1-\hat{a}_2^2)/(1-\hat{a}_2^2\hat{r}_{12}^2) \qquad (3.57)$$

3.5 RELATIONSHIPS BETWEEN OPTICAL CONSTANTS AND INSERTION LOSS FOR DFTS

(a) Reflection measurements

If the specimen under observation has a very large absorption coefficient in the measured spectral range, a transmission experiment is impossible, so one has to use a reflection measurement. In this type of measurement a thick specimen is chosen, with the front surface polished optically flat.

A background interferogram, $I_o(x)$ is first recorded with the reference mirror, then this mirror is removed and replaced with the specimen in the same plane as the reference mirror.

Let us take the amplitude reflectivity of the mirror as

$$\hat{r}_m(\nu) = \exp i\pi \qquad (3.58)$$

Since the specimen is of a strongly absorbing material, only the first term of the reflection is considered. Thus the reflectivity for the specimen is given as

$$\hat{r}(\nu) = r(\nu)\exp i\phi_r(\nu) \qquad (3.59)$$

The phase delay of the specimen is in the range of $\pi \leq \phi_r(\nu) \leq 2\pi$. The grand maxima of the two interferograms $I_s(x)$ and $I_o(x)$ are recorded at nearly the same position of the moving mirror. Therefore, both interferograms can be recorded from the same starting point. This point will be used as the reference point for the phase spectrum and so no further information is then required. Thus the insertion loss is given by :

$$\tilde{L}(\nu) = r(\nu)\ \exp i[\phi_r(\nu) - \pi] \qquad (3.60)$$

and from equation 3.52 , the complex refractive index can be calculated from the inversion of the Fresnel equation. This equation is given below:

$$\tilde{n}(\nu) = [\ 1 - \hat{r}(\nu)\ ]/[\ 1 + \hat{r}(\nu)\ ] \qquad (3.61)$$

b) Measurement of a thick transparent specimen using a single pass arrangement

The calculation of the insertion loss for this configuration will be simplified by recording the interferogram I (x) with wings of equal

optical path length x, symmetric about the position of zero optical path difference (see fig. 3.4). The value of x is normally chosen to be sufficiently large to resolve all features in the specimen spectrum.

In the standard procedure, the sampling point nearest to the zero crossing at the centre of the interferogram is used to balance and apodize the interferogram. In dispersive measurements, this point is also used as the reference point for calculating the phase spectrum of the specimen. The specimen is now inserted into the fixed arm of the interferometer and let us assume that the specimen has a mean refractive index of $\bar{n}$ (assuming that the dispersion in n is small). If the specimen is thick enough, the signatures associated with the higher order transmitted waves will be well separated on the recording. Thus, the first main signature will be displaced by $(\bar{n}-1)d$, from the centre point of the back-ground interferogram. The higher order ones will be at $(3\bar{n}-1)d$, $(5\bar{n}-1)d$, etc, where d is the thickness of the sample.

In practice, the optical constants can be determined from the first order interferogram. The experimental procedure for this is to record the sample interferogram by shifting the starting point of the recording by an amount 2B, and scanning the interferogram over an optical path difference of 2x. The value for the shift of starting point is chosen by this equation:

$$2B \simeq (\bar{n}-1)d$$

The reason for this is to allow the zero crossing point for the specimen interferogram to nearly coincide with the background zero crossing point, and the same levelling and apodization are used as for the background interferogram.

Due to the thickness of the sample, only the first order transmitted partial wave will be recorded and the relevant complex transmission coefficient of the specimen will be only the first term of the equation (3.54).

$$t(\nu) = t(\nu)\exp[\, i\phi(\nu)] = \frac{4\hat{n}(\nu)}{[1+\hat{n}(\nu)]^2}\exp[\, 2\, i\pi\nu\hat{n}(\nu)\, d] \tag{3.62}$$

The insertion loss can be determined from the complex ratio

$$\tilde{L}'(\nu) = L'(\nu)\exp i\phi_L'(\nu) = FT[I_s(x)]/\, FT[I_o(x)] \tag{3.63}$$

of the complex transforms of the interferograms. Notice that this is not the true complex insertion loss because of the shift in the starting points. So the complex insertion loss will include the term $4\pi\nu B$ in the phase spectrum, i.e.

$$\hat{L}(\nu) = L'(\nu)\exp(\, i\phi_L'(\nu) + 4\pi\nu B) \tag{3.64}$$

so that we have the insertion loss in terms of the experimentally determined quantities. Thus the optical constants can be calculated by using the relationship between complex transmission and insertion loss. Thus

$$\hat{L}(\nu) = T(\nu)\exp(-i2\pi\nu d) = \frac{4\hat{n}(\nu)}{[1+\hat{n}(\nu)]^2}\exp(i\, 2\pi\nu[\,\hat{n}(\nu) - 1\,]d) \tag{3.65}$$

The factor $(\hat{n}(\nu)-1)d$ follows from the fact that the optical path

length is increased by replacing the vacuum with the specimen in the interferometer.

If $k(\nu) << n(\nu)$, which is normally the case if one can perform the experiment, then the equation can be simplified as

$$n(\nu) = 1 + \frac{1}{2\pi\nu d}\left[\phi_L(L) + 4\pi\nu B \pm 2m\pi\right]$$

$$k(\nu) = \frac{1}{2\pi\nu d}\ln\left[\frac{4n(\nu)}{[1+n(\nu)]^2}\frac{1}{L(\nu)}\right] \qquad (3.66)$$

so that $n(\nu)$ and $k(\nu)$ can be calculated in separated equations. Notice that the term $\pm 2m\pi$ is introduced to ensure continuity in the true value of the phase difference because the computed value is plotted in the range of $\pm\pi$.

c) Single-pass measurement on a thin absorbing specimen

If the specimen is of an absorbing nature, the measurement will be done by using the reflection type of arrangement. However, if it is possible for a transmission measurement to be performed on a carefully thinned specimen, then the single-pass transmission measurement is better than an amplitude reflection measurement because the phase change $\phi_r(\nu)$ of the reflection will be close to π, the value for the reference mirror. In case of the single-pass measurement, the phase change

$$\phi_L(\nu) \simeq 2\pi\nu[\,n(\nu) - 1\,]\,d \qquad (3.67)$$

is normally much larger and more easily measured. Since the specimen

is very thin, the signatures associated with all the partial waves described by equation 3.54 will overlap on the interferogram. Thus, the full geometric series will apply. From equations 3.57 and 3.52, the complex insertion loss will be expressed as

$$\hat{L}(\nu) = \frac{4\hat{n}(\nu)}{(1+\hat{n}(\nu))^2} \frac{\exp 2\pi i \nu (\hat{n}(\nu)-1)\, d}{1-[(1-\hat{n}(\nu))/(1+\hat{n}(\nu))]^2 \exp 4\pi i \nu \hat{n}(\nu) d} \qquad (3.68)$$

where $\hat{n}(\nu)$ is the complex refractive index, and this complex insertion loss can be related to $\hat{T}(\nu)$ by equations 3.63 and 3.64. Since the measurements are done close to the reststrahlen band, where the dispersion in the refractive index is large, there are many branches in the phase spectrum, and this makes it difficult to trace the phase to zero frequency. Hence, some other information like an amplitude reflection measurement is needed to ensure the phase continuity at low frequencies.

Since the equation for $\hat{L}(\nu)$ cannot be solved analytically for the complex refractive index, it must be solved numerically at each frequency using a method such as a complex secant method, an iterative procedure described by Conte and de Boor [1972]. This method needs an initial estimate of n at some point on the spectrum, and starting values for n at the first spectral point above and below the reststrahlen band can be obtained from equation 3.68, or from supplementary amplitude reflection measurements. The final values for n at these points are used as the starting values at the adjacent spectral points, and the process continues until $n(\nu)$ and $k(\nu)$ have been determined within the experimental uncertainty throughout the spectrum.

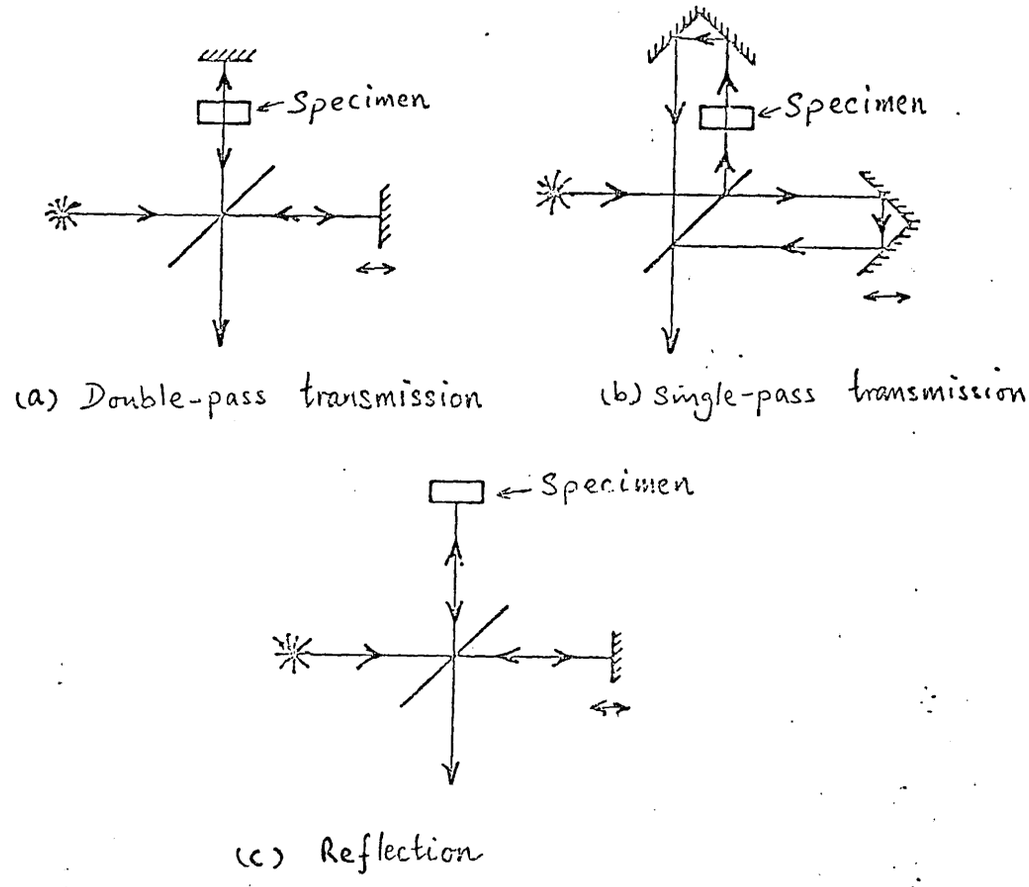

Fig. 3.1 Schematic diagram of the three basic interferometers used in DFTS.

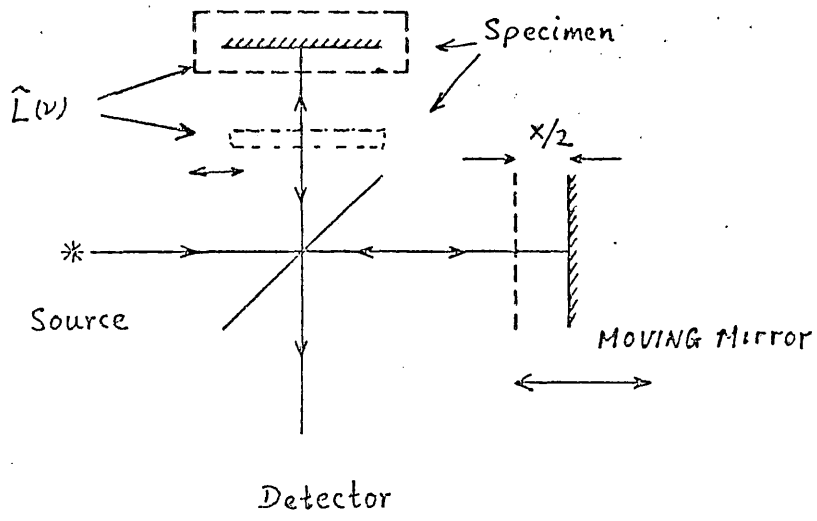

Fig. 3.2 An illustration of the term insertion loss when the fixed mirror is replaced with the specimen, or the specimen is inserted into the optical path.

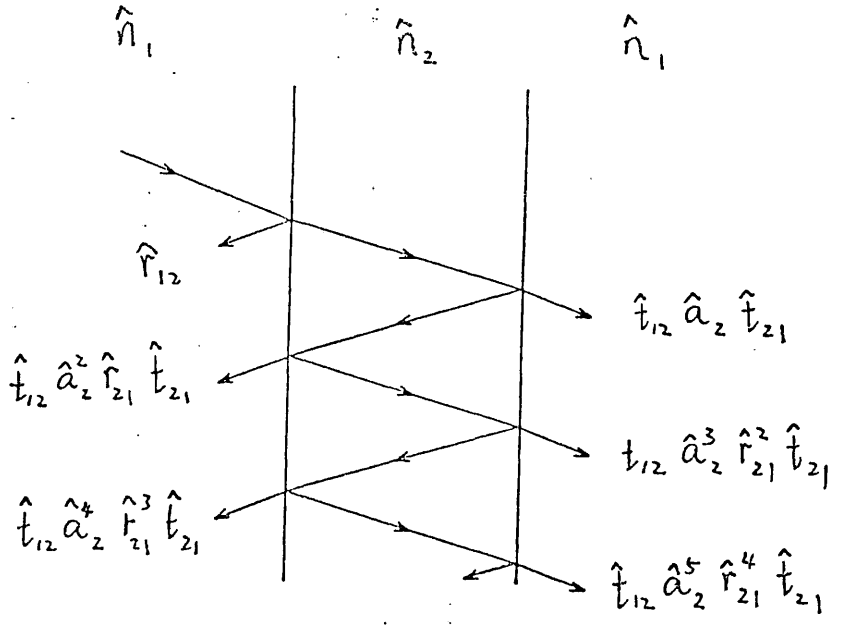

Fig. 3.3 An illustration of multiple reflections by a lamellar crystal.

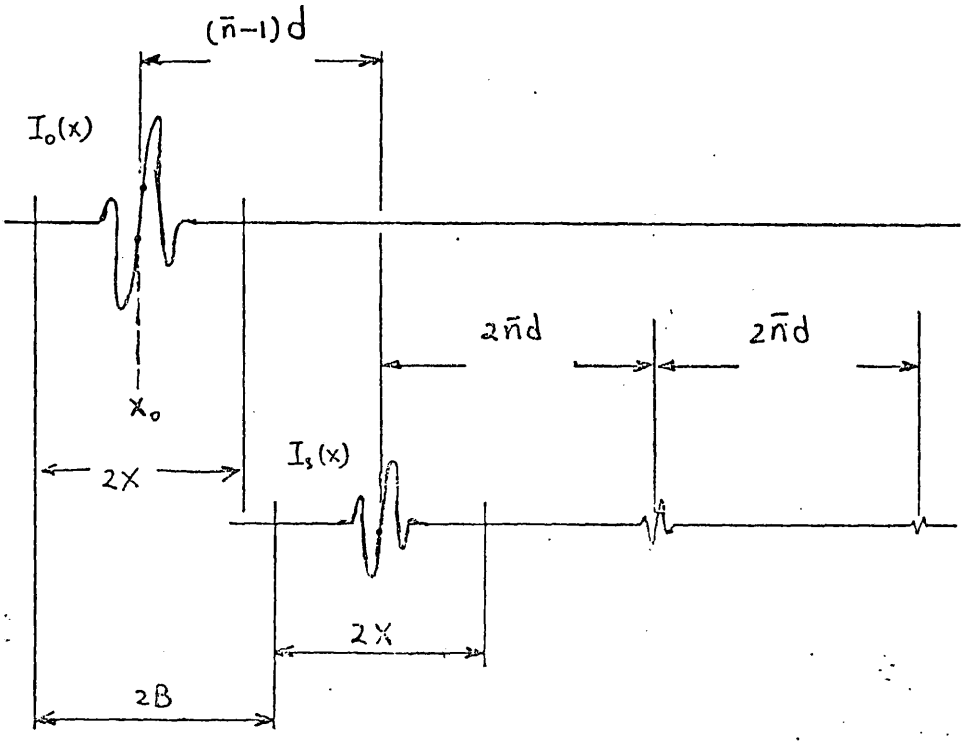

Fig. 3.4 A schematic diagram to show the relative starting points of the sample ($I_o(X)$) and background ($I_s(X)$) interferograms.

CHAPTER 4

LEAST-SQUARES METHOD

The least-squares method was first proposed by Davies [1973]. The idea behind this is that the electromagnetic field expansions are broken up into many regions around the radiation scatterer (in this case the wire grid). The advantage of this procedure is that many sets of functions which satisfy Maxwell's equations are known and some properties may only be desirable in one region and not in the next. Thus each region can be described independently and the problem is therefore reduced to that of satisfying the boundary conditions over the interfaces of the regions.

If we take the region u, the electric and magnetic fields can be expanded in series of the form:

$$\underset{\sim}{E}^{u} = \sum_{n=0}^{N} c_n^u \, f_n^u$$

$$\underset{\sim}{H}^{u} = \sum_{n=0}^{N} c_n^u \, g_n^u \qquad (4.1)$$

where each pair of vector fields f ,g must satisfy Maxwell's equations over the entire u region. In practice, the expansions are finite and will not satisfy the continuity conditions on the interface between the neighbouring regions exactly. Thus there will be some mismatch in the electric and magnetic fields across the interface. So some method has to be used to choose the coefficient c for each region to reduce this mismatch to zero within some approximation.

The method used by Davies is to take the expression for the average mismatch over the boundaries, and defined as

$$\sum_{u,v} \int_{S_u \cap S_v} \left(\left| \underset{\sim}{E}^{u}_{tan} - \underset{\sim}{E}^{v}_{tan} \right|^2 + Z^2 \left| \underset{\sim}{H}^{u}_{tan} - \underset{\sim}{H}^{v}_{tan} \right|^2 \right) W(\underset{\sim}{r}) \, ds \qquad (4.2)$$

where $S_u \wedge S_v$ is the intersection of the boundaries of regions u and v, and the subscript "tan" indicates the component parallel to the interface. $W(\underline{r})$ is the weighting function which allows different boundaries to be weighted differently. Normally the value is equal to unity. The value Z is the positive impedance which gives the relative magnitude of the magnetic contribution to this mismatch. Because the field expansions in each region are solutions of Maxwell's equations, the normal component of the electric and magnetic fields will satisfy the boundary conditions if the tangential components are matched [Jones 1964]. Unfortunately, the method gives only an approximate matching of tangential components, and it seems that the normal component may not satisfy the boundary conditions to the same degree of approximation. Therefore, a mismatch for the normal component is added. The definition for such a mismatch is given below:

$$\sum_{u,v} \int_{S_u \wedge S_v} \left(\left| \varepsilon^u \underline{E}_\perp^u - \varepsilon^v \underline{E}_\perp^v \right|^2 + Z \left| \mu^u \underline{H}_\perp^u - \mu^v \underline{H}_\perp^v \right|^2 \right) W(\underline{r})\, ds \qquad (4.3)$$

where ε^u and ε^v are the relative electric permittivities of the medium in the regions u and v, respectively. Similarly μ^u and μ^v are the relative magnetic permeabilities. The subscript $\perp$ indicates the component normal to the interface.

In order to understand the problem of wire gratings, we take a wire grid which is assumed to be made of material of linear homogeneous permeability μ equal to the free space value of μ_o. The electric permittivity ε is equal to $N^2 \varepsilon_o$, where N is the refractive index of the material and ε_o is the permittivity of free space. All the wires in the wire grid have a radius of a, and spacing of d, and we assume that they have an infinite length (see fig. 4.1).

Let a monochromatic plane wave of angular frequency w be incident onto this plane wire grating of infinite extent. Assume the wave-vector $\underline{k}$ for this wave has the form $(k_x, k_y, 0)$. So now the problem becomes a two dimensional scattering problem, and can be expressed by two separate scalar expressions of electric field $\underline{E}$ and magnetic field $\underline{H}$ parallel to the axis of the invariance. This is only true if they are not coupled by the boundary conditions, as is true in this case.

Take the case of "E-polarisation" , i.e. $\underline{E}$ parallel to the axis of the wires, then we can write the electric field as:

$$\underline{E} = E\,\hat{\underline{z}} \tag{4.4}$$

where $\hat{\underline{z}}$ is the unit vector along the z-axis and the scalar E is the value which satisfies the two-dimensional Helmholtz equation. By taking the Maxwell curl equation (equ 3.30) and assuming the wave has a harmonic time variation of exp(iwt), then we have

$$\begin{aligned} \frac{\partial \underline{H}}{\partial t} &= \nabla \wedge \underline{E} \\ i\mu_0\omega \underline{H} &= \nabla \wedge E\,\hat{\underline{z}} \\ i\mu_0\omega \underline{H} &= \hat{\underline{z}} \wedge \nabla E \end{aligned} \tag{4.5}$$

Similarly for the case of "H-polarisation" we can write the magnetic field as

$$\underline{H} = H\,\hat{\underline{z}} \tag{4.6}$$

Again if we take the Maxwell curl, we then have

$$\begin{aligned} \varepsilon \frac{\partial \underline{E}}{\partial t} &= \nabla \wedge \underline{H} \\ i\varepsilon\omega \underline{E} &= \nabla \wedge H\,\hat{\underline{z}} \\ i\varepsilon\omega \underline{E} &= \hat{\underline{z}} \wedge \nabla \underline{E} \end{aligned} \tag{4.7}$$

Since the grating is of a periodic structure, we can therefore divide it into unit cells which extend over all values of y, and from -d/2 to d/2 in the x-direction. So the expansions for this region do not depend on the z-axis, and are periodic in the x-direction, i.e.

$$\underset{\sim}{E}(x+d,y) = \exp(-ik_x d)\ \underset{\sim}{E}(x,y)$$

$$\underset{\sim}{H}(x+d,y) = \exp(-ik_x d)\ \underset{\sim}{H}(x,y) \qquad (4.8)$$

The unit cell is further divided into four regions by the circular boundary of the wire and the lines $y=\pm Y$ (see fig.4.2).

Before we can express the electric and magnetic fields in these four regions, we first have a close look at the solutions of the Helmholtz equation in the two coordinate systems:

(a) in Cartesian coordinates (x,y,z) the Helmholtz equation is

$$\nabla^2\psi + k^2\psi = 0 \quad , \qquad (4.9)$$

then the general solution is in the form of

$$\psi = \exp(\pm i\alpha x)\ \exp(\pm i\beta y)\ \exp\pm(\kappa^2+\beta^2)^{\frac{1}{2}} z \qquad (4.10)$$

(b) in cylindrical coordinates the Helmholtz equation is in the form

$$\frac{1}{r}\frac{\partial}{\partial r}\left(r\frac{\partial\psi}{\partial r}\right) + \frac{1}{r^2}\frac{\partial^2\psi}{\partial r^2} + \frac{\partial^2\psi}{\partial z^2} + k^2\psi = 0 \qquad (4.11)$$

then the general solution is

$$\psi = [\ J_m(\sqrt{k^2-\gamma^2}\ r) + Y_m(\sqrt{k^2-\gamma^2}\ r)]\exp\pm(irz)\ \exp\pm(im\phi) \qquad (4.12)$$

where J_m , Y_m are Bessel functions of order m of the first and second kind respectively.

For the case of H-polarisation, and for $y > Y$, i.e. the field after the wave has passed through the wire grid, from equ(4.7) we have

$$iw\varepsilon E_x = \frac{\partial}{\partial y} H$$
$$iw\varepsilon E_y = \frac{\partial}{\partial x} H \qquad (4.13)$$

and H is the solution of the Helmholtz equation [equ(4.10)], and is in the form of

$$Z_o H = \sum_{\ell=-L}^{L} b_\ell \exp(-i\alpha_\ell x - i\chi_\ell |y|) \qquad (4.14)$$

where $\alpha_\ell = k_x + \frac{2\pi\ell}{d}$

$\chi_\ell = k^2 - \alpha_\ell^2$

$Z_o = \left(\frac{\mu_o}{\varepsilon_o}\right)^{1/2}$

From equ(4.13) we have the electric field expansions as

$$iw\varepsilon E_x = \frac{1}{Z_o} \frac{\partial}{\partial y} \sum_{-L}^{L} [\, b_\ell \exp(-i\alpha_\ell x - i\chi_\ell |y|)$$
$$E_x = \sum_{-L}^{L} - \frac{\chi_\ell}{k} b_\ell \exp(-i\alpha_\ell x - i\chi_\ell |y|) \qquad (4.15)$$

where $k^2 = k_x^2 + k_y^2 = \frac{\omega^2}{c^2}$

Similarly

$$E_y = \sum_{\ell=-L}^{L} \frac{\alpha_\ell}{k} b_\ell \exp(-i\alpha_\ell x - i\chi_\ell |y|) \qquad (4.16)$$

Assuming that the incident wave originated at $y=-\infty$, then the field in the region of $y<-Y$ will be expressed as

$$Z_o H = \exp(-k_x x - ik_y y) + \sum_{\ell=-L}^{L} a_\ell \exp(-i\alpha_\ell x - i\chi_\ell |y|) \qquad (4.17)$$

and using the same procedure as before we will obtain the electric field in x and y components as

$$E_x = -\frac{k_y}{K}\exp(-ik_x X - ik_y y) + \frac{\chi_\ell}{K}\exp(-i\alpha_\ell x - i\chi_\ell |y|)$$

$$E_y = \frac{k_x}{K}\exp(-ik_x X - ik_y y) + \frac{\alpha_\ell}{K}\exp(-i\kappa_\ell x - i\chi_\ell |y|) \qquad (4.18)$$

where the extra term $\exp(-ik_x x - ik_y y)$ represents the incident wave, with wave vector of $(k_x, k_y, 0)$.

In the region of $|y|<Y$, the fields are expanded in the solution of the Helmholtz equation appropriate to the geometry of the cylinder, i.e. in terms of the cylindrical coordinate system. From the solution of this Helmholtz equation [equ(4.12)], the electric and magnetic fields inside the boundary of the wire can be written as:

$$Z_o H = \sum_{m=-M}^{M} A_m J_m(Nkr)\exp(im\phi) \qquad (4.19)$$

and where

$$E = \frac{1}{w\varepsilon r}\frac{\partial H}{\partial \phi} = \sum_{-M}^{M}\frac{m}{N^2 kr} A_m J_m(Nkr)\exp(im\phi) \qquad (4.20)$$

and

$$E_\phi = \frac{1}{\omega\varepsilon r}\frac{\partial H}{\partial r} \qquad (4.21)$$

$$= \sum_{-M}^{M} -\frac{1}{iN} A_m J_m'(Nkr) \exp(im\phi)$$

where J_m is the Bessel function of order m of the first kind, and as usual the prime on J_m' indicates the derivative of that function. Notice that the function Y_m in equ(4.12) does not enter the expression, because of being singular at the centre of the wire, but it will be included in the field expression for outside the wire.

By using a process similar to that used above, we can obtain the electric and magnetic fields outside the cylinder as

$$Z_o H = \sum_{-M}^{M} [B_m J_m(kr) + C_m Y_m(kr)] \exp(im\phi) \qquad (4.22)$$

and

$$\begin{aligned} E_r &= \sum_{-M}^{M} \frac{m}{kr} [B_m J_m(kr) + C_m Y_m(kr)] \exp(im\phi) \\ E_\phi &= \sum_{-M}^{M} \frac{-1}{i} [B_m J_m'(kr) + C_m Y_m'(kr)] \exp(im\phi) \end{aligned} \qquad (4.23)$$

The expressions given above will allow the boundary conditions at the surface of the cylinder to be satisfied exactly. Thus, for the continuity of the tangential components, we have

$$Z_o H^{outside} = Z_o H^{inside} \qquad (4.25)$$

and

$$E_\phi^{outside} = E_\phi^{inside} \qquad (4.26)$$

From equ(4.19) and equ(4.22), we obtain

$$A_m J_m(Nka) = B_m J_m(ka) + C_m Y_m(ka) \qquad (4.27)$$

and from equ(4.21) and equ(4.24), we have

$$A_m J_m'(Nka) = B_m J_m'(ka) + C_m Y_m'(ka) \qquad (4.28)$$

By using the Wronskian relation for the Bessel function [Abramowitz 1965] the coefficients B_m and C_m can be expressed in terms of A_m, i.e.

$$B_m = \frac{\pi ka}{2} \left[J_m(Nka)\, Y_m'(ka) - \frac{1}{N} J_m'(Nka)\, Y_m(ka) \right] A_m$$
$$C_m = \frac{\pi ka}{2} \left[\frac{1}{N} J'(Nka)\, J_m(ka) - J_m(Nka)\, J_m'(ka) \right] A_m \qquad (4.29)$$

If we consider that the wires are made of perfectly conducting material, then the electric field inside the wire will become zero, so at the boundary conditions of

$$E_\phi^{outside} = 0 \qquad \text{at} \qquad r = a \qquad (4.30)$$

then the equ(4.24) becomes zero at r=a, and so we have

$$B_m J_m'(ka) + C_m Y_m'(ka) = 0 \quad , \qquad (4.31)$$

so

$$C_m = - \frac{J_m'(ka)}{Y_m'(ka)} B_m \qquad (4.32)$$

Thus, for a perfect conductor the expressions for the coefficients are very much simpler.

For the case of "E-polarisation" the electric field is expanded in series identical to those of $Z_o H$, and so similarly we will have the expressions

$$B_m = \frac{\pi kq}{2} \left[J_m(Nka)\, Y_m'(ka) - N\, J_m'(Nka)\, Y_m(ka) \right] A_m \qquad (4.33)$$

$$C_m = \frac{\pi ka}{2} \left[N J_m'(Nka) J_m(ka) - J_m(Nka) Y_m'(ka) \right] \Lambda_m$$

for the coefficients.

For perfectly conducting wire, the electric field again is equal to zero at r=a. Thus the expression similar to $Z_o H$ will become zero at r=a, then we have

$$B_m J_m(ka) + C_m Y_m(ka) = 0$$

$$C_m = - \frac{J_m(ka)}{Y_m(ka)} B_m \tag{4.34}$$

From the above expressions, there is only one unknown in the region near the wire, i.e. Λ_m (or B_m in the case of perfectly conducting wire). Due to the periodicity of the grating, the near field expressions can be simply extended beyond the unit cell in a continous condition, i.e.

$$\underset{\sim}{H}\ (d/2,y) = \exp(-ik_x d)\ \underset{\sim}{H}\ (-d/2,y)$$

$$\underset{\sim}{E}\ (d/2,y) = \exp(-ik_x d)\ \underset{\sim}{E}\ (-d/2,y) \tag{4.35}$$

Now the electric and magnetic fields in all the regions have been expressed in series. Thus, we only have to match the boundary conditions as follows

1) to match the nearfield and plane wave expressions on y=Y in the unit cell.
2) to match the near field and plane wave expressions on y=-Y,
3) to match the near field at the neighbouring unit cell along x=d/2.

The full mismatch expression becomes

$$\int_{-\frac{d}{2},Y}^{\frac{d}{2},Y} \left(\left| \underset{\sim}{E}^{near} - \underset{\sim}{E}^{plane} \right|^2 + Z^2 \left| \underset{\sim}{H}^{near} - \underset{\sim}{H}^{plane} \right|^2 \right) W(x,y)\, dx$$

$$+ \int_{-\frac{d}{2},-Y}^{\frac{d}{2},-Y} \left(\left| \underset{\sim}{E}^{near} - \underset{\sim}{E}^{plane} \right|^2 + Z^2 \left| \underset{\sim}{H}^{near} - \underset{\sim}{H}^{plane} \right|^2 \right) W(x,-Y)\, dx \qquad (4.36)$$

$$+ \int_{-Y}^{Y} \left(\left| \underset{\sim}{E}^{near}(d/2) - \exp(-ik\,d)\, E^{near}(d/2) \right|^2 \right.$$

$$\left. + Z^2 \left| \underset{\sim}{H}^{near}(d/2) - \exp(-ik\,d)\, H^{near}(d/2) \right|^2 \right) W(d/2,y)\, dy$$

The impedance Z will be set to Z_o, the impedance for free space, and the weighting function is set to unity for all integrals.

In general the integrals above are evaluated numerically [Beunen 1976]. Then the coefficients a_ℓ , b_ℓ , and A_m can be obtained from the solutions of these integrals. Thus, the power reflection and transmission coefficients can be calculated by using the formulae

$$R = \sum |a_\ell|^2 \frac{\chi_\ell}{k_y}$$

$$T = \sum |b_\ell|^2 \frac{\chi_\ell}{k_y} \qquad (4.37)$$

where R and T are the reflection and transmission coefficients, respectively.

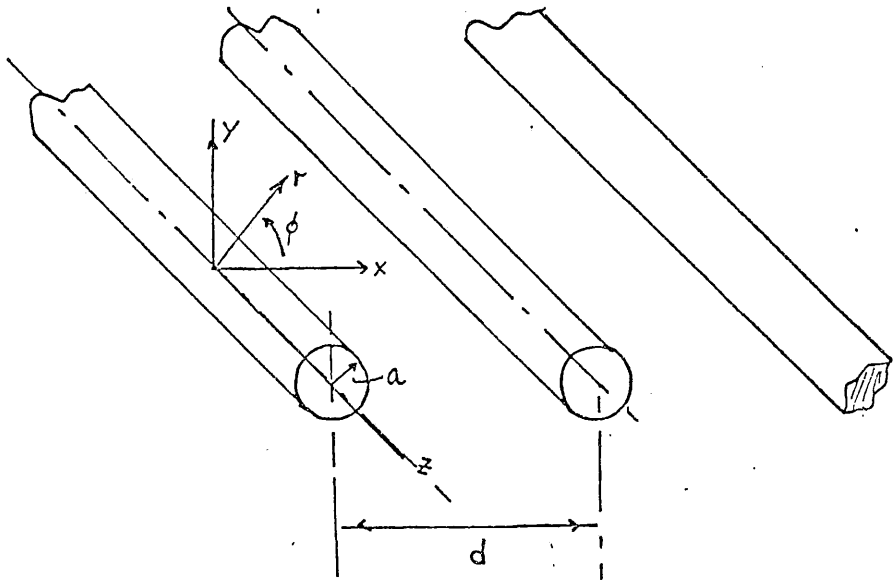

Fig. 4.1 Schematic diagram of a wire grid with infinite length.

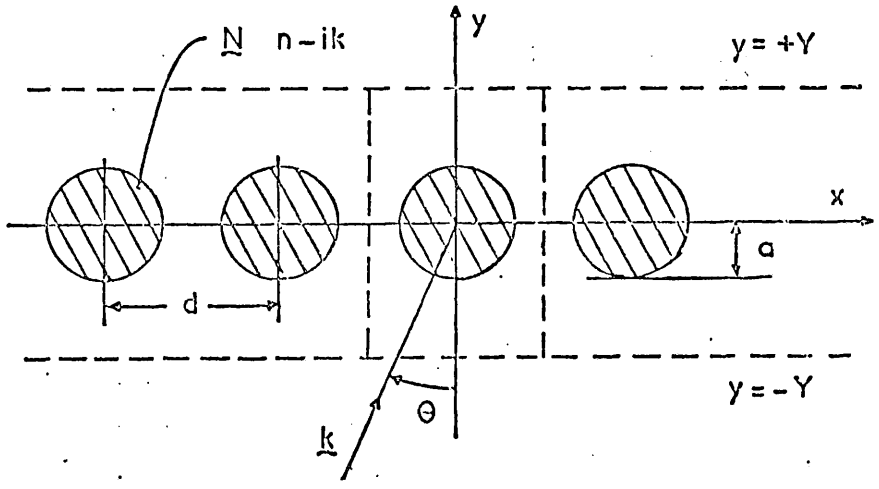

Fig. 4.2 A diagram showing a section normal to the wire grid.

CHAPTER 5

THE INTERFEROMETERS

5.1 THE BASIC DESIGN OF THE INTERFEROMETERS

The design of the transmission and reflection instruments is based upon the modular unit developed by the National Physical Laboratory and produced by Grubb Parsons & Co. Ltd. [Chantry 1971], and both instruments are of the Michelson type of interferometer. A large number of additional compatible units which are not commercially available have been designed and made here at Westfield to enable the use of the interferometer to be extended to more specialised work.

The configuration of the transmission instrument is illustrated in fig.5.1 [Parker et al 1978]. The heart of the instrument is the central cube, which is a commercial unit, with the beam divider held vertically along its diagonal. The four vertical side faces of the cube are used to bolt on extension arms. These arms are used to house the radiation source, the fixed mirror, moving mirror, sample holder, lens, and detector etc.

A commercial quartz encapsulated mercury lamp is used as the radiation source, which emits a broad band of submillimetre wave radiation by thermal emission. The lamp is placed in a water cooled housing because of its high working temperature. This lamp is also enclosed in a copper cylinder, with a hole of diameter 8mm centred on the optical axis of the instrument to limit the aperture.

A collimator (B) is employed to direct the radiation emitted from the lamp to be incident upon the beam divider in the centre cube. The purpose of the beam divider is to direct two partial beams into the

two mirror arms by transmission and reflection. The special arrangement of these two mirror arms ensures that the return beams are off axis by employing two sets of roof-top mirrors instead of conventional plane mirrors. This novel design is to enable the radiation beam to pass through the sample once only, and also, by changing a few components, it enables the instrument to be used as a polarising interferometer, as described later in this chapter.

The movable roof-top mirror in one arm is mounted on the non-rotating spindle of a precision made micrometer which has a maximum travel of 25 mm and is driven by an electrically powered stepping motor. The control electronics of this motor allows the mirror to move in either direction in step lengths of 2.5, 5, 7.5, and 10μm. From Chapter 2 it follows that these step lengths give corresponding aliasing frequencies of 1000, 500, 333, and 250 cm^{-1} respectively. The roof-top mirror in the fixed arm is clamped, but a facility is provided for aligning it by a system of three aligning screws, and an adjusting screw is also provided to rotate the mirror about the optical axis. In addition to these, a facility is provided in the movable mirror arm to slide the mirror up and down perpendicular to the optical axis.

Following reflection by these two mirrors, the beams are incident back onto the beam divider with an off set of 25.4 mm. The radiation beam from the fixed arm passes through the sample if the sample is inserted into the optical path. The sample holder is mounted under a liquid nitrogen cooled cylinder. After transmission and reflection by the beam divider the two beams recombine and interfere according to the difference in the optical paths in the two mirror arms, and the dispersion of the sample. The recombined beam then passes through an

optical focusing system which consists of either a lens or condensing mirrors. This enables the radiation beam to be focused onto the window of a Golay detector or a liquid helium cooled bolometer.

The design of the reflection instrument [Parker et al 1978b] is similar to that of the transmission instrument,but with a liquid helium cooled cryostat in the fixed arm to bring the specimen to the operating temperature of about 7k. The configuration of the interferometer is illustrated in fig 5.2. A large part of the instrument , such as the lamp housing, collimator, central cube etc, is the same as the components used in the transmission instrument described earlier.

The radiation from the lamp, S passes through the collimator, C, and then through a 1mm thick black polythylene filter, B. The purpose of the filter is to reduce the amount of unwanted radiation reaching the cryostat, thus increasing the holding time of the cryostat. The reflected beam from the mylar beam divider is propagated through a 1.5mm thick white polythylene window, W1, acting as a vacuum window, and to a mirror, M1, inclined at 45° to the beam from which it is reflected vertically upwards onto the specimen, mounted under the base of the cryostat. The mirror M1 is made by aluminising the front surface of the mylar beam divider of a second central cube unit. The beam initially transmitted by the beam divider passes through a compensating window, W2 ,identical to W1, onto a mirror, M2, acting as the vibrating mirror for the phase modulation system. The beam is then diverted through 90° onto the moving mirror, M, from which it is reflected back to the beam divider. The partial beams from the two arms are then recombined at the beam divider and focused by a polyethylene lens doublet, L, onto a Golay detector, D. The window W1

is used to separate the low and high vacuum systems. The cube unit on one side of the window, W1, together with the cryostat, can be evacuated to a pressure of 10^{-6} torr to permit the specimen to be cooled to liquid helium temperature. However, the remainder of the instrument on the other side of the window need only be evacuated to a pressure of 10^{-2} torr to eliminate atmospheric absorption.

The design of the liquid helium cryostat is illustrated in fig 5.3. The thermally insulating nylon bolts, N, are used to fix the base plates, B1 and B2, of the liquid nitrogen and liquid helium cans, respectively, in position. The base plates are held rigidly in position in a metal reference plate, R, and the specimen, X, is mounted close to, and in good thermal contact with the liquid helium can base, B2. Flexible stainless steel bellows, B, are welded into the filler tubes of the liquid nitrogen and liquid helium cans to accommodate the thermal contraction. As the specimen cools down, its front reflecting surface moves vertically as the nylon bolt contracts, but the motion is mainly in the vertical direction, hence, the misalignment is very small. The specimen then remains fixed in position as long as there is liquid in the two cans. The continuous expansion in the length of the liquid helium and liquid nitrogen cans which occurs as the liquids boil off is accommodated by the bellows, and does not affect the position of the specimen.

The sample mount is bolted to the base plate, B2, of the liquid helium can as a complete unit. The unit is designed with a rotating screen operated by two electrically powered solenoids [Parker and Lowndes 1979]. The surface of the specimen crystal is aluminised in the pattern shown in fig. 5.4, and aligned with the screen, which has a similar cut-out pattern. The purpose of the screen is to expose

either the unmetallised crystal surface or the aluminised part of the surface to the incident radiation, and it is programmed to be operated in either

1) Conventional mode; the complete interferograms are recorded first from the aluminised surface and then from the exposed crystal surface in separate scans of the moving mirror.
2) Switching mode; two interferograms are alternately sampled at each step on a single scan of the moving mirror.

The operation in the switching mode is to reduce the error of x between the location of the position of zero path difference of the reference and the crystal surfaces, i.e. a reduction of the phase error in the results.

5.2 PERFORMANCE OF THE INTERFEROMETERS

There are a number of factors which will affect the performance of the interferometers described above.

1) Detectors

The standard detector used for these two interferometers is a Golay cell. The advantages of such detectors are their convenient size, ease of operation, and room temperature operation. The performance of this type of detector is perfectly adequate for most IR applications. By choosing the window materials wisely one can study different regions of the IR spectrum with adequate signal to noise

ratio. Two most commonly used in IR work are diamond and quartz window Golay cells. The diamond Golay can respond up to and beyond the frequency of 10,000 cm^{-1}, and the cheaper quartz Golay has a high frequency cut-off at about 250 cm^{-1}.

Due to the form of the black-body radiation curve, the radiation emitted below about 30 cm^{-1} is extremely weak. At this point the Golay cell may not be good enough in some applications. To overcome this problem one usually uses a liquid helium cooled detector. The performance of the detector is described in terms of Noise Equivalent Power (NEP). The NEP for a typical liquid helium cooled detector is of the order of 1000 times better than that of a Golay in similar experimental conditions.

The helium cooled detector used with the above instruments is an antimony (Sb) doped germanium (Ge) thermal bolometer manufactured by QMC Industrial Research Limited. This detector has a working range of 2-250 cm^{-1} if a sapphire window is fitted, and is only used for the low frequency range where the performance of a Golay is inadequate, because of the big disadvantage of the need for cryogenic facilities.

2) Modulation Systems

Another source of noise in the interferometer is lamp fluctuations. To reduce this the radiation is modulated before reaching the detector, and the recording electronics only measures the signal which lies within a small bandwidth around the modulating frequency. This effect will be described in detail later.

The need of such modulation systems is due to the large amount of far IR radiation emitted by the warm walls of the interferometer and

other materials in the field of view of the detector. Due to the large acceptance angle of the Golay detector (60°), the modulation must be made far back along the optical system in order to reduce the influence of the extraneous sources.

The most simple type of modulation method is amplitude modulation (AM). In the Grubb Parsons system this is done by installing a cylindrical chopper around the lamp. However, this type of modulation system produces a large DC background load at the detector. The drift and noise of the DC level of the interferogram is often disadvantageous when accurate results are required. Another disadvantage of this AM system is that 50% of the lamp energy, or more, is lost. The main advantage is that it is frequency independent, and does not impose any response envelope on the throughput of the instrument as does the phase modulation system described next.

The next form of modulation system is that of phase modulation. In this system , the path difference is modulated by a small periodic displacement of one of the interferometer mirrors. To enable one to understand the operation of such system , let us take the modulation function as

$$F(ft) = A \sin (2\pi ft) \qquad (5.1)$$

where A is the amplitude of vibration of the mirror. The time-dependent signal from the detector is a modified form of equation 2.7.

$$S(x,t) \simeq P(\nu) \cos[\, 2\pi\nu(x + A \sin(2\pi ft))\,] \qquad (5.2)$$

The time dependent parts in this function are very complicated and the coefficients of their Fourier components are Bessel functions. But the pass band of the electronics may be arranged so as to include only the

first order, so that the resulting interferogram has the form

$$I(x) \simeq \int_0^\infty P(\nu)\ J_1(2\pi\nu A)\ \sin(2\pi\nu x)\ d \qquad (5.3)$$

Thus the throughput spectrum of the interferometer has a Bessel function envelope imposed on it. The function $J_1(2\pi\nu A)$ has its zeros at $\nu = 0$ and at a frequency given by $2\pi\nu A = 3.84$. From this envelope, one can see that the main disadvantage of PM is the fall-off on the low frequency side of the throughput spectrum.

The modulation reaches 100% in the region of the maximum of the Bessel function, which is a large improvement over the AM system of about 50%. The large DC level of the AM system is no longer modulated in the PM mode, hence the drift problems are eliminated and the noise due to the lamp source fluctuation is also reduced. The Bessel function maximises and minimises at frequencies dependent on the amplitude of the vibrating mirror. Therefore, one can adjust the amplitude of this vibration by altering the power output of the oscillator unit to maximize the response in a specific spectral region. So in effect this acts like a non-absorbing filter for the throughput spectrum.

The third modulating system is polarisation modulation for the polarising interferometer. During the measurement, the transmission instrument described earlier has been modified by replacing the mylar beam divider with a free standing wire grid, and a polariser and an analyser have also been placed in the inlet and outlet ports of the interferometer. So the arrangement of this instrument becomes the Martin Puplett type [Martin & Puplett 1970]. If instead of having a fixed polarizer, we mounted the polarizer on a rotating cylinder (fig. 5.5), then, when the radiation passes through this rotating polarizer,

its electric vector will be rotated with the polarizer. The output of the modulation system is very similar to that of AM, with symmetrical interferograms, but with the large DC level removed. So this system has the advantage of PM, but without the Bessel function envelope. i.e. the throughput of this system has a nearly flat response up to the cut off frequency of the polarizer where its polarising effect is lost. The only disadvantage is that it can only work in a polarising interferometer, so it is only used in the low frequency region.

3) Beam Dividers

The conventional beam dividers are made of mylar and are stretched on a metal frame, which is placed in the central cube of the interferometer. Since this thin mylar film is paralled sided, and the phenomenon of multiple internal reflection occurs, we have to include all these beams produced by the internal reflection in the analysis. By taking the refractive index of mylar to be 1.85, and assuming it to be a non-absorbing material, Bell[1972] has shown that for a beam of unpolarised radiation incident upon a mylar thin film, the primary transmitted beam is about 83% of the incident flux, the secondary transmitted beam is only 0.7%, and so is negligible. But the primary reflected beam is 8.9%, and 7.4% for the secondary reflection, and the third order reflection is only 0.07%. From these data, one can see that only the two primary beams and the secondary reflecting beam are significant.

Notice that the magnitudes of the two reflected partial beams are nearly equal, therefore interference exists between them, and this occurs upon each reflection by the beam divider. The phase shifts for

the internal and external reflection by the beam divider are zero and respectively. If we take D as the thickness of the mylar film and n as the refractive index, then from Bell[1972] the interference conditions for these two reflected components are given by

$$m\lambda = 2d\,(n^2 - 1/2)^{1/2} \qquad (5.4)$$

When m=1, 2, 3 .... the interference is destructive, but for m=1/2, 3/2, 5/2 .... the interference is constructive. The first minimum is at $\nu = 1/\lambda = 0$, which is very obvious because then one beam has a phase of π respect to the other. The next minima are when m=1, 2 etc. Thus the efficiency of the beam divider depends upon the interference between the two reflected beams. A set of first order interference fringes for the beam divider, with different thicknesses of mylar film is shown in fig. 5.6. So, when measurements are made by using an interferometer with a mylar beam divider, the thickness D must be chosen so as to optimise the throughput energy in the spectral region under observation. But no matter what thickness of beam divider is used, the efficiency in the spectral region near zero frequency is always low. Thus, although by using a thicker beam divider the low frequency region may be improved, the bandwidth of the first order interference fringe is narrowed, so such dividers are far from ideal for measurements below 20 cm^{-1}.

To overcome the problem of the poor low frequency response of the dielectric beam divider, the beam divider can be replaced with a free standing wire grid, with the interferometer working in the polarising mode.

4) The Recording Electronics

The recording electronics used for both instruments was basically the same. The modulated radiation falls upon the detector and the signal passes on to be rectified by a phase sensitive detector (PSD). A PSD is a system which produces a DC output signal in response to an AC input signal whose frequency is equal to that of a reference signal. The DC output given by a PSD is proportional to the amplitude of the input signal and the cosine of its phase angle relative to that of the reference signal.

A PSD acts essentially as a multiplier giving an output signal which is proportional to the product of the input signal and the reference signal. Consider a sinusoidal signal, $e_s = E_s \sin(\omega_s t + \phi)$ multiplied by a square wave reference signal; the square wave is assumed to be symmetrical about zero, and to have unit amplitude and unit mark-space ratio.

The Fourier series for a unit amplitude square wave is

$$V_r = \frac{4}{\pi}(\sin w_r t + \sin 3w_r t + \sin 5w_r t + \ldots\ldots) \qquad (5.5)$$

and the product of the reference signal and the input signal is

$$e_s V_r = \frac{4}{\pi} E_s [\sin(w_s t+\phi) \sin w_r t + \sin(w_s t +\phi) \sin w_r t + \ldots)$$

$$= \frac{2}{\pi} E_s [\cos((w_s - w_r)t+\phi) - \cos((w_s + w_r)t+\phi) \qquad (5.7)$$

$$+ \frac{1}{3}\cos((w_s - w_r)t+\phi) - \frac{1}{3}\cos((w_s + w_r)t+\phi) + \ldots]$$

Examination of the above equation shows that the product gives rise to d.c. terms for signal frequencies of w ; 3w ;5 w etc.

When $w_s = w_r$ the d.c. term is $\frac{2}{\pi} E_s \cos\phi$

When $w_s = 3w_r$ the d.c. term is $\frac{2}{\pi} E_s \frac{1}{3} \cos\phi$ etc.

In a PSD the multiplication process is followed by low pass filtering which can be performed by a simple RC filter which will attenuate all a.c. components of the product. The frequency cut-off of such a system is thus set at 1/T where T= RC, the time constant of the filter.

The noise rejection properties in a phase sensitive detection system arise in large part from the extremely narrow bandwidth which is so readily obtained by selection of filter time constant. A PSD acts somewhat like a rectifier that is tuned to the reference frequency, but its noise rejection properties are far superior to those of a conventional filter combination. Noise passed by a conventional filter circuit gives rise to a d.c. component in the normal rectification process, but in a PSD unwanted signals, like random noise, produce fluctuations about the d.c. level produced by the wanted signal at the reference frequency. It would be quite impractical to obtain the narrow bandwidth of a PSD system with a conventional filter circuit.

Since the output signal from the PSD is in analogue form, a data acquisition system must be used to record the sampled data points so that the data processing can be performed by a digital computer. The recording electronics used in the past few years is a very primitive system. The output medium which is used in the system is a paper tape, and the block diagram of the system is shown in fig. 5.7. The output of the PSD is connected to a paper chart recorder and a digital voltmeter. The purpose of the chart recorder is to monitor the signal of the interferogram during the operation, and the DVM is used to

convert the analogue signal from the PSD into digital form. Thereafter, this digital data is punched onto the paper tape by the tape punch. All these operations are controlled by the sampling pulse generator, which produces triggering pulses in the following order:

1) the moving mirror is stepped,
2) after a short time delay, the signal from the PSD is latched into the DVM,
3) once the DVM has converted the analogue signal into digital form the data is then punched onto the paper tape, and after another short time delay the whole procedure is repeated until the end of the scan.

The above system did give an adequate facility for recording data over the past few years because there were no online computing facilities in the laboratory, and the data punched on the paper tape had to be submitted to the University Computing Centre. However, with the increasing use of microprocessors in electronic equipment, it is now feasible to use one of these micros to handle the data acquisition and data processing for the Fourier spectrometers, and such a system has been built by the author and used with Fourier spectrometers at Westfield College. This system is described in the next chapter.

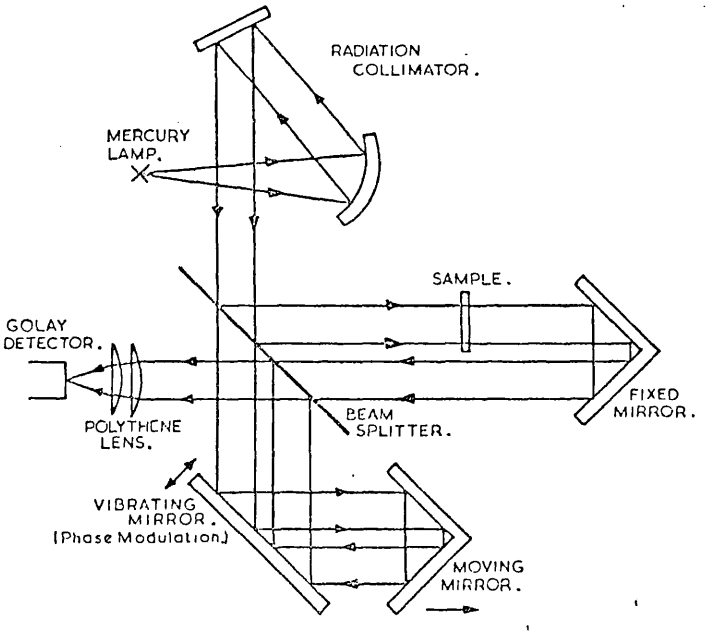

(a) THE INTERFEROMETER

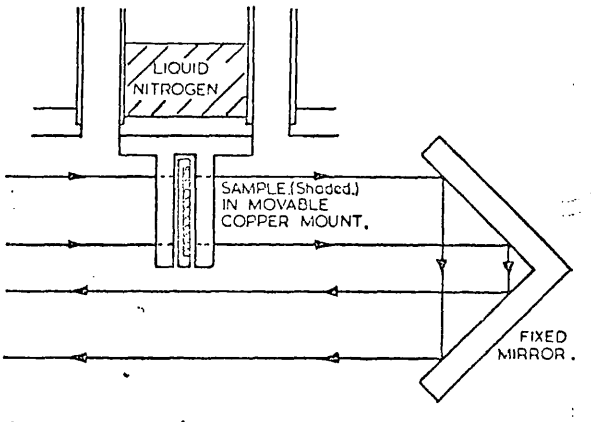

(b) SAMPLE HOLDER

Fig. 5.1 Schematic diagram of the single-pass transmission instrument.

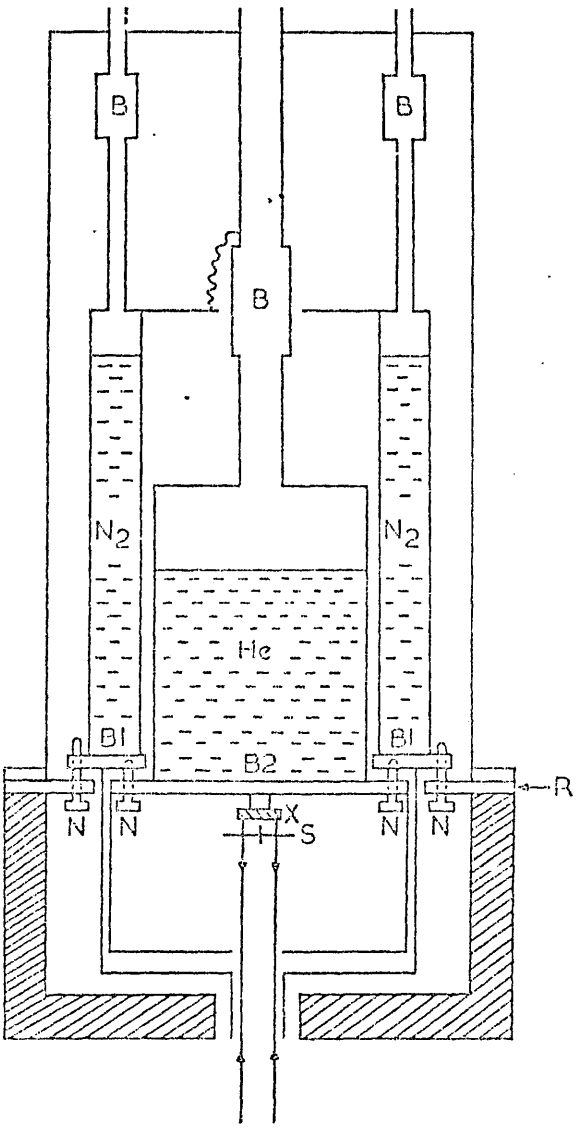

Fig 5.3 Schematic diagram of the liquid helium cryostat.

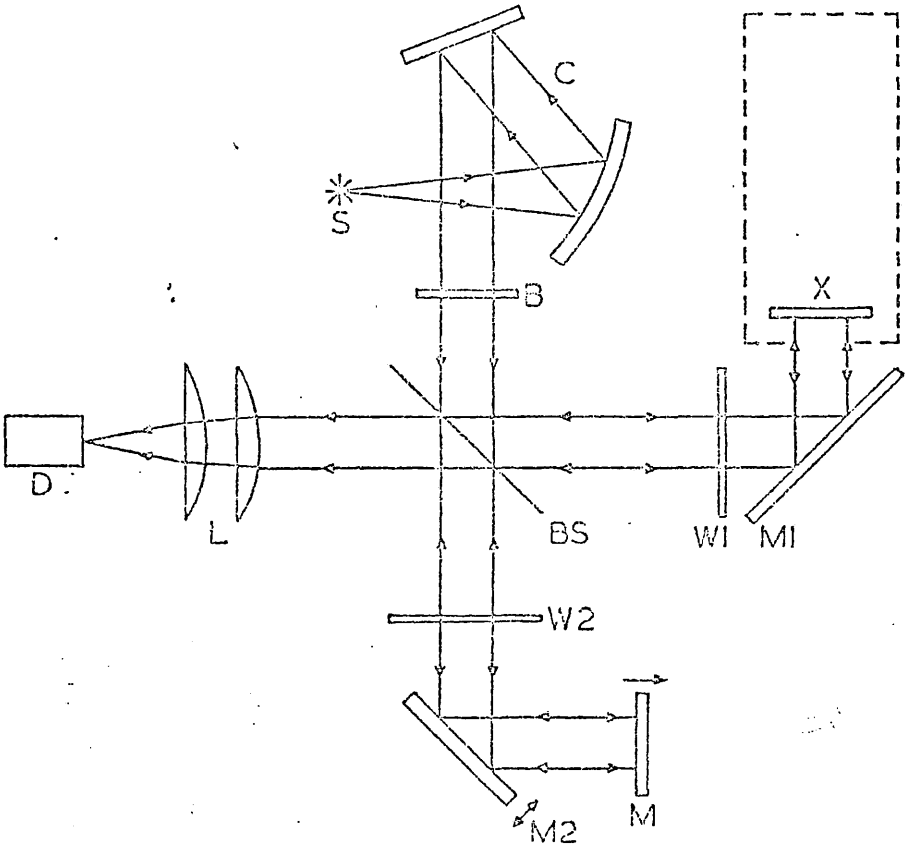

Fig. 5.2 Schematic diagram of the reflection instrument.

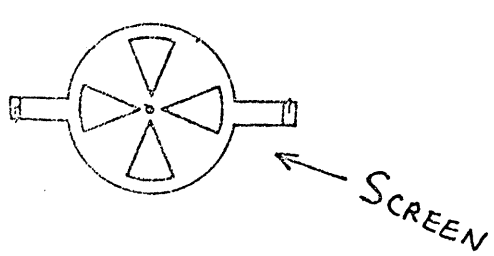

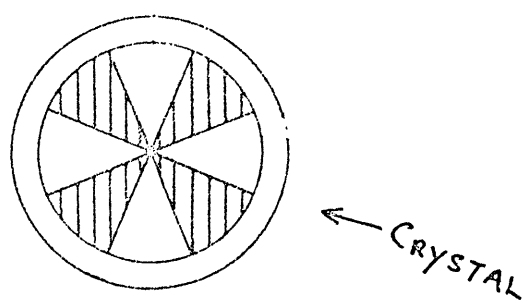

Fig. 5.4 Schematic diagram of the switching screen pattern.

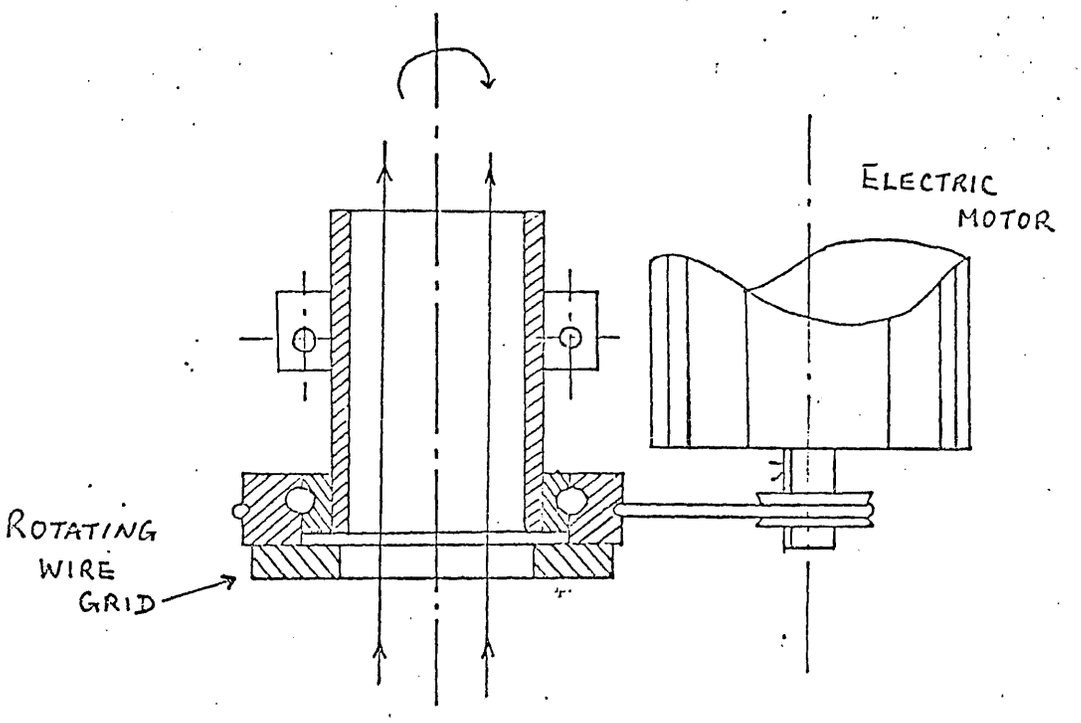

Fig. 5.5 Schematic diagram of the polarising modulator.

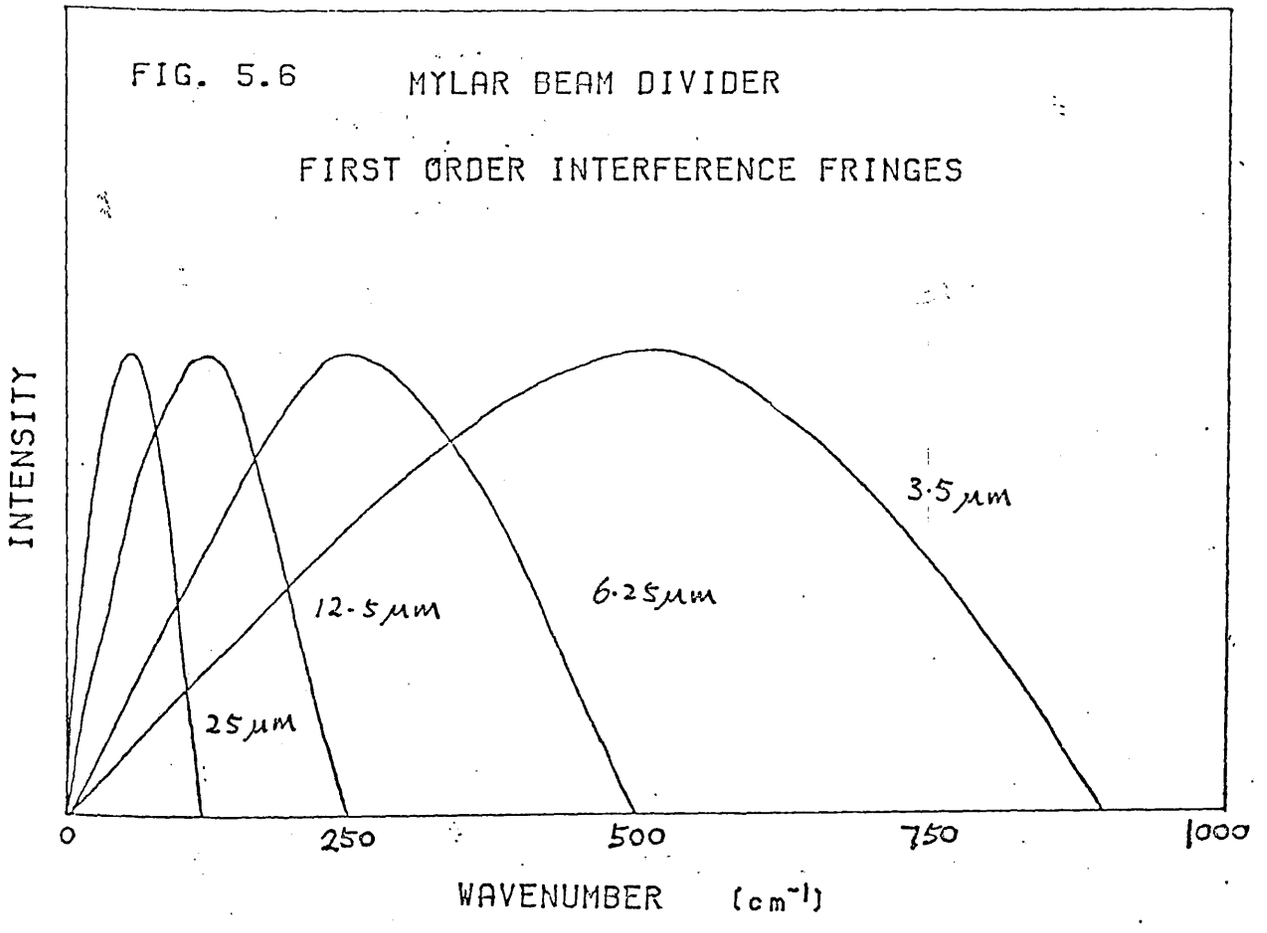

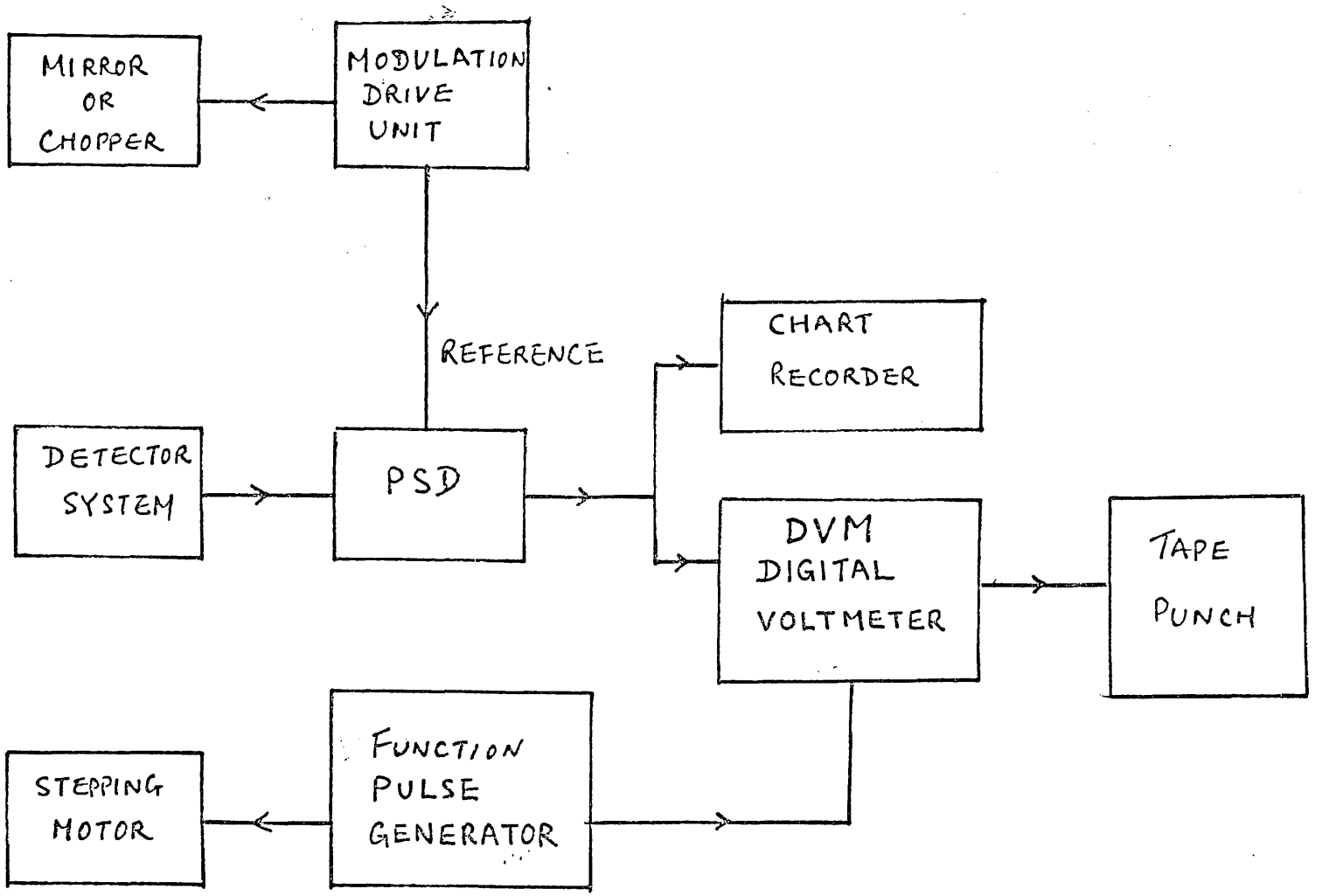

Fig. 5.7 Block diagram of the recording electronics.

CHAPTER 6

A MICROCOMPUTING SYSTEM FOR THE FOURIER SPECTROMETERS

6.1 INTRODUCTION

In the few short years that microprocessors have been available, they have revolutionized the design of electronic equipment. Using these compact, versatile circuits one can design computing power into a system wherever one needs it. A microprocessor is a complete central processor unit (CPU) on a single chip of silicon whose dimensions are measured in mere fractions of a centimetre. With one of these chips, plus a few other support chips of similar size, one can build a micro-computer system offering performance equivalent to some early computers that occupied almost an entire room, and some newer chips contain enough support circuitry, memory, and peripheral circuits to form a complete micro-computer without the addition of other chips.

Since the introduction of microprocessors their prices have tumbled to the point where unit costs of some popular types are now under £ 10. The truly revolutionary aspect of microprocessors is their versatility, which stems from their programmability. The functions of microprocessors can be changed by modifying the "software" of the same basic system. No longer do different circuits need different basic "hardware". So a microprocessor system used for data acquisition may be used for data processing without major hardware changes.

A micro-computing system for use with Fourier spectrometers for data acquisition and on line data processing has been built at Westfield college. The system is based on the Zilog Z80 eight bit microprocessor, and constructed on the IEEE S100 standard bus system

for micro-computers. The reason for choosing the Z80 and the S100 bus system is the large amount of software available for the CP/M [stands for control program for microprocessor) disc operation system which is the basic operation system used with this micro-computing system. Details of CP/M DOS will be described in this chapter.

6.2 AN INTRODUCTION TO MICROPROCESSORS

Microprocessors are a remarkably versatile new tool. They can lower the cost and increase the flexibility of electronic equipment. Together with memory and peripheral circuitry, microprocessor chips form complete microcomputers. In complexity, these micros fall somewhere between conventional minicomputers and small, hand-held calculators. They are as compact and inexpensive as calculators, but, like minicomputers, can be programed for a wide range of tasks and work with such peripheral computer devices as printers and magnetic memories.

To-day many types of microprocessor have been produced with different technology, eg. PMOS (p-channel metal-oxide semiconductor), NMOS (n-channel MOS), CMOS (complementary -MOS) etc. Regardless of the technology used, microprocessor systems are organized in basically the same way as conventional computer systems. The major blocks are a central processing unit (CPU), memory, and input/output (I/O) facilities. Within the memory there are "instructions", which are coded pieces of information that direct the activities of the CPU. The memory also holds coded data that are processed by the CPU. Typically, two kinds of memory are used for programs and data storage. The first

type is a ROM (read-only memory). In this type of memory the information can be read, but that information cannot be altered during operation or when the system is switched off. In most microcomputer systems an EPROM (erasible programmable ROM) is used, because the user can then re-program the information stored. An ultra-violet light source is usually used to erase the information stored in the EPROM. This type of memory is mostly used for basic machine operation systems or cold start loaders for some operation systems such as CP/M disc operation systems. The next type of memory is a RAM (random-access memory), which allows information to be written and modified as well as read during the operation of the program, but the contents are lost if the machine is turned off.

In operation, the CPU reads each instruction from memory and uses it to initiate various processing actions, but the CPU needs to communicate to the outside world, and usually this is done by using the I/O ports. However, some processors are designed without I/O ports, and instead use some memory locations to act as I/O ports, a good example being the Motorola M6800 processor.

In general, the operation of a CPU is very much like the system's supervisor. It fetches instructions from memory, decodes their binary contents, and executes them. During the execution of instructions the microprocessor references memory and I/O ports as necessary. It also recognizes and responds to various externally controlled signals such as reset, interrupts, etc.

Inside a typical microprocessor are incorporated various functional units to supervise and manage the operation of the system. A microprocessor CPU usually has control circuitry, an arithmetic logic unit (ALU), and a number of registers that provide temporary

storage of information. A block diagram of a simple microprocessor is shown in fig. 6.1 to illustrate the principle. A microprocessor usually has three types of bus lines for the flow of information, and these are address bus, data bus and control bus. The address bus is usually output from the CPU to the memory devices to access the memory locations, and the data bus is for exchanging information between the CPU and the memory or I/O ports. The control bus is used to define the operation of the CPU, eg. to differ between a read or write operation, etc.

The most useful register inside a CPU is the "accumulator". It can serve both as the source and as the destination register for operations involving some other registers, the ALU, or memory. Additional registers have dedicated uses, a good example of which is the program counter which keeps track of program instructions by maintaining the address of the next instruction which is stored in the memory. Each time the microprocessor fetches an instruction it increments the program counter so that it always "points" to the following instruction. The fetched instruction (in the form of operation code) goes to another dedicated register, the instruction register, and is then decoded by internal logic.

The microprocessor executes each instruction in sequence. It proceeds from numerically lower memory addresses that give the instruction to be executed early, to higher addresses that give later instructions. However, this sequential order can be broken by a "JUMP" instruction, which directs the microprocessor to a different part of the program.

Another useful instruction is the "CALL" instruction that gives rise to the execution of a subroutine. The subroutine usually consists

of a series of instructions that are to be executed repeatedly during the course of a main program. Before handling a subroutine the microprocessor has to store the returning address of the main program when the execution of the subroutine is completed. This information is usually stored in an area known as a "stack". The stack is used to save vital information, and in this case the information is the return address for the program counter, but the stack can also be used for storing contents of other registers. The return address which is stored will be used to resume the operation of the main program once the subroutine has been executed.

There may also be many more registers within the CPU for different types of microprocessor chips, but those described above are the most important and common registers one could have in a microprocessor. In the next section an outline description of the internal structure of the Z80 CPU is given.

6.3 Z80 CENTRAL PROCESSING UNIT

The purpose of this section is to discuss the structure of the Z80 microprocessor in as far as it affects the programmer, and to introduce some examples of the instruction codes in machine level code.

The microprocessor chip consists of a 40 pin large scale integrated circuit, with 8 data pins, 16 address pins and other pins for power and control purposes. Up to 64 kilobytes (one byte equals 8 bits) of memory may be directly addressed by the CPU. The stack pointer allows any portion of RAM to be used as an external stack, so

that subroutine nesting is only limited by the size of the memory. The stack can be used to store the contents of the program counter, flags, accumulator and all the other general purpose registers.

The arithmetic logic unit (ALU) performs addition, subtraction, logical functions of ANDing, ORing and exclusive ORing, and shifting operations between two 8 bit operands. In addition, binary-code decimal (BCD) operations may be performed.

There are fourteen general-purpose 8 bit registers within the Z80 CPU, which are designated as A, B, C, D, E, H and L and A', B', C', D', E', H'and L'. Only one set of the seven registers and the corresponding flag register F or F' can be accessed at any given time. Thus, a special Z80 instruction is provided to select A and F or A' and F', and another instruction is provided to select B, C, D, E, H, L or B', C', D', E', H',L'. A block diagram of the register set is shown in fig. 6.4.

In general the accumulater (A register) is the main register for performing arithmetic and logical operations. The other six registers can be grouped to form three register pairs for sixteen bit operations, eg. BC, DE and HL. These register pairs can be used as memory pointers, and to perform sixteen bit precision arithmetic etc. The sixteen bit precision arithmetic involves adding, subtracting, incrementing, or decrementing a sixteen bit value.

The special-purpose registers are the I (interrupt vector register), R (memory refresh register), IX, IY (index registers). The application of these registers will not be discussed here, because they are used in rather special circumstances by the programmer, so for those who want to know more about these registers, the Z80 programming manual is a good reference to read [Z80 Assembly Language

Programming Manual].

The Z80 has a wide range of instructions, ranging from a simple instruction to add two registers to a block search instruction. Because of the wide range of functions that Z80 instructions perform, instructions range in length from one byte to four bytes. In addition to this, instructions also differ in how external memory is addressed. In general there are ten addressing modes for the Z80 CPU, and they are listed below:

1) Implied addressing

In this addressing mode, the operation code of the instruction fixes the source and destination of the instruction.

eg. LD E,A ; load register E with the value in register A , this op-code is 5F hex.

2) Immediate addressing

In this addressing mode, the second or third byte of the instruction itself is the operand.

eg. LD A, 02H ; load register A with the value 2 hex. where the first byte is the op-code and the second byte is the value 2 hex. i.e. 3E 02 in hex.

3) Extended immediate addressing

In this addressing mode, the second and third bytes are the operand giving a sixteen bit value.

eg. LD HL, 8000H ; means load register pair HL with the value 8000 hex, where the first byte is the op-code, and the second and third bytes contain the value 8000 hex. eg. 21 00 80 in hex. code.

4) Resister addressing

This addressing mode is similar to the implied addressing mode, except that the instruction would contain a field which specifies which register is to be utilized in performing the instruction.

eg. RL A ; means rotate register A (or other registers) to the left.
i.e. CB 17 in hex. code.

5) extended addressing

In this addressing mode the instruction holds the address of the data in the instruction format, i.e. the second and third byte of the instruction code.

eg. LD A, (1000H) ; means load the content store in the memory location 1000 hex.
i.e. 3A 00 10 in hex code.

6) register indirect addressing

In this addressing mode one of the register-pairs is used as a pointer for the memory location.

eg. LD A, (HL) ; means load the content store in the memory location indicated by the register pair HL.
i.e. 7E in hex code.

7) Relative addressing

In this addressing mode the sequence of the instruction can jump to a location relative to the present address.

eg. JR 16H ; means jump to location 16 hex forward.
i.e. 18 16 in hex. code.

8) Index addressing

In this addressing mode one of the index registers is used as a pointer.

eg. LD (IY+6), 88H ; means that the value of 88 hex will be stored in the location indicated by the register IY plus 6 position.

i.e. FD 77 06 in hex. code.

9) Bit addressing

In this addressing mode the instruction specifies any one bit of the 8-bits in an operand for either testing, setting, or resetting etc.

eg. SET 1, B ; means set bit 1 of register B

i.e. CB C8 in hex. code.

10) Page zero addressing

This addressing mode is used only by one instruction, the RST P. In effect, this instruction is to cause a branch to one of the eight page zero locations after pushing the content of PC into the stack.

One nice feature of the Z80 CPU is that it is software compatible with the early type 8080A CPU, an eight bit processor produced by Intel Inc. As there is lots of software written for this processor, the advantage of Z80 is that it can execute at a clock speed of 4MHz instead of 2MHz. Thus a speed advantage of two is achieved. The execution speed can also increase if the special Z80 instruction code is used. This means that the Z80 can execute 8080A software at twice the speed of 8080A.

6.4 OPERATING SYSTEM

Another reason for choosing the Z80 CPU is that one of the most popular disc operating systems (DOS) for the microprocessor CP/M is written in 8080 code. CP/M is a single-user, single-task disc operating system. Essentially, it provides a user interface to a diskette file system, and simple input output routines. CP/M itself consists of four sections plus user's programs, and a block memory map of the system is shown in fig. 6.5. The I/O and diskette control handlers are called the basic input output system (BIOS), and are different for different hardware configurations, but the main body of the CP/M does not care about the configuration of the system hardware as long as the subroutines in BIOS pass the right parameters. Thus this enables software produced on one machine to be used on other machines if they have the CP/M system.

The file manager is included in the basic disc operating system (BDOS). This section of the system has facilities to open a file, close a file, plus other routines.

Upon switch on, the bootstrap loader (stored in an EPROM) loads the CP/M core into RAM where it remains while the computer is switched on. The console command processor (CCP) will wait for commands to be typed in from the console (usually a VDU) and then executes. The CCP offers five basic commands; they are given as follows:

1) DIR --- lists the names of files on the named disk.
2) ERA --- erases a named file or files.
3) REN --- re-names a file.
4) SAVE -- copies N 256-byte blocks of memory from location 100 hex onto disc and calls the file name.

5) TYPE -- prints out a named file onto the screen.

CP/M thinks that any other command you type in except the above five is the name of a file which it will try to load and execute. Within the system software package there are a few more programs which one could use. These programs are listed below:

STAT --- reports the free space on disc, or if a name of file is given, it will report the size of that file.

PIP --- (peripheral interchange program) enables one to transfer files from one place to another. One could use it to copy files from one disc to another, etc.

MOVCPM --- re-adjust CP/M for your memory size.

SYSGEN --- creates CP/M system on a new disc; usually CP/M is stored on the two outer tracks of the disc.

ASM --- an 8080 type assembler.

LOAD --- creates an executable disc file from the hex file produced by the ASM assembler.

DDT --- a machine-code debugger.

ED --- the system text editor used to create a source program for high level language etc.

Due to the complexity of the Fourier transform and associate programs, it is very time consuming to write them in machine code. Therefore, a high level programming language is used. This is one of the big advantages of using CP/M operating systems because there are a large number of high level programming languages available such as BASIC, FORTRAN, ALGOL and PASCAL, etc. In this development work PASCAL is used. Thus all the data processing programs, i.e. fast Fourier transform routines, etc, have been written in this programming

language, but the data acquisition program was written in machine code, so as to maximize the use of the RAM space so that as many as 24 thousand sampling points can be recorded for special applications.

6.5 INTERFACING THE MICROPROCESSOR SYSTEM WITH A FOURIER SPECTROMETER

In order to interface a microcomputer to the outside world, it is necessary to input sensory data into its memory or register. Since most sensory data encountered in our environment are analogue in nature, they must be converted to digital values before the microprocessor can understand them. This conversion process is accomplished by an analogue to digital (A/D) converter as an interface between the microcomputer and the analogue signal. In this case the analogue signal is the output signal from the PSD.

In general, there are three basic types of A/D converters : ramp, successive approximation, and tracking. First in the order mentioned is the ramp converter which uses a count up method of conversion and is best suited for very slowly changing data. The major drawbacks to this type of converter are its extremely slow speed of 2 clock pulses per conversion, and that data can only be taken out at the end of the conversion cycle. The second type of converter is the successive approximation A/D converter. This type is the most expensive as it requires additional data holding circuits, but then it is the fastest type of converter which requires only one clock pulse for each bit of resolution. The major disadvantage associated with this type of converter other than its high cost is its method of sampling the input

signal and then making a quick approximation of what it might be, since the input signal is only sampled every N clock pulses. The output from this type of converter can only be read at the end of the conversion cycle. The third type is the tracking A/D converter. This unit is a compromise between the first two types of converter. Essentially this type locks on to the input analogue signal and as long as the slew rate of the loop does not exceed the digital output, it will equal exactly the analogue input within the resolution limit of the converter. If the slew rate is exceeded, the output immediately becomes erratic and you need an adjustment.

A block diagram of the microprocessor system built for the data acquisition and on line data processing is shown in fig. 6.6. Basically it consists of a Z80 CPU, running at 4MHz clock speed. It has a full 64K bytes of RAM, plus an EPROM cold bootstrap loader, two floppy disc drives for magnetic storage, and a VDU for the command console. The printer and graphic plotter are used for outputting the spectrum and numerical data, etc. The vital part of the system is the interface link between the spectrometer and the microprocessor.

In the design of the A/D interface, a 12 bit converter made by Hybrid System Corporation with model number ADC 581 is used. It uses the successive approximation method with a convertion time of 17 us for full 12 bit conversion and it has 5 input voltage ranges. In order to maximize signal resolution using the A/D converter, the analogue input has been scaled as close to the maximum input signal range as possible. In this case we have selected the 0-10V range, as this is the output voltage range from the PSD.

The circuit diagram of this interface is shown in fig. 6.7. Since the A/D converter is only 12 bits wide, we used one input port for the

lower 8 bits and another port for the top 4 bits. Hence, there are 4 unused bits in the second port. Therefore, we connected the status line signal onto one of these lines. Thus, this will simplify the hardware design and enable the interface board to use only two I/O ports, and we have assigned them as 80 and 81 hex. addresses.

The interface board consists of address and control decoding from the CPU, and also data lines for transferring data to the CPU. The board uses two I/O port addresses at 80 and 81 hex. The address decoding is done by IC1, and IC2 (see fig. 6.7). Because the Z80 can address up to 256 I/O ports, i.e. 8 addressing bits, IC2 is used to decode the top 4 address bits. Thus if and only if the top 4 address bits equal 8 hex., the output from IC 2 will be low. This then switches on the enable line of IC 1, which is a 4 to 16 line decoder chip. This is used to decode the lower 4 address bits, so gives 16 independent I/O ports on the board, but only two are used in the present design. Since the CPU uses the same address lines for memory and I/O ports, some signal is used to differentiate between memory and I/O instructions. This is done by decoding the S100 bus signal "SINP". This signal is used to inform devices that it is a reading from an input port cycle. i.e. the addressing lines contain the address of the input port to be read by the CPU. As the enable gate of the decoder chip (IC 1) is an active low signal (enable when voltage level is zero), an inverter gate is necessary to invert the active high (enable when voltage level is +5V) SINP signal.

When the ADC 581 receives a triggering signal, the status line (pin 20) remains low until the conversion is done. This status line is then used to clock a D type flip-flop (74LS74 IC 3), and the latched signal from IC 3 is fed to the second input port. This is used to

inform the CPU that the data is ready from the ADC chip. In order to avoid the CPU reading the same data again, the flip-flop is reset when the data is read, i.e. the enable 1 signal is used to reset the flip-flop IC 3. The power on reset signal is also gated to reset the flip-flop so that when the power is switched on the interface is always in the reset status. Thus the reading of false data is avoided.

IC 6 and 7 are 8 bit tri-state buffers, which are controlled by the two enable lines 1 and 2. These buffers will only turn on when the CPU wants data from these decoded input ports.

The program for reading the data from the ADC board is executed by the "polled method", i.e. the status of the ADC chip is observed and tested in a loop before the data is read. This method is most time consuming but offers very simple hardware design, as one can see from the circuit diagram. The procedure for inputting data from the ADC board is shown in the block diagram fig. 6.8, and the subroutine for reading the data into RAM is also listed in Z80 Assembler symbols in fig. 6.9 as an example.

All the sampling data are stored in RAM first, then once the scan is finished all the data is transferred onto disc file under CP/M format. We have stored the data in a format that is compatible with the integer type of file of the Pascal compiler, thus the Fourier transforming program which is compiled by the compiler can read the data without any problems. The Fourier transform programs provide apodization, ratioing, and plotting functions etc. With all these facilities this on-line data processing system provides a very useful tool for analysing the raw data from the Fourier spectrometers.

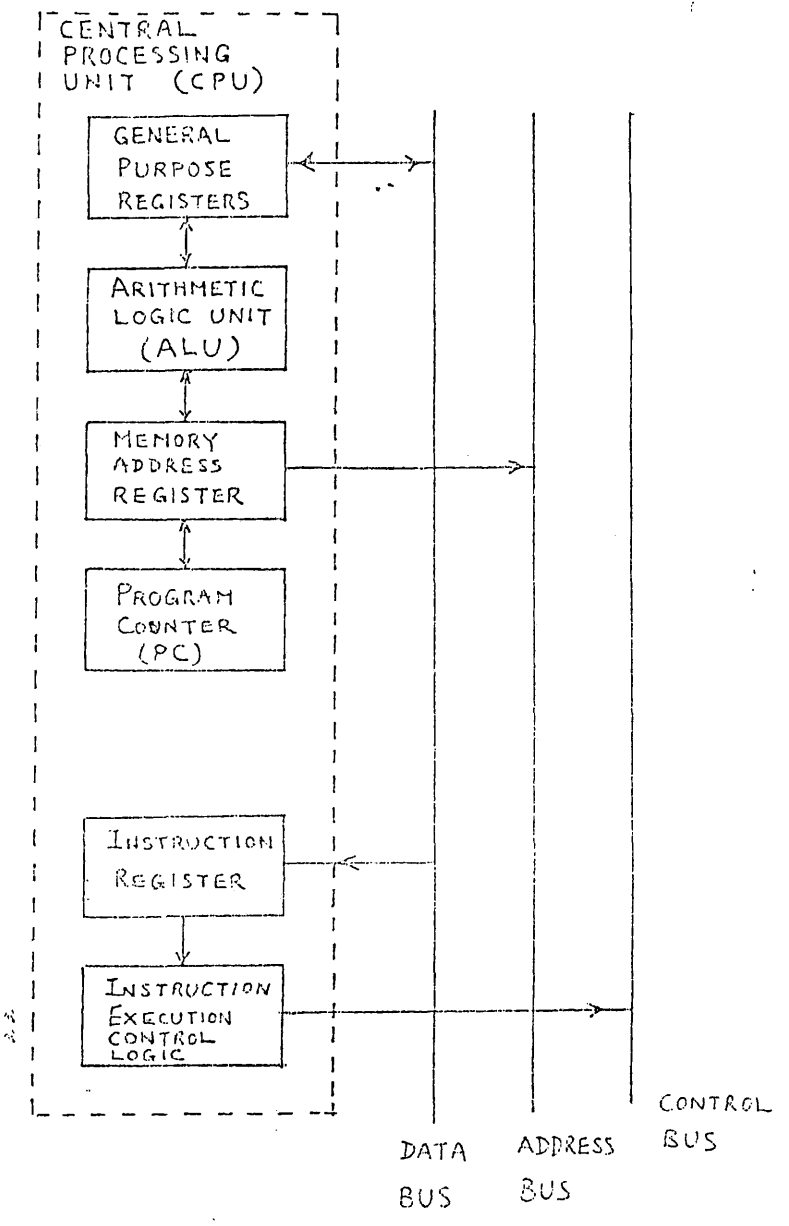

Fig. 6.1 A block diagram of a simple microprocessor: three buses are generally needed to provide communication between the microprocessor memory and the I/O devices.

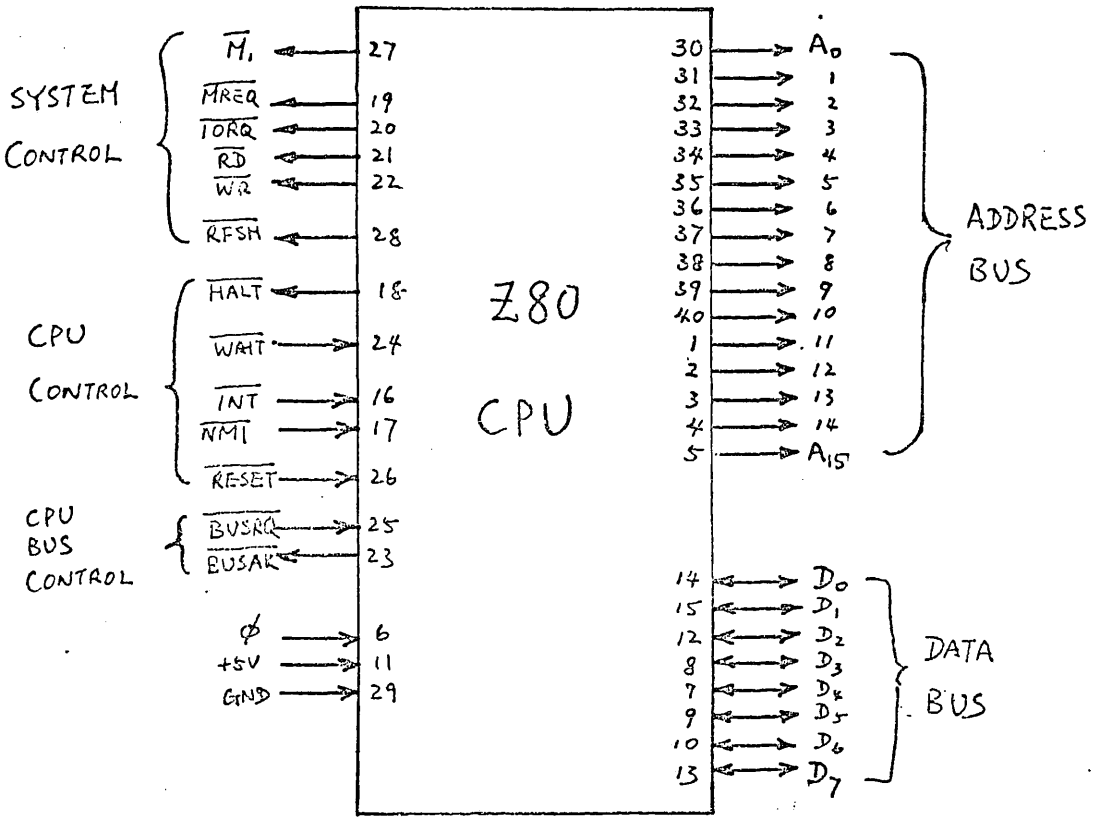

Fig. 6.2 A pin diagram of the Z80 CPU chip.

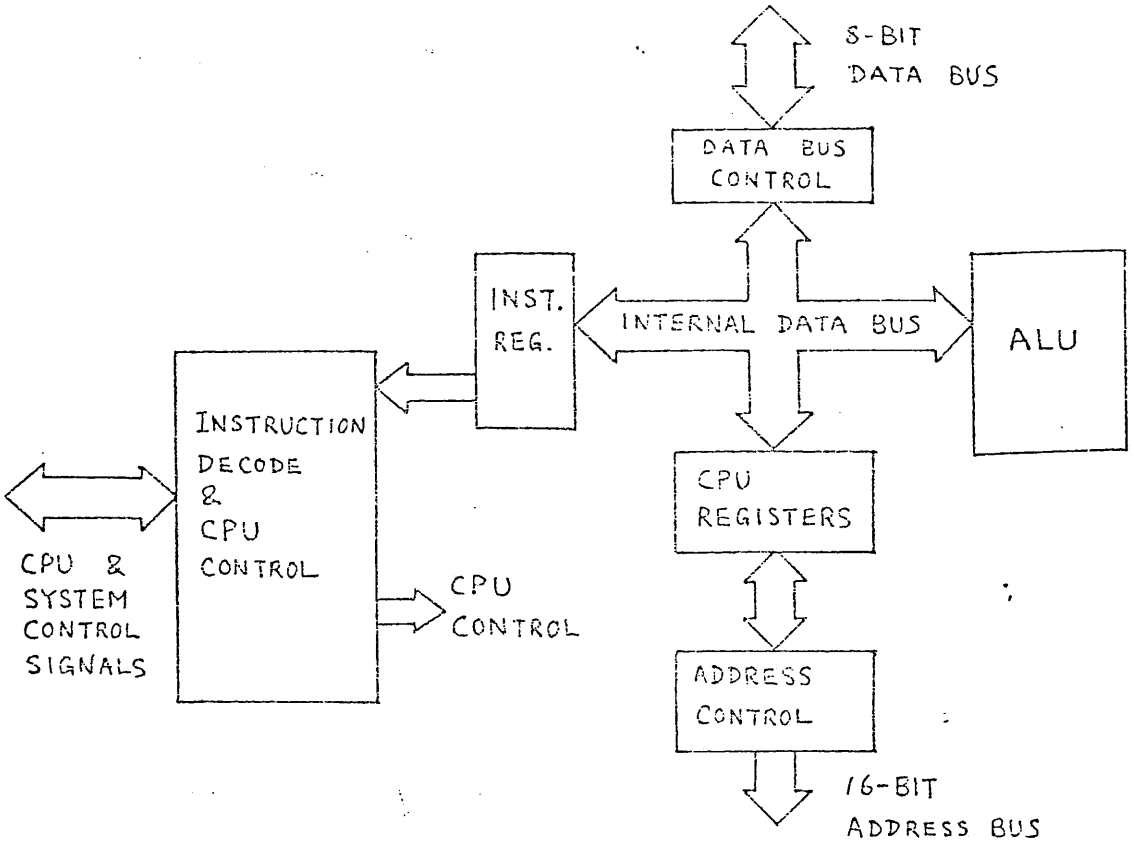

Fig. 6.3 Internal structure of the Z80 CPU.

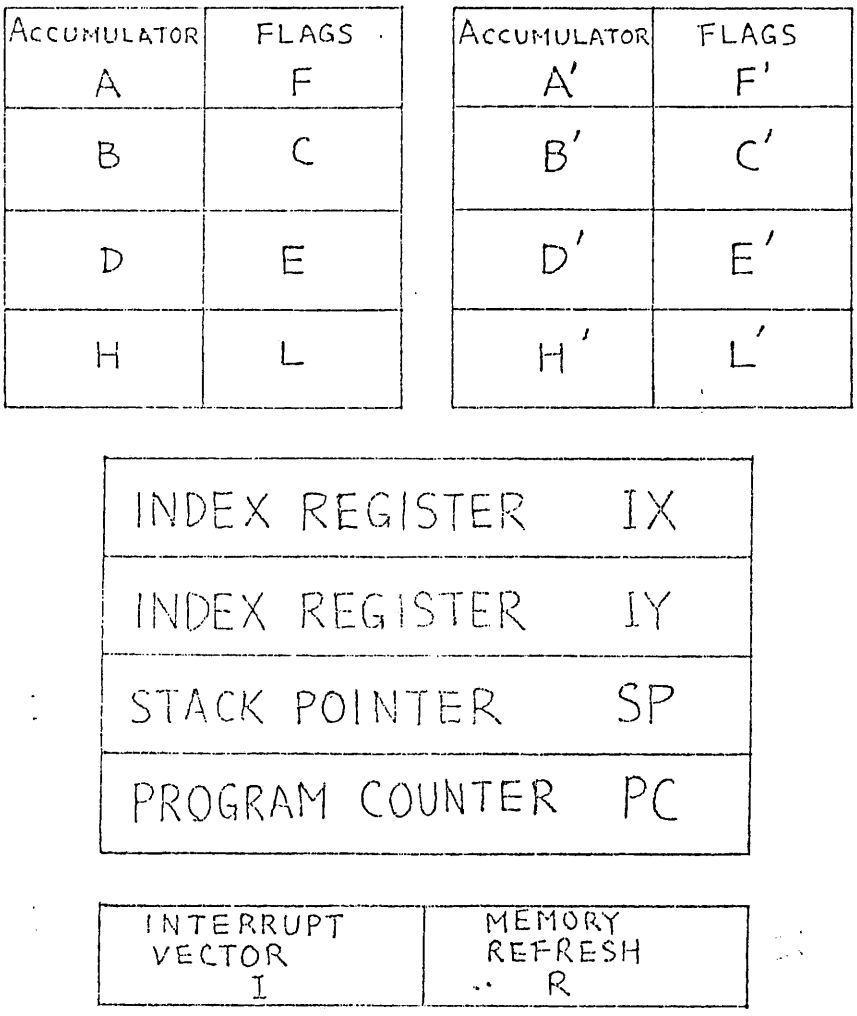

Fig. 6.4 Z80 registers set.

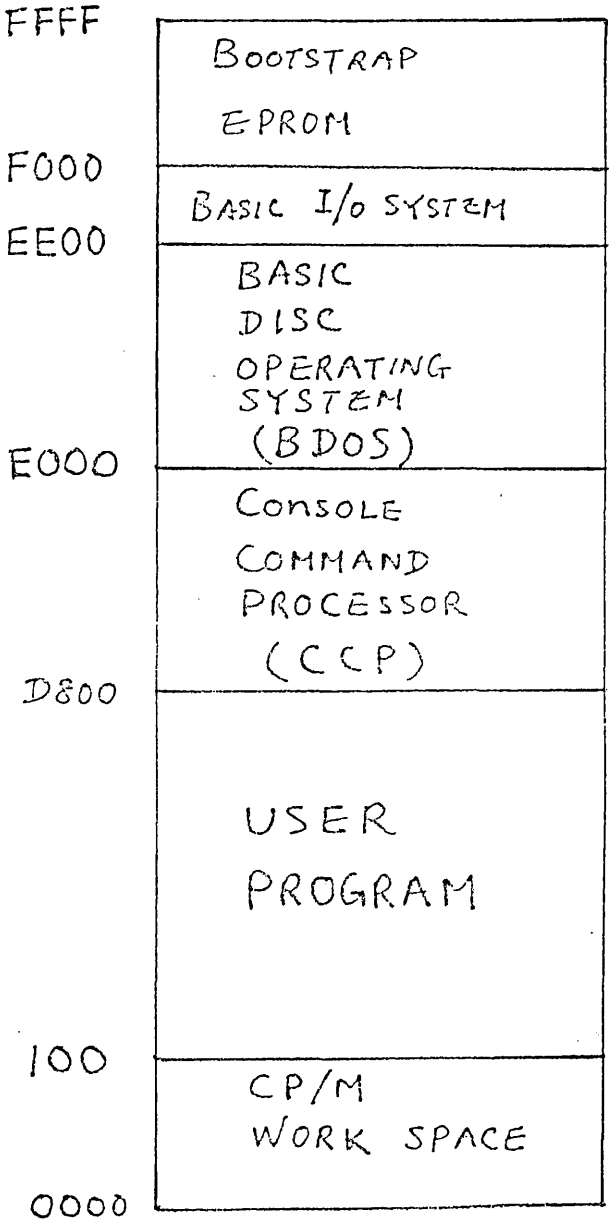

Fig. 6.5 A memory map of the CP/M disc operating system used in the microprocessor system.

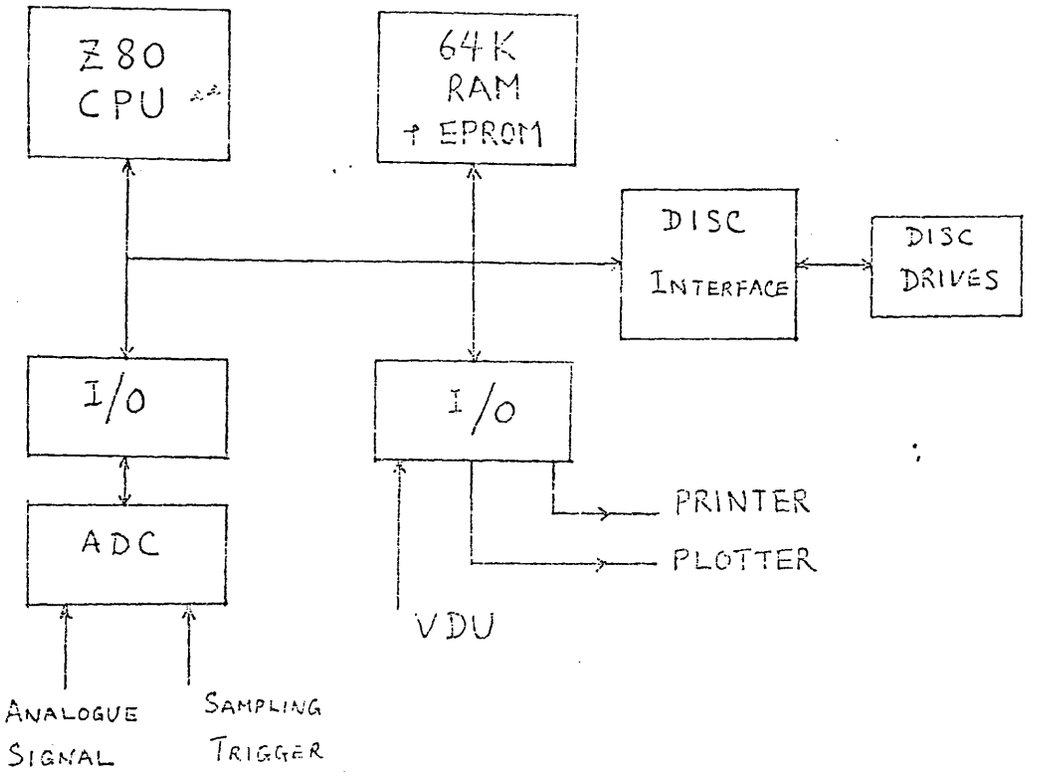

Fig. 6.6 A block diagram of the microprocessor system used with the Fourier spectrometer.

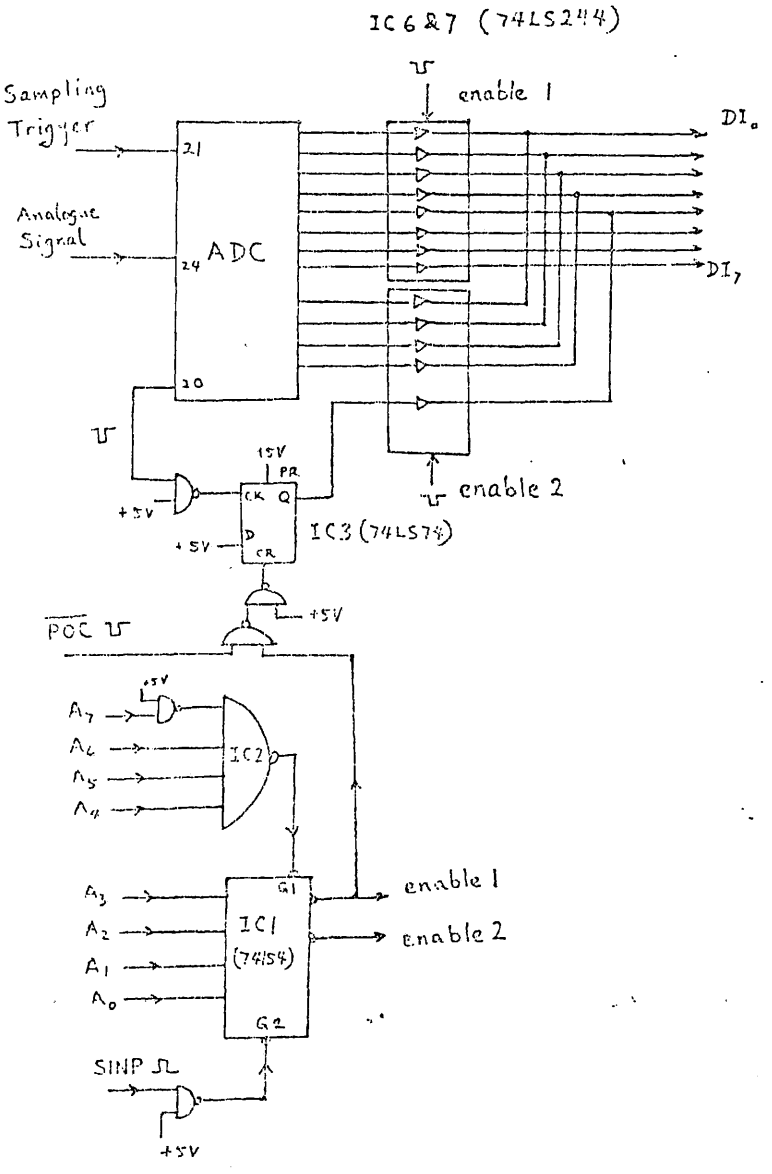

Fig. 6.7 A circuit diagram of the ADC interface board.

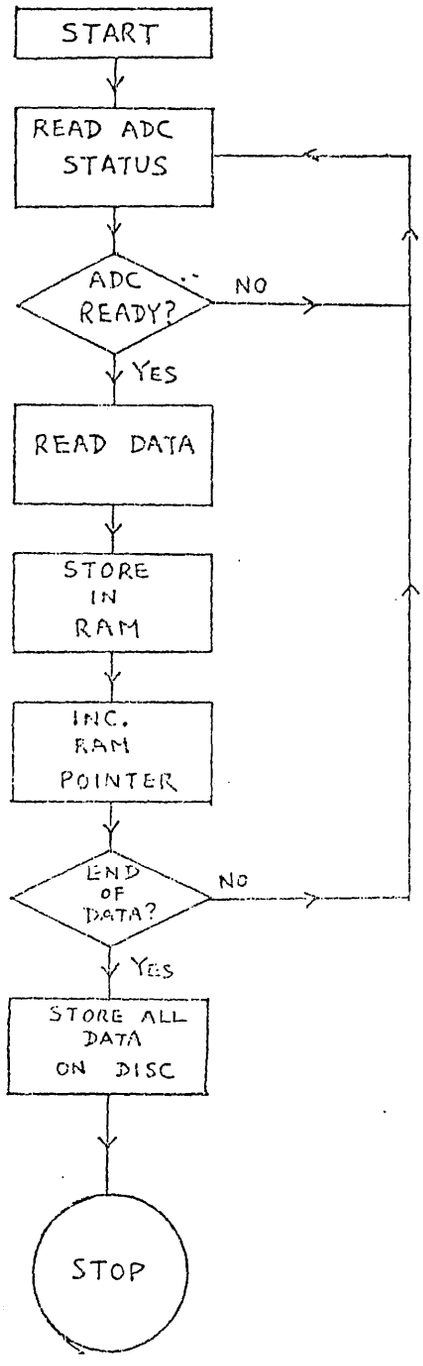

Fig. 6.8 A flow chart of the procedure for reading data from the ADC board.

```
Z80 Assembler  ZASM V1.2                    Subroutine for read data

  1                ;Subroutine for read data
  2                ;from the ADC board.
  3
  4                RAM:    EQU  2000H      ; RAM address
  5                PORTA:  EQU  80H        ; Port A address
  6                PORTB:  EQU  81H        ; Port B address
  7                NPOINT: EQU  200        ; Set for 200 points
  8
  9                        ORG  1000H
 10
 11 1000 2A0020   READ:   LD   HL,(RAM)   ; load HL with storge
 12                                       ; storge address
 13 1003 06C8             LD   B,NPOINT   ; load B with number of
 14                                       ; points to be read
 15 1005 DB81     LOOP:   IN   A,(PORTB)  ; input the second port
 16                                       ; into reg. A
 17 1007 E610             AND  10H        ; Check ADC ready line (bit 4
 18                                       ; is used) this bit is high
                                          ; when ready.
 19 1009 28FA             JR   Z,LOOP     ; If not ready then loop.
 20                                       ; until ready.
 21 100B E60F             AND  0FH        ; Remove top 4 bits because
 22                                       ; they are not data.
 23 100D 77               LD   (HL),A     ; Save this data into RAM.
 24 100E 23               INC  HL         ; Increment the RAM pointer.
 25 100F DB80             IN   A,(PORTA)  ; Now read the other 8 bits.
 26 1011 77               LD   (HL),A     ; Save into RAM.
 27 1012 23               INC  HL         ; Increment the RAM pointer
 28                                       ; for next loop.
 29 1013 10F0             DJNZ LOOP       ; Decrement reg. B and if it
 30                                       ; is not equal to zero then
                                          ; jump to loop.
 31 1015 C9               RET             ; If reg. B equals zero then
 32                                       ; return to main program.
 33                       END
```

Fig.6.9 A sample program for input data from the ADC board.

CHAPTER 7

EXPERIMENTAL MEASUREMENTS

7.1 PRODUCTION OF FREE-STANDING TUNGSTEN WIRE GRIDS

All the tungsten wire grids were made at the National Physical Labaratary using a modified coil winder. A set of grids with different wire spacings have been wound from 10 μm diameter wire using a technique described by Costley et al [1977], but with 5μm diameter wire modifications had to be made to the winding apparatus because the wire is much finer and breaks easily.

The main alterations in the winder are as follows:

1) The tension of the wire has been reduced from 22g to 3g by adjusting the slipping clutch of the coil winder.

2) The wire has been made to by-pass all the pulleys in the constant head tension device made for 10 μm wire, and only passes around the pulley on the tension arm. However, this appears to have no deleterious effects on the wire spacing. This procedure is necessary to prevent breakage.

3) The lead screw driving the wire grid has been changed to a finer one with 40 turns/in which gives a smaller wire spacing.

4) The wire grid former on which the grid frames are mounted during winding has been redesigned. The new former is smaller than that for 10 μm grids to reduce the waste of wire when winding small 5 μm grids, and this also gives a better continuous tension for the wires during winding. To help with this tension problem, the two sides of the former are made from glass rods, so that the wire only passes over the smooth surface of the glass rod.

5) The winding speed has been reduced from 4 rpm to 2 rpm to reduce the tension of the wire.

With the above modifications, the winder is able to produce 5 μm wire grids with apertures of up to 60mm diameter for use as beam dividers in interferometers. Such beam dividers have been made with 12.5μm wire spacing for use in the transmission instrument, and the results will be described in this chapter.

7.2 TRANSMISSION COEFFICIENT OF 10 um WIRE GRIDS

1) Measurements made by Laser

The first set of experiments to measure the power transmissiom of the thin wire grids was made with an HCN laser. This laser produced radiation at a frequency ν =29.7 cm^{-1} (λ =337 μm). The ouput radiation from the laser was incident at 45° on a mylar beam divider (See fig. 7.1). The transmitted beam from the beam divider was polarised by passing it through a commercial substrate-mounted polariser, P, and thereafter incident normally on the free-standing wire grid, and the transmitted radiation from the wire grid was then focussed onto Golay detector No.1 by the polythene lens. The beam initially reflected by the beam divider was focussed onto another Golay, G2, by the polythene lens, L2. The mounting for the wire grid specimen was designed to rotate to obtain the minimum transmission output, and the unit could be removed from the radiation beam.

The signals from G1 and G2 Golays were ratioed electronically by

an electronic ratiometer amplifier. Hence the error due to the power level drift of the laser beam was reduced. The power transmission of the sample grid for $\underset{\sim}{E} \| \underset{\sim}{S}$ was measured by rotating the grid until minimum transmission was achieved, and then the grid was removed from the beam to read the output of the laser beam. The ratio of the minimum transmission output against the incident power signal would give the power transmission coefficient, $T_{\|}$, of the sample grid for $\underset{\sim}{E} \| \underset{\sim}{S}$. This procedure was repeated for wire grids with spacings in the range 30-65um. The results are compared with the theoretical predictions based on the method described in Chapter 4 in fig 7.2, and it can be seen that there is excellent agreement between experiment and theory.

2) Measurements by Fourier Transform Spectrometry

The power and phase transmission spectra (T, ϕ) of a selection of grids were measured at normal incidence in the frequency range 20-450 cm^{-1} by a combination of conventional Fourier transform spectrometry and dispersive Fourier transform spectrometry. All transmission measurements were made by using the single pass instrument described in Chapter 5. The sample grids used in the laser measurement were remounted on a smaller aperture frame which could be slid in and out of the radiation beam in the interferometer. Measurements were made for both orientations of the wire grid, i.e. electric vector, $\underset{\sim}{E}$, parallel to the wires, $\underset{\sim}{E} \| \underset{\sim}{S}$, and perpendicular to the wires of the grid, $\underset{\sim}{E} \perp \underset{\sim}{S}$.

Due to the low efficiency at low frequencies of interferometers

using mylar beam dividers, for measurements at frequencies below 125 cm^{-1} the interferometer was converted to the polarising mode. The conversion was done by placing free-standing wire grids between the collimator and the beam divider, and between the beam divider and the polyethylene lens doublet, both grids with their wires vertically oriented. These wire grids acted as the polariser and analyser for the interferometer. The most important component is the beam divider, and this was replaced by another wire grid but with the wires oriented at 45^{o} to the electric vector of the incident radiation. All the wires were wound from 10 μm diameter tungsten wires with 25μm wire spacing. For the measurements at higher frequencies the beam divider was replaced by 6.25um thick mylar, and commercial substrate mounted polarisers efficient throughout the measured range were used to replace the wire grid polarisers. This enabled the instrument to be used up to a frequency of about $400cm^{-1}$.

The sample grids were mounted onto a copper ring with an aperture of 1.5cm and the wires were fixed with "Durofix" adhesive onto this ring. Wire grids with spacings d=55, 45, and 35 μm were measured, and the results are plotted in figs 7.3, 7.4, and 7.5 respectively. The resolution of the measured spectra was 4 cm^{-1}, but only sufficient points have been plotted to illustrate clearly the structure present in the spectra. On each figure the calculated power transmission coefficient, $T(\nu)$ and phase coefficient, $\phi(\nu)$ are also plotted for comparison.

There appears to be a reasonable agreement between experiment and theory for all three grids except in the region near the diffraction peaks at $d/\lambda = 1$, i.e. in the region B on the graphs. Only in the case of the grid with d=55 μm (fig 7.5) were measurements made near the

region where $d/\lambda = 2$, but it is clear that the predicted structure was not present. For the other two grids, this region near $d/\lambda = 2$ was outside the measured frequency range, so no comparison was possible.

For the case of $\underline{E} \| \underline{S}$, one can see the predicted high transmission near $d/\lambda = 1$. The discrepancies between experiment and theory in this region seem to get more serious as the spacing of the grid decreases. The reason for such discrepencies is believed to be due to the irregularities in the wire spacing. In order to investigate this possibility, the spacing of the wire grids was measured by using a microscope. The measurements of the individual spacings over about 150 periods for these three grids were recorded, and the mean spacing, $\bar{d}$, the standard deviation, σ, and the ratio of $\sigma / \bar{d}$ were calculated for each grid by using the well known formulae given below

$$\sigma = \frac{\sum (d - \bar{d})^2}{n - 1}$$

$$\bar{d} = \frac{\sum d}{n}$$

where n is the number of data points. The results of all the grids are shown in Table 6.1.

If one observes the value of σ, it can be seen that in each case it is a significant fraction of $\bar{d}$. The value of the ratio, $\sigma/\bar{d}$ increases as $\bar{d}$ decreases. This correlates very well with the observation in figs 7.3 - 7.5 that the discrepencies between experiment and theory increase as $\bar{d}$ decreases, so it is probable that these discrepencies are indeed due to the irregularities in the grid spacings.

7.3 MEASUREMENTS ON 5 μm WIRE GRIDS

By improving the winding technique used for the production of 10 μm wire grids, 5 μm diameter tungsten has also been used to produce free-standing wire grids. Three sets of wire grids have been made for measurements of amplitude and phase transmission coefficient. They had wire spacings of d=100, 50, and 25 μm. The measurements for these grids were made by using the same single pass instrument described earlier, but with a few components changed. The beam divider used was made from 6.25 μm mylar, and commercial substrate mounted polarisers were used to select the desired component of polarisation for the measurement of complex amplitude transmission coefficient. The results are shown in figs 7.6 to 7.8. When one looks at the results of the theoretical work, one can see that for a perfect grid at normal incidence the transmission amplitudes are close to unity for both polarisations near the frequencies where $d/\lambda = 1$, or 2, where $\lambda = 1/\nu$ is the wavelength, and d is the wire spacing.

The theoretical calculations of the amplitude and phase transmission coefficients of the grids were carried out assuming regular spacing of the wires. Although the theory takes account of absorption in the wires, it has been found that the effect of their finite conductivity is negligible at the frequencies of interest. The calculations have been carried out for the two simplest configurations of plane polarised radiation with the electric vector parallel and perpendicular to the grid wires. The results are plotted in each case with the measured results in the same graph for easy of comparison.

7.4 MEASUREMENTS ON CRYSTALLINE SOLIDS

The main application of dispersive Fourier transform spectrometry described in this thesis is to determine the optical and dielectric functions of solids in the far infrared region. In general, the optical constants and dielectric functions can be calculated from the complex insertion loss $\tilde{L}(\nu)$ by using the well known Fresnel relations. The determination of the complex insertion loss for the two interferometers has been described in Chapter 3.

The specimens measured by the transmission and reflection instruments were alkali halide crystals. These crystals have the face-centred cubic diatomic ionic crystal structure, and disperson due to lattice vibrations occurs in the measuring range of these instruments. The analysis of lattice vibrations in such crystals has been described in the harmonic approximation by a number of authors [Born and Huang 1966, Donovan and Angress 1971].

In this chapter an outline of the dispersion relations is given, and the results of the measurements on KCl and KBr crystals using the two instruments are also presented.

a) Infrared dispersion by cubic diatomic cryatals

In this section, an outline of the dispersion of the dielectric function due to lattice vibrations is given. The crystal structure described is face-centred cubic which is the structure of some alkali halide crystals. If the crystal structure has n atoms per unit cell,

the frequency ν (in cm^{-1}) has 3n branches. Three of these branches are called acoustic modes which have the property of $\nu_i(q) \to 0$ as $q \approx 0$. In fact, the atoms in the unit cell move in the same direction with the same amplitude, which at long wavelengths is analogous to the propagation of an elastic wave. The remaining 3n-3 branches are called optic modes, which have non-zero values of $\nu(q)$ as $q \approx 0$. In cubic diatomic crystals, there are two atoms per unit cell, hence, there are six branches, three accoustic and three optic modes.

The vibrations of a diatomic lattice are produced by the movement of the two different types of atoms in the crystal. Any resultant electric moment will interact with the electric field of an incident electromagnetic wave. The long wavelength acoustic vibrations are identified as elastic waves, and therefore can be described by macroscopic equations. However, the theory of optical vibrations ($q \approx 0$) was developed by Huang [1951]. In his treatment, he used two expressions to relate the macroscopic electric field E, and relative displacement of the two atoms in the unit cell, i.e.

$$\begin{aligned} \ddot{\underline{W}} &= b_1 \underline{W} + b_2 \underline{E} \\ \underline{P} &= b_2 \underline{W} + b_3 \underline{E} \end{aligned} \qquad (7.2)$$

$\underline{W}$ is the reduced vector, and expressed as

$$\underline{W} = \underline{U} / \overline{M} \qquad (7.3)$$

where $\underline{U}$ is the displacement of the positive ion relative to the negative ion, and $\overline{M}$ is the reduced mass of the positive and negative ions.

A solution can be obtained by taking $\underline{W}$, $\underline{E}$, $\underline{P}$ to be varying

periodically with time in the form $\exp(-i\nu t)$. By eliminating the function $\underline{W}$ from the equation of motion above, we have

$$\underline{P} = \left\{ b_3 - \frac{b_2^2}{b_1 + \nu^2} \right\} \underline{E} \qquad (7.4)$$

where the polarization $\underline{P}$ is related to the electric field E with the expression

$$\underline{P} = \chi \underline{E} \qquad (7.5)$$

where χ is the electric susceptibility, and the dielectric constant is related to χ as

$$\varepsilon = 1 + 4\pi\chi \qquad (7.6)$$

Thus, from equations (4) and (5) the value of becomes

$$\chi = b_3 - \frac{b_2^2}{b_1 + \nu^2} \qquad (7.7)$$

Hence, the dielectric function is obtained as

$$\varepsilon = 1 + 4\pi b_3 - \frac{4\pi b_2^2}{b_1 + \nu^2} \qquad (7.8)$$

By substituting the time variation functions of $\underline{W}$, $\underline{H}$, $\underline{P}$ and $\underline{E}$, into Maxwell's equations, this gives the condition that

$$\varepsilon(\nu)\ (\underline{q}.\underline{E}) = 0 \qquad (7.9)$$

which leads to two alternative possible solutions.

1) Longitudinal waves

If $\underline{W}$, $\underline{P}$, $\underline{E}$ and $\underline{q}$ are all parallel the resulting vibration is a longitudinal wave. Since $\mathcal{E}(\nu)=0$, this gives

$$0 = 1 + 4\pi b_3 - \frac{4\pi b_2^2}{b_1 + \nu_L^2} \tag{7.10}$$

thus

$$\nu_L^2 = -b_1 + \frac{4\pi b_2^2}{1 + 4\pi b_3} \tag{7.11}$$

where ν_L is independent of q.

2) Transverse wave

If $\underline{W}$, $\underline{P}$ and $\underline{E}$ are parallel, but perpendicular to $\underline{q}$, the resulting vibration is a transverse wave, i.e.

$$(q/\nu)^2 = \mathcal{E}(\infty) + \frac{\mathcal{E}(o) - \mathcal{E}(\infty)}{\nu_o^2 - \nu^2}\nu_o^2 \tag{7.12}$$

where $\mathcal{E}(\infty) = 1 + 4\pi b_3$

$$\mathcal{E}(o) = 1 + 4\pi b_3 + \frac{4\pi b_2^2}{\nu_o^2}$$

$$b_1 = -\nu_o^2$$

where ν_o is the natural frequency of this transverse mode. Hence, for a given value of q, equation (12) has two solutions, and there are two alternative orientations of q with respect to $\underline{E}$ which still maintain their mutual orthogonality. Thus , there are four independent

transverse vibrational modes.

However, the dispersion relation can be generally expressed as

$$\mathcal{E}(\nu) = \mathcal{E}(\infty) + \frac{(\mathcal{E}(0) - \mathcal{E}(\infty))\nu_0^2}{\nu_0^2 - \nu^2} \qquad (7.13)$$

Hence, by using this dispersion relation, we may calculate the corresponding reflection spectra from the Fresnel relations.

As the frequency increases, the refractive index N increases steadily, but as the frequency ν reaches the dispersion frequency ν_0, $\mathcal{E}(\nu)$ becomes infinite, hence N becomes infinite, and the resulting reflectivity becomes unity; i.e. the crystal becomes a perfect reflector. When the frequency passes this point $\mathcal{E}(\nu)$ is negative until it becomes zero again when the frequency is equal to ν_L, the longitudinal optic mode (LO) frequency. The value of $\mathcal{E}(\nu)$ is negative between the frequencies ν_0 and ν_L, thus the refractive index N is imaginary and gives a band of perfect reflection. This band is known as the reststrahlen band.

When at frequency ν_L, the function $\mathcal{E}(\nu)$ is equal to zero, i.e.

$$0 = \mathcal{E}(\infty) + \frac{(\mathcal{E}(0) - \mathcal{E}(\infty))\nu_0^2}{\nu_0^2 - \nu_L^2} \qquad (7.14)$$

from this we can obtain the well known relationship between ν_0 and ν_L

$$\frac{\nu_L}{\nu_0} = \left(\frac{\mathcal{E}(0)}{\mathcal{E}(\infty)}\right)^{1/2} \qquad (7.16)$$

the Lyddane-Sachs-Teller (LST) relation.

Experimental results for a real diatomic cubic crystal show that the reflection in the reststrahlen band does not agree quantitatively

with the simple crystal model described above. A closer approximation to the dispersion relation is obtained by including a damping term in the equation of motion, i.e.

$$\ddot{\underline{W}} = b_1 \underline{W} - \gamma \dot{\underline{W}} + b_2 \underline{E} \qquad (7.16)$$

This gives the dielectric function as

$$\varepsilon(\nu) = \varepsilon(\infty) + \frac{\nu_0^2 (\varepsilon(0) - \varepsilon(\infty))}{\nu_0^2 - \nu^2 - i\gamma\nu} \qquad (7.17)$$

Born and Huang (1954) took γ as frequency independent, but for most alkali halides γ varies considerably in the LO frequency region and the expression must be modified to account for the discrepency.

The above discussions of lattice vibrations have so far been restricted to the harmonic approximation. This model fails to account for detailed structure in the measured spectra because it neglects the details of the interactions between the normal modes which accompany the decay of the transverse optic phonon. Studies of the effect of anharmonicity on various physical properties of crystals have been carried out by many authors [Cowley 1963, Wallis et al 1966, etc]. Let us consider an expression for the potential energy V which is expanded in a power series in terms of the displacements, i.e.

$$V = \xi_0 + \xi_1 u + \xi_2 u^2 + \xi_3 u^3 + \xi_4 u^4 + \ldots . \qquad (7.18)$$

If the u^3 and all higher order terms in the expansion are neglected, we have the "harmonic approximation", which has been discussed earlier. However, if we include the higher order terms in the power series, i.e. u^3, u^4 etc, this will lead to an anharmonic description

of the crystal.

A detailed discussion of the theory of the dielectric response of an anharmonic crystal has been given by Cowley [1963]. Therefore, only the results are quoted here. His expression for the complex frequency dependent susceptibility $\chi(\nu)$, which he derived by using diagrammatic perturbation theory for crystals with cubic symmetry is written as

$$\chi(\nu) = \frac{1}{Nvh} \frac{2\nu(oj)\, M_{\alpha}^{2}(oj)}{\nu^{2}(oj) - \nu^{2} + 2\nu(oj)[\Delta(oj,\nu) - i\Gamma(oj,\nu)]} \qquad (7.18)$$

where $\nu(oj)$ is the harmonic frequency of the TO phonon at wave vector $q \simeq 0$, $M_{\alpha}(oj)$ is the leading term in the expansion of the crystal dipole moment operator in a power series of the normal mode coordinates, Nv is the crystal volume, and $\Delta(oj,\nu)$ and $\Gamma(oj,\nu)$ are the real and imaginary parts of the irreducible self-energy of the transverse optic phonon.

The real part, $\Delta(oj,\nu)$ of the self-energy can be written as the sum of two parts, i.e.

$$\Delta(oj,\nu) = \Delta^{E} + \Delta^{A}(oj,\nu) \qquad (7.20)$$

where Δ^{E} is a frequency independent contribution which arises from the thermal expansion of the crystal, and $\Delta^{A}(oj,\nu)$ is frequency dependent, and arises purely from the anharmonic interactions.

Since the complex refractive index can be expressed as

$$n(\nu)^{2} = \varepsilon(\nu) = \varepsilon(\infty) + \chi(\nu) \qquad (7.21)$$

then for zero frequency, $\varepsilon(o)$ is defined as

$$\varepsilon(o) = \varepsilon(\infty) + \chi(o) \qquad (7.22)$$

And from equation 7.19, this will become

$$\varepsilon(o) = \varepsilon(\infty) + \frac{1}{Nvh} \frac{2\nu(oj)\, M_\alpha^2(oj)}{\nu^2(oj) + [\Delta^E - \Delta^A(oj,0)]} \qquad (7.23)$$

Thus from above the expression it will give the expression for $M_\alpha^2(oj)$ as

$$M_\alpha^2(oj) = \frac{1}{2} Nvh\, \nu(oj)[\varepsilon(o) - \varepsilon(\infty)] \qquad (7.24)$$

By substituting M_α^2 into equation 7.21, we will have

$$\varepsilon(\nu) = \varepsilon(\infty) + \frac{(\varepsilon(o) - \varepsilon(\infty))\,\nu^2(oj)}{\nu^2(oj) - \nu^2 + 2\nu(oj)[\Delta(oj,\nu) + i\Gamma(oj,\nu)]} \qquad (7.25)$$

for the dielectric response.

From equations $\Delta^A(oj, \nu)$ and $\Gamma(oj, \nu)$, it follows that the real and imaginary parts of the anharmonic self-energy of the transverse optic mode can be written as

$$\Delta^A(oj,\nu) = \frac{1}{2}[\nu(oj)[(\varepsilon(o) - \varepsilon(\infty))\eta'(\nu) - 1] + [\nu^2/\nu(oj)] - \Delta^E(oj),$$

$$\Gamma(oj,\nu) = -\frac{1}{2}\nu(oj)[\varepsilon(o) - \varepsilon(\infty)]\eta''(\nu) \qquad (7.26)$$

where

$$\eta'(\nu) = [\varepsilon'(\nu) - \varepsilon(\infty)] / \{[\varepsilon'(\nu) - \varepsilon(\infty)]^2 + \varepsilon''(\nu)^2\}$$

$$\eta''(\nu) = -\varepsilon''(\nu) / \{[\varepsilon'(\nu) - \varepsilon(\infty)]^2 + \varepsilon''(\nu)^2\}$$

where $\varepsilon'(\nu)$ and $\varepsilon''(\nu)$ are the measured real and imaginary parts of the dielectric function derived from the refractive index measurements. Thus the full frequency dependence of $\Delta^A(\nu)$ and $\Gamma(\nu)$ can be calculated from the measured complex delectric response for

comparison with theoretical calculations.

b) Experimental results

Alkali halides are a good subject for spectroscopic studies in the far infrared because of their distinctive reststrahlen region. All the measurements made using the two interferometers described in Chapter 5 were on KCl and KBr crystals, which have their reststrahlen bands comfortably within the working range of the instruments.

In the region of the reststrahlen band, the crystal is nearly opaque, hence the reflection instrument is used. However, when the sample becomes more transparent away from the reststrahlen band, its phase reflection coefficient, $\phi_r(\nu)$, is very close to that of the reference mirror (π radians) and cannot be satisfactorily determined. Hence, a simultaneous measurement made by the transmission instrument has been used to give a better result, due to the phase transmission coefficient $\phi_t(\nu)$ being very much larger than ($\phi_r - \pi$).

For the reflection measurement, crystals having the dimensions of 50 mm diameter and 6 mm in thickness were used. One surface was optically polished to a flatness of about $\pm$ 0.1μm, and partially aluminised in a pattern described in Chapter 5. By using the switching mode of the instrument, systematic phase errors resulting from the drift of the reference mirror were avoided.

For the transmission measurements, a KCl crystal 25mm in diameter was used, and thinned to 254 $\pm$ 2μm, but the thickness of the KBr crystal was only 110 $\pm$ 2μm. Therefore, the insertion loss produced by these specimens will be in the category of thin specimens, and the details of the procedure for determining the amplitude and phase

transmission coefficients, and the subsequent calculation of the optical constants and dielectric functions have been given in Chapter 3.

The complex refractive indices of KCl and KBr, measured using the reflection and transmission instruments are shown in fig. 7.9 to 7.10 for temperatures in the range 7 k to 300 k. The corresponding dielectric functions are illustrated in fig 7.11 to 7.12. The frequencies of the transverse optic (TO) and longitudinal optic (LO) modes determined from the plots of dielectric response are also indicated in the figures, and these frequencies are in excellent agreement with values determined by Lowndes [1970] and Lowndes and Martin [1969].

The self-energy functions, $\Delta(oj, \nu)$ and $\Gamma(oj, \nu)$ have been calculated from the above dielectric function data, using equation 7.26. The values of Δ^{E}, $\varepsilon(o)$, $\varepsilon(\infty)$ have been taken from Lowndes et al [1969 & 1976]. In the figure showing the experimental results of for KBr at room temperature, the solid line is a calculation which includes the sum of the lowest order cubic and quartic terms [Bruce 1973].

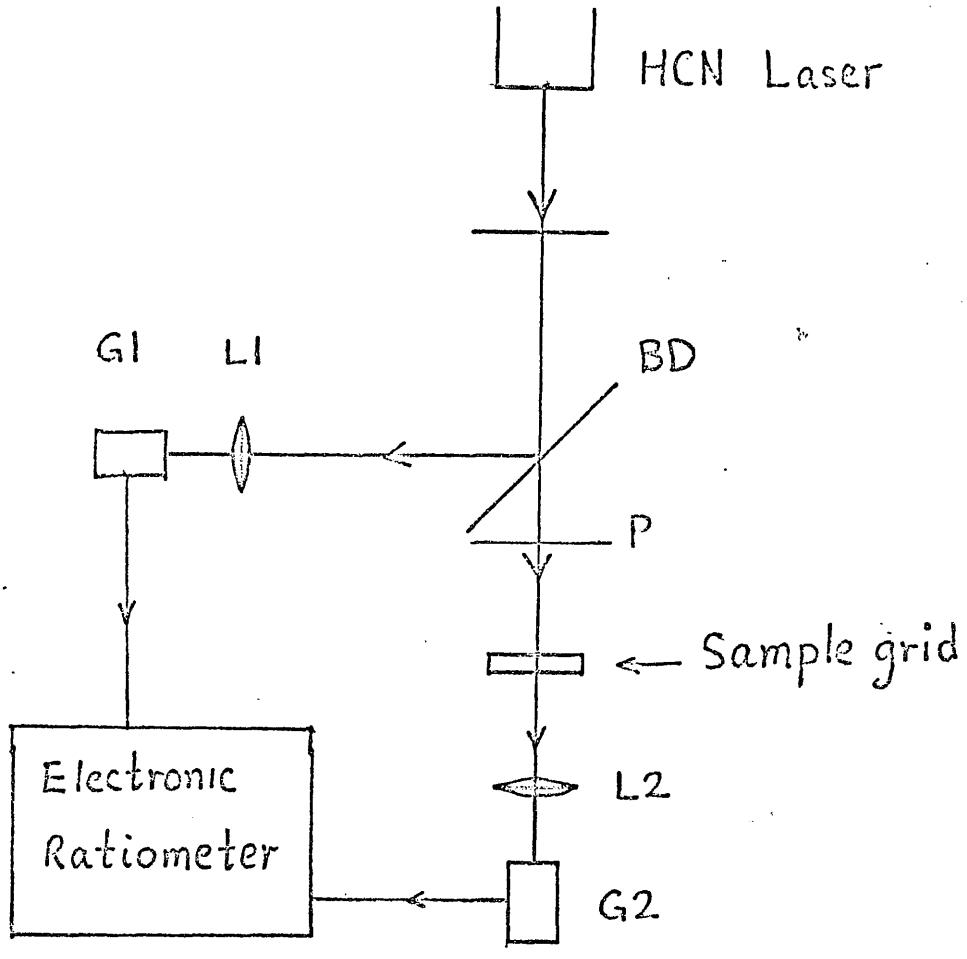

Fig. 7.1 Schematic diagram of the equipment for the laser measurement.

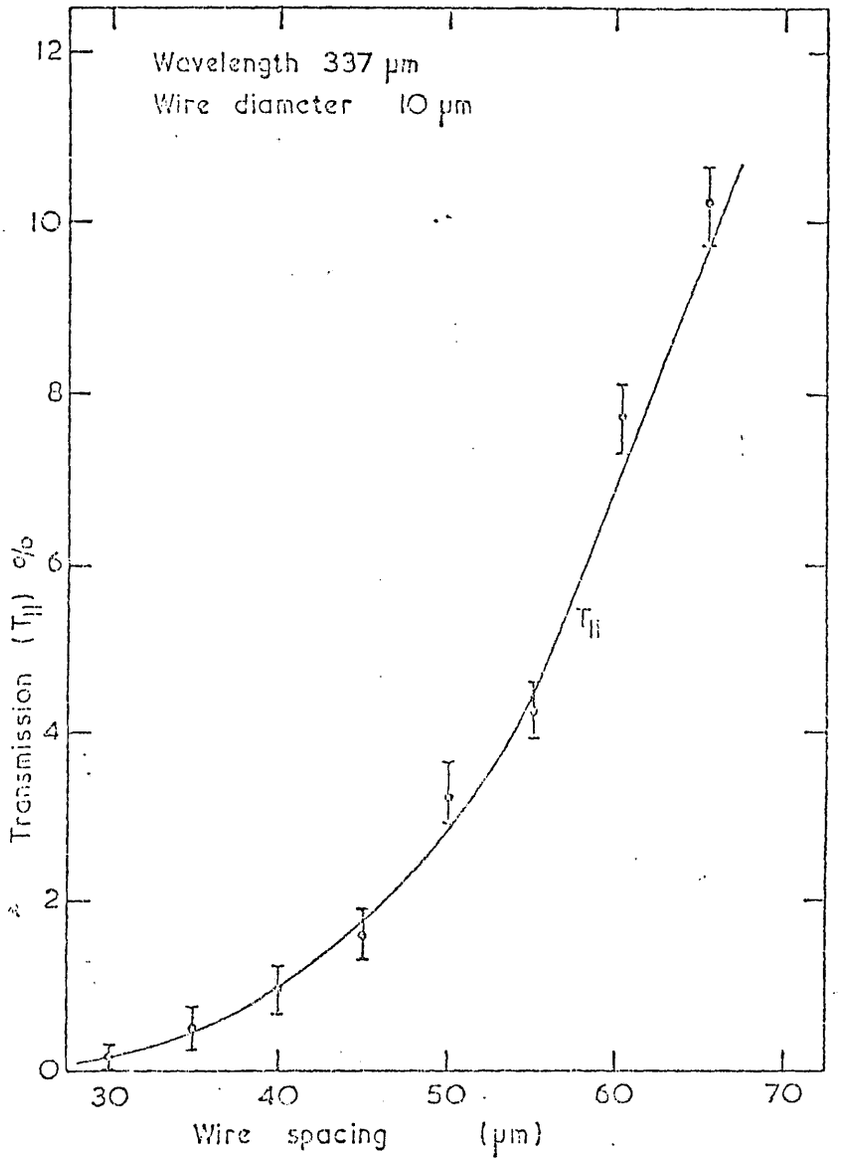

Fig. 7.2 The results from the laser experiment.

..... Measured

_____ Calculated

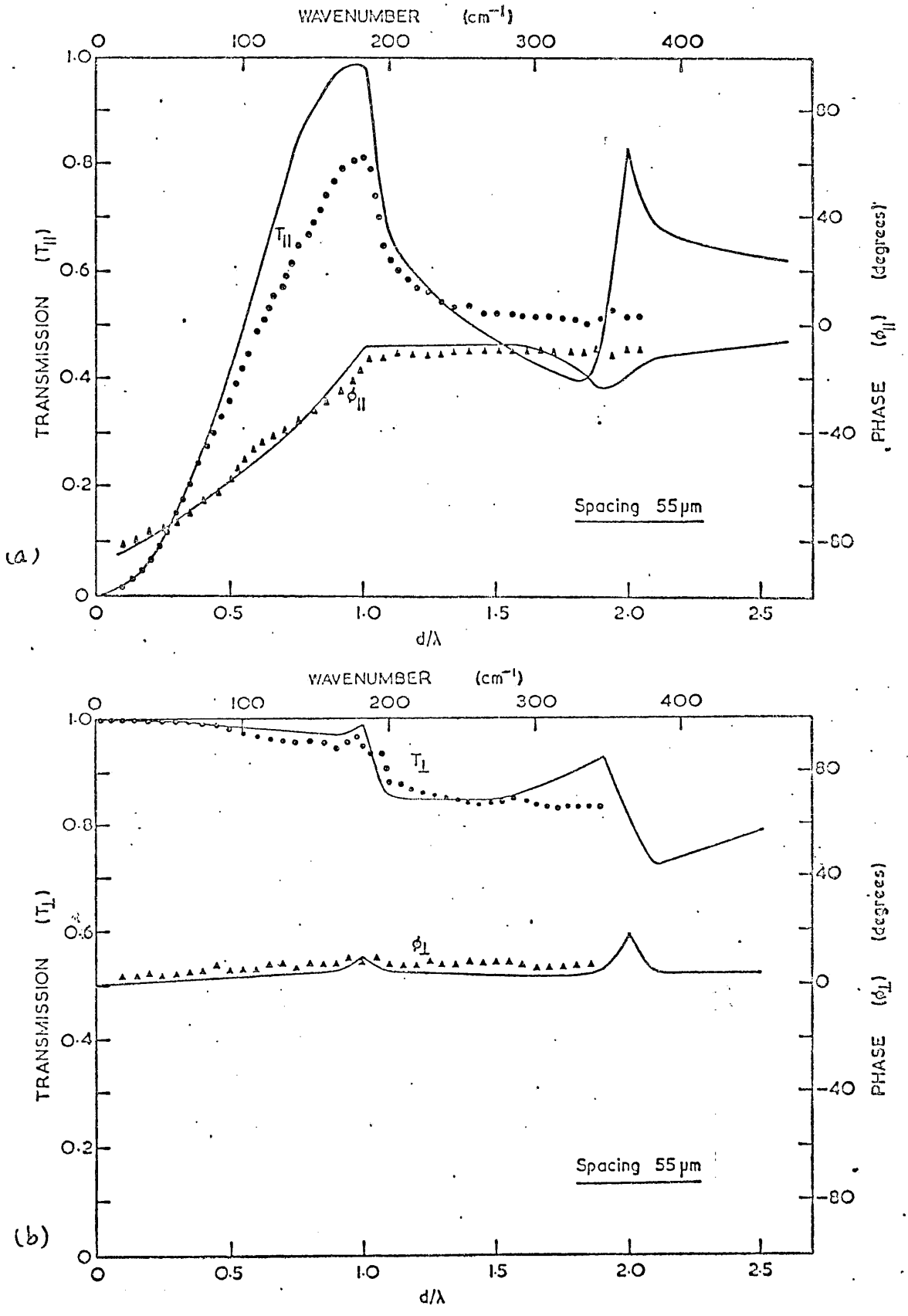

Fig. 7.3 Measured and calculated power transmission and phase spectra for a grid of 55 μm spacing for (a) $\underset{\sim}{E} \parallel \underset{\sim}{S}$ and (b) $\underset{\sim}{E} \perp \underset{\sim}{S}$.

..... Measured

_____ Calculated

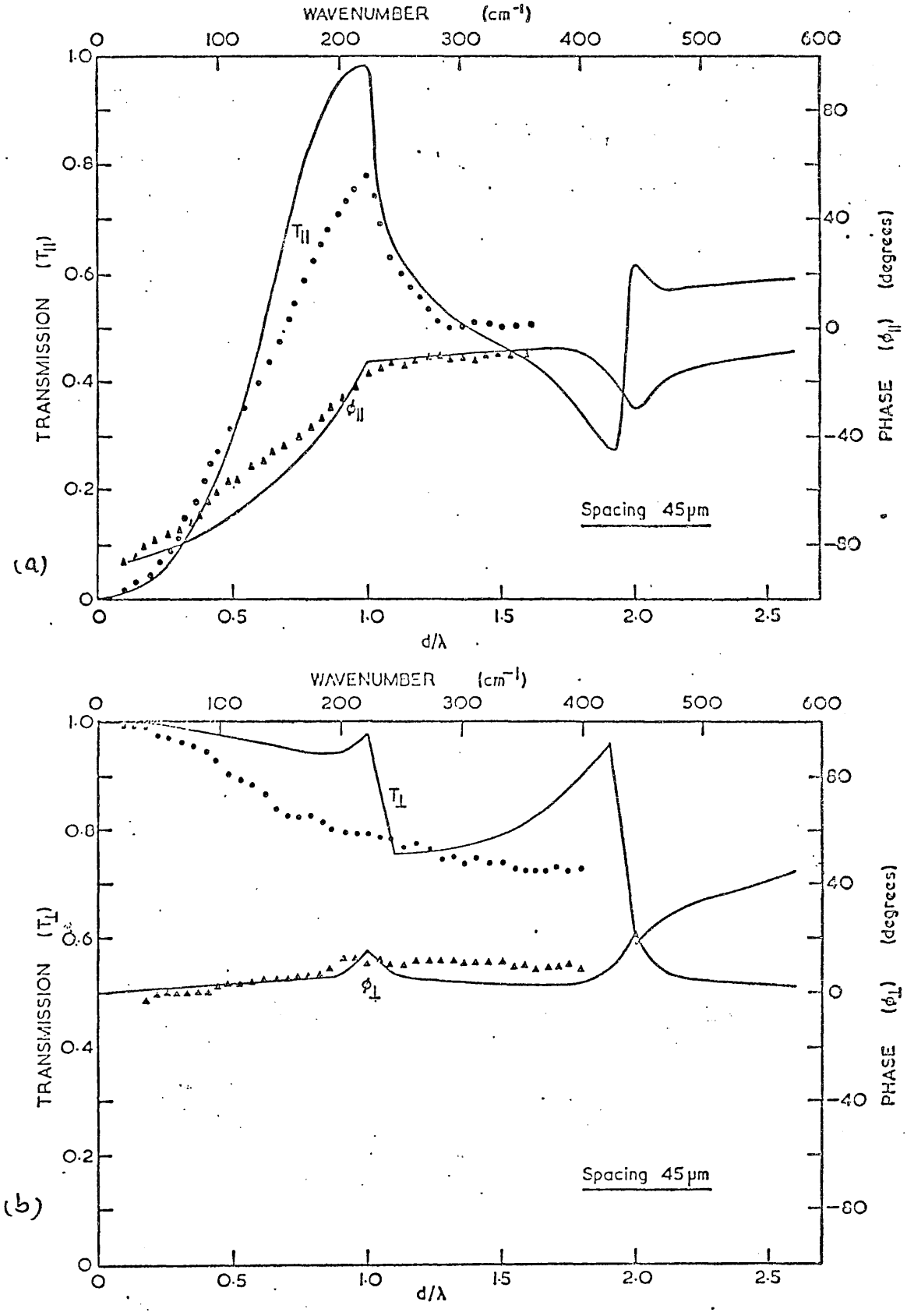

Fig. 7.4 Measured and calculated power transmission and phase spectra for a grid of 45 μm spacing for (a) $\underset{\sim}{E} \parallel \underset{\sim}{S}$ and (b) $\underset{\sim}{E} \perp \underset{\sim}{S}$.

..... Measured

_____ Calculated

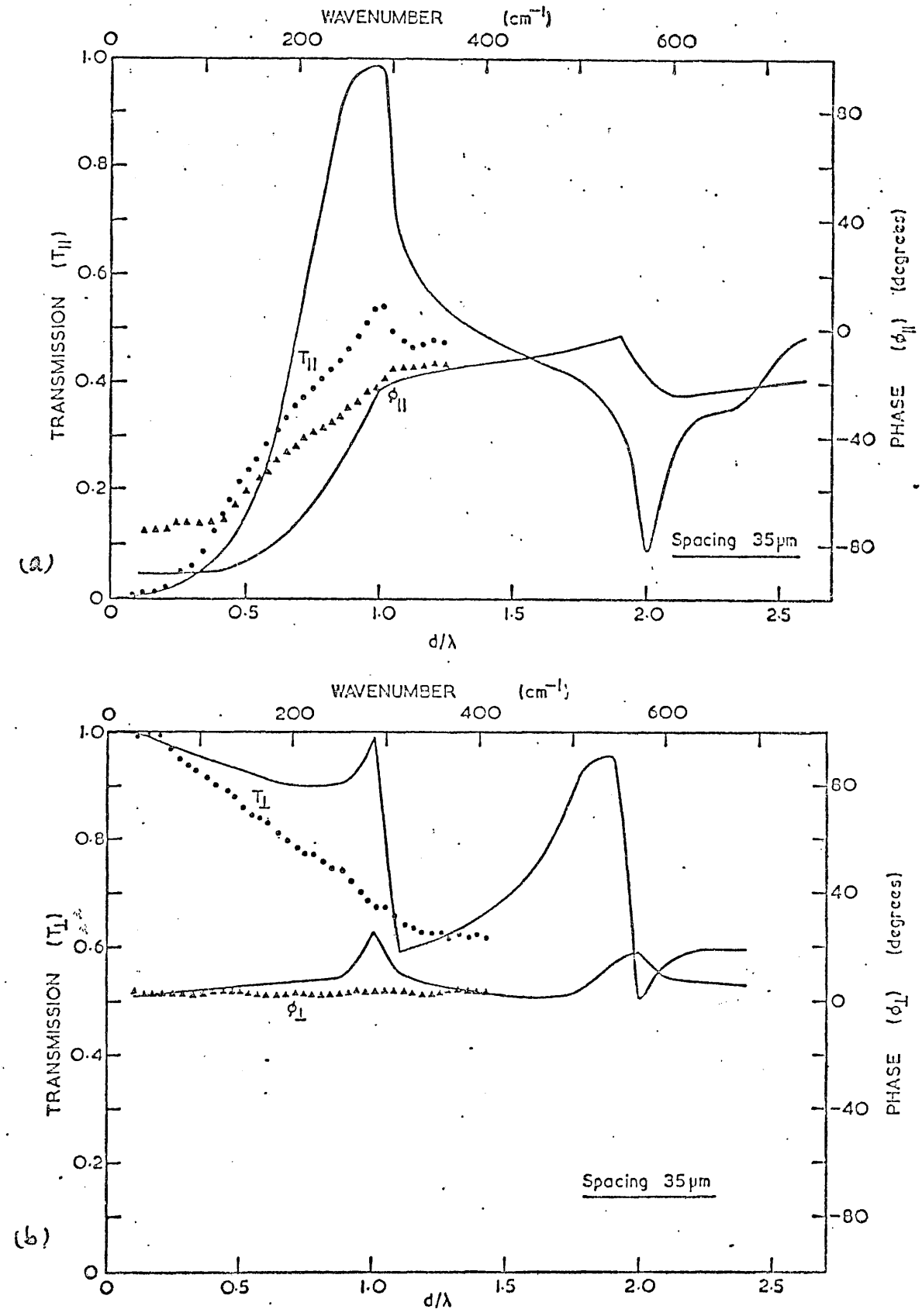

Fig. 7.5 Measured and calculated power transmission and phase spectra for a grid of 35 μm spacing for (a) $\underset{\sim}{E} \parallel \underset{\sim}{S}$ and (b) $\underset{\sim}{E} \perp \underset{\sim}{S}$.

..... Measured

_____ Calculated

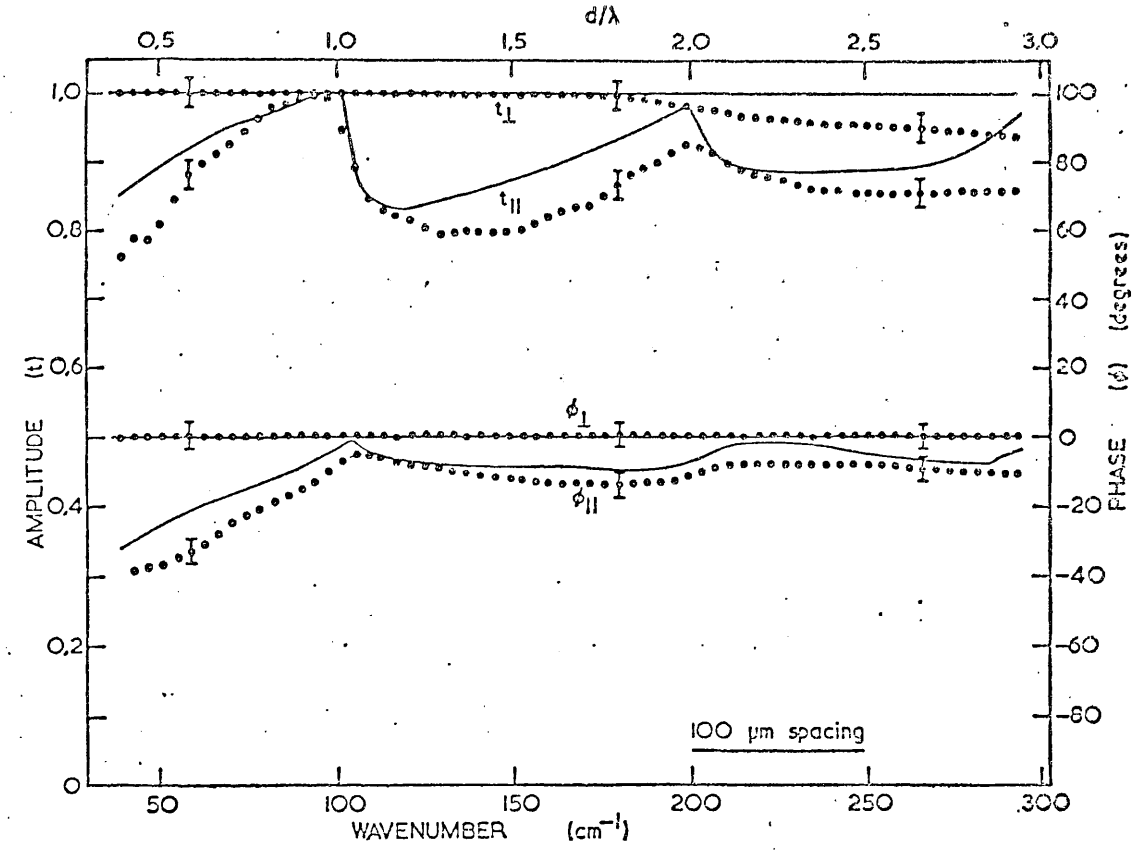

Fig. 7.6 Measured and calculated power transmission and phase spectra for a grid of 100 μm spacing

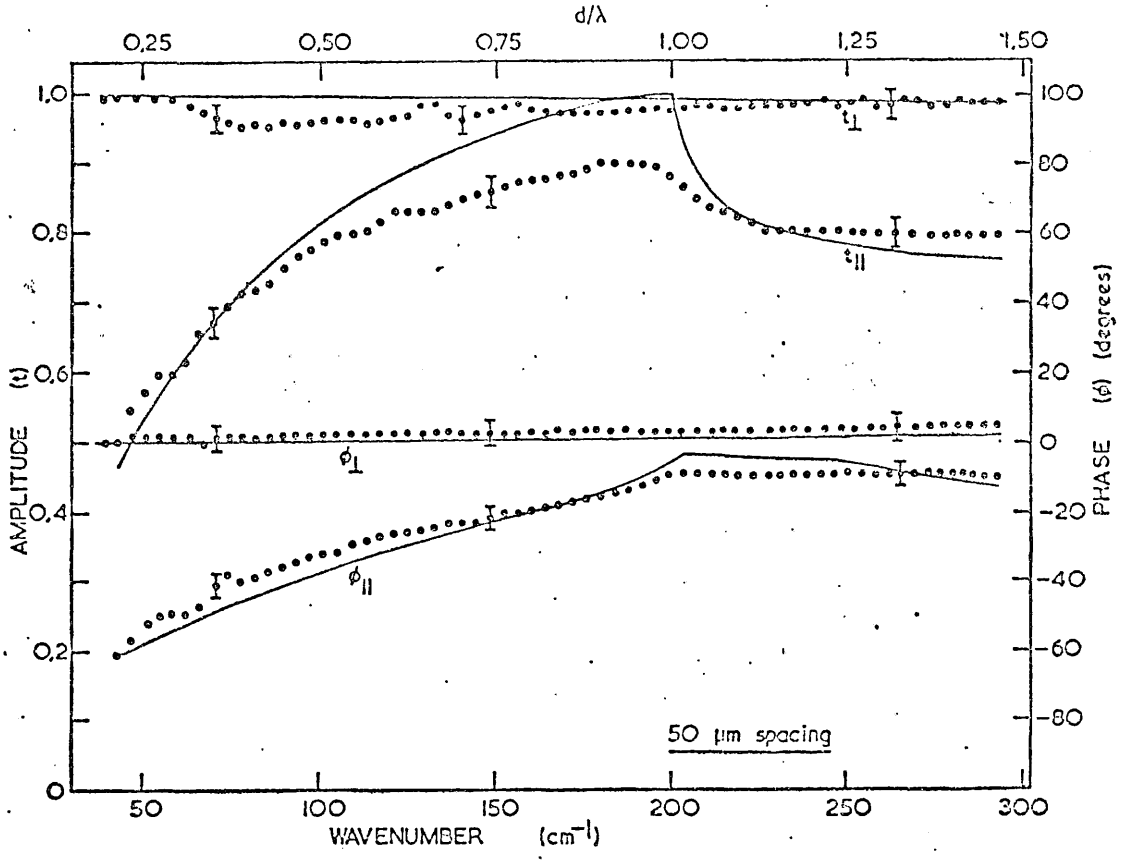

Fig. 7.7 Measured and calculated power transmission and phase spectra for a grid of 50 μm spacing

····· Measured

_____ Calculated

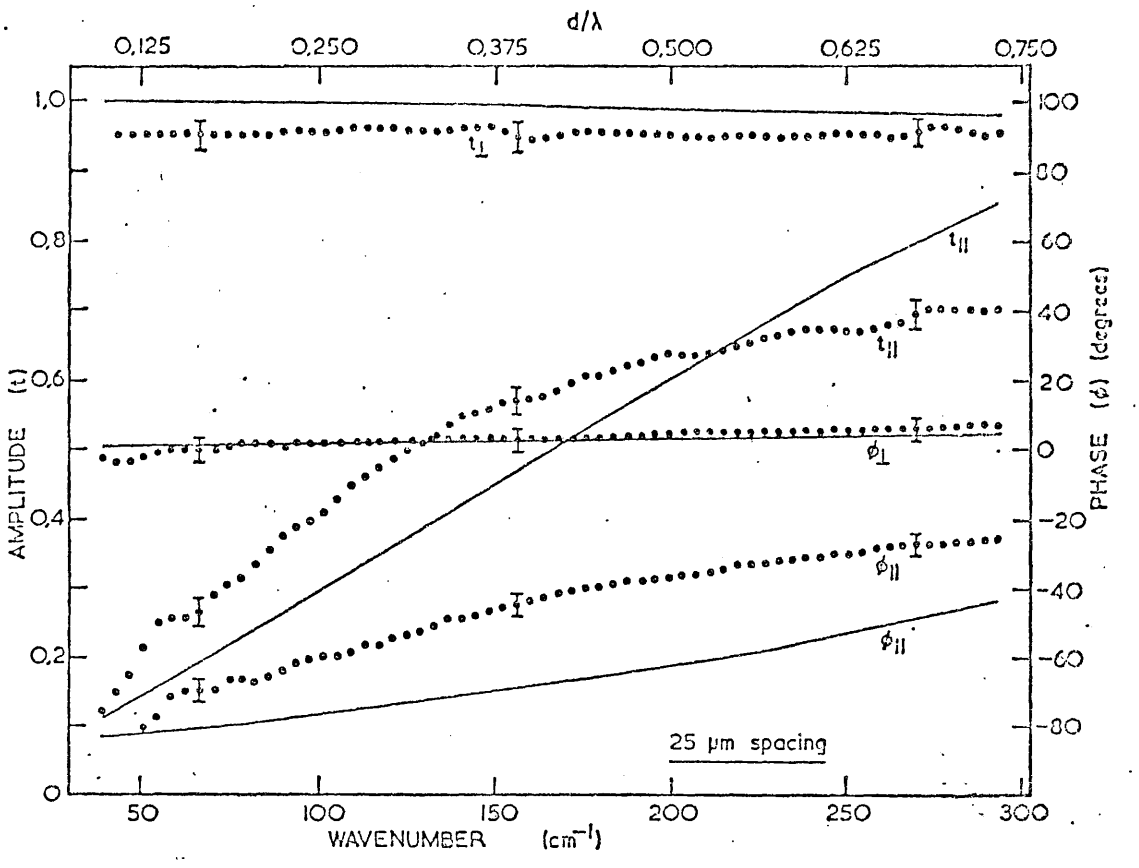

Fig. 7.8 Measured and calculated power transmission and phase spectra for a grid of 25 μm spacing

..... Measured

_____ Calculated

TABLE 1

	Nominal spacing (μm)		
	55	45	35
$\bar{x}$	55.9	47.5	36.0
σ	8.9	9.7	10.1
$\sigma/\bar{x}$	.16	.20	.28

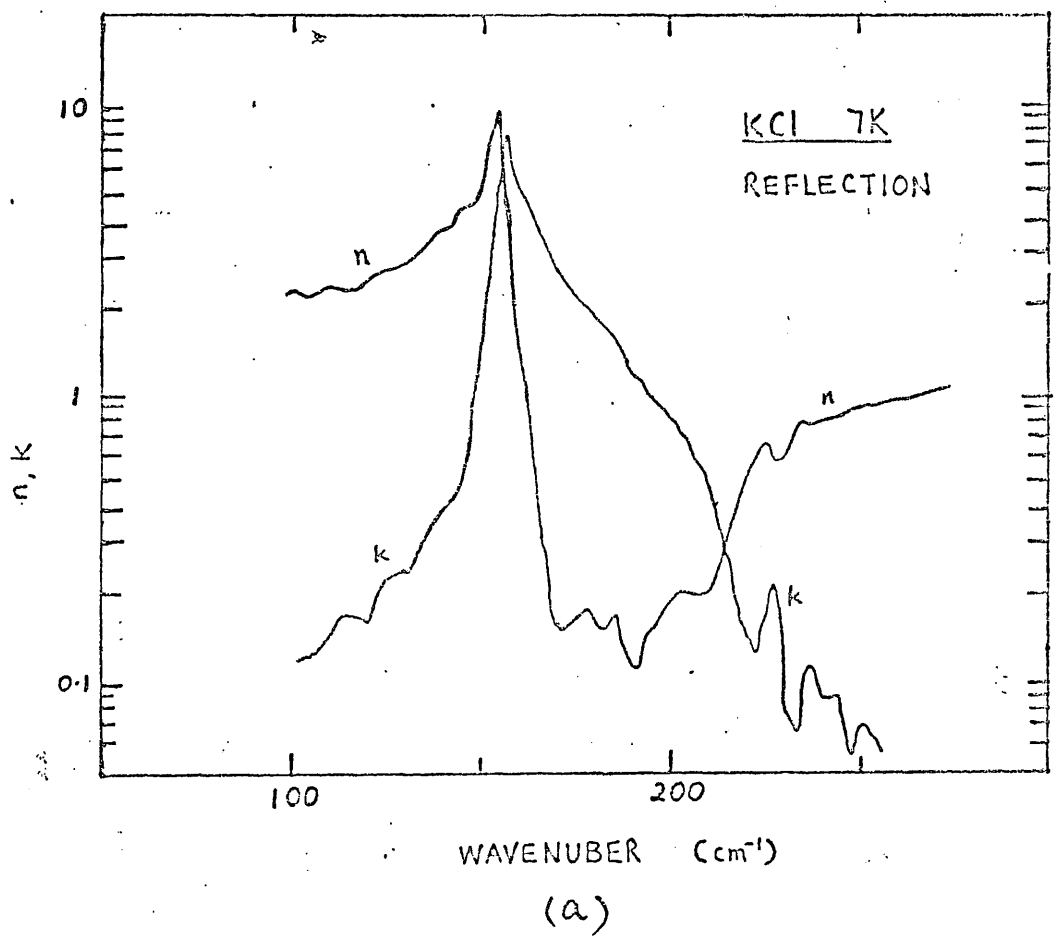

Fig. 7.9 Measured optical constants for KCl crystal at temperatures of 7K (a), 100K (b) and 300K (c).

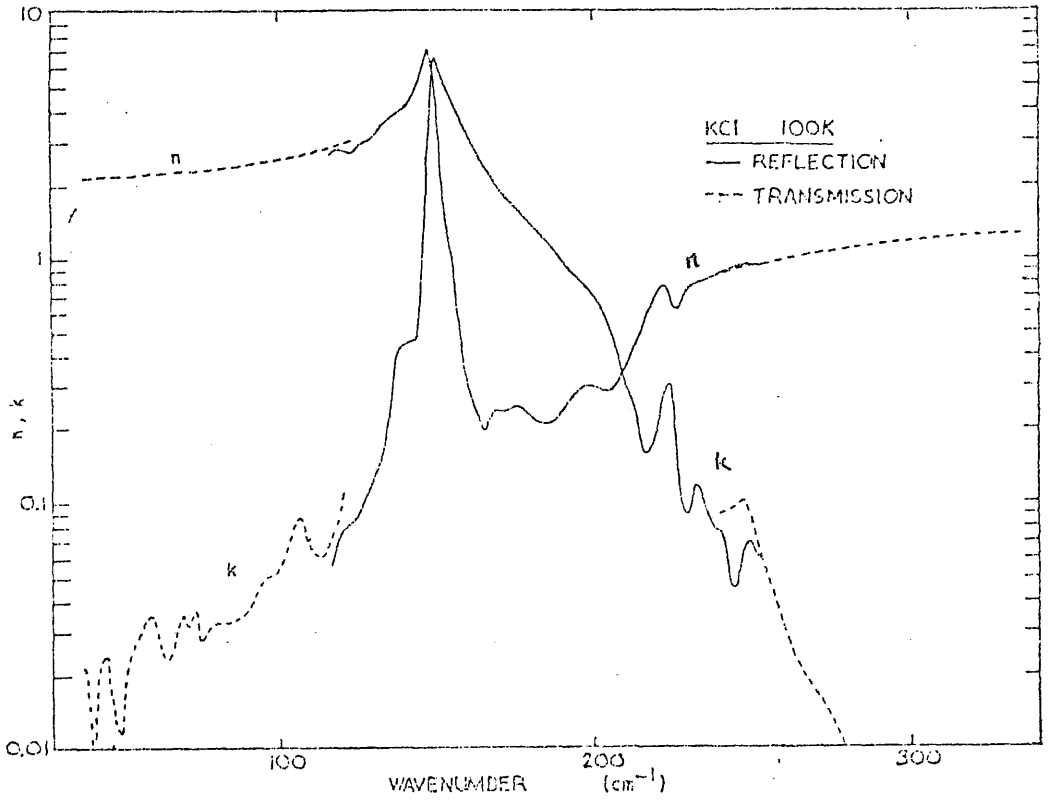

Fig. 7·9 (b)

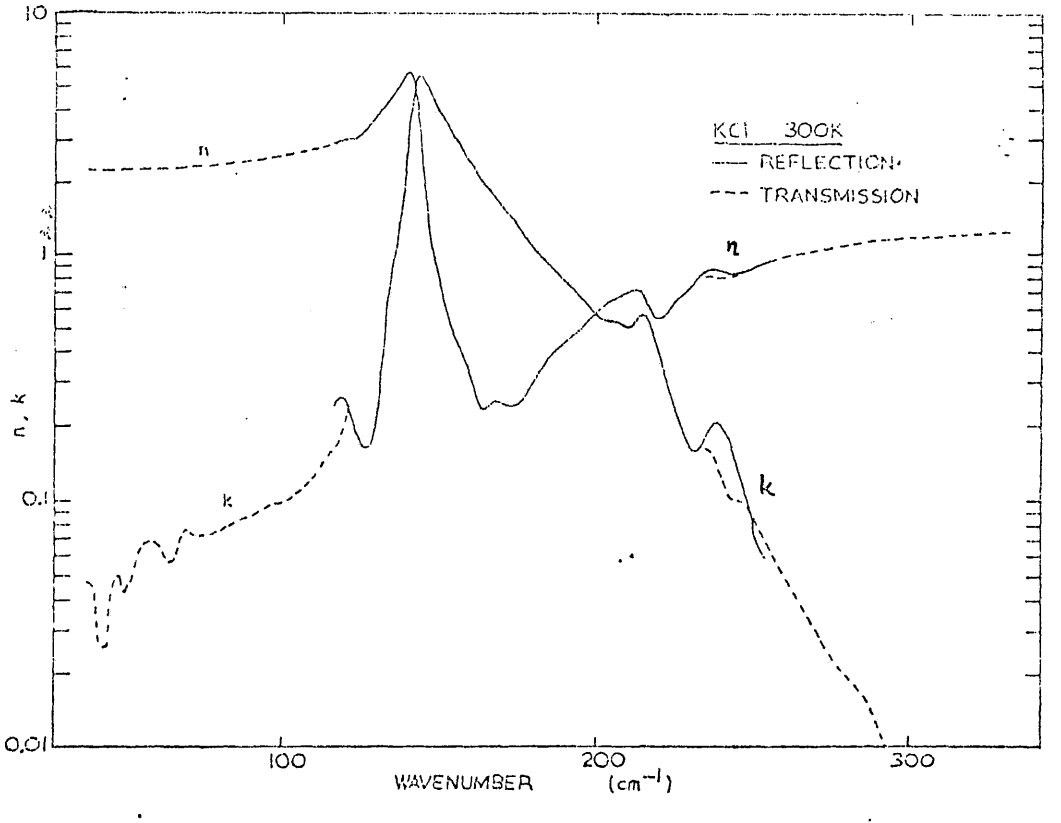

Fig. 7·9 (c)

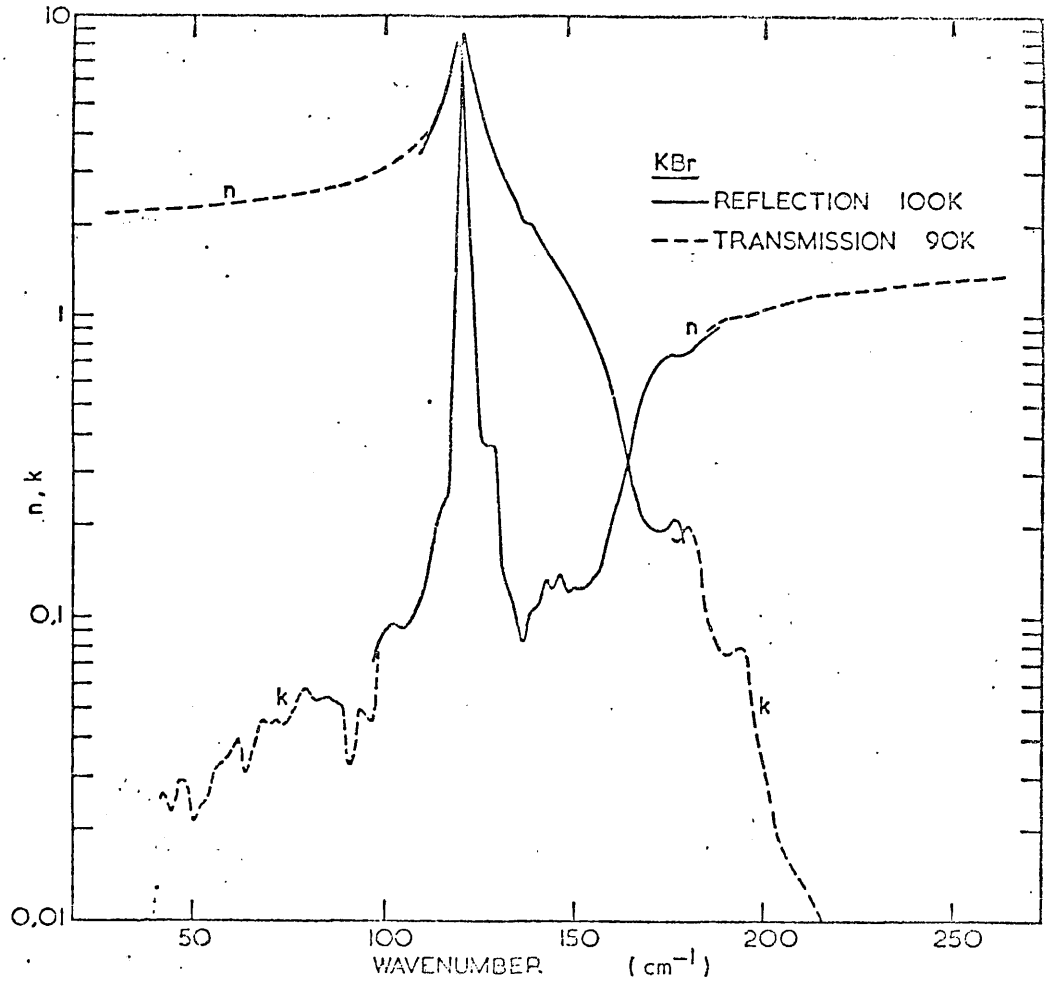

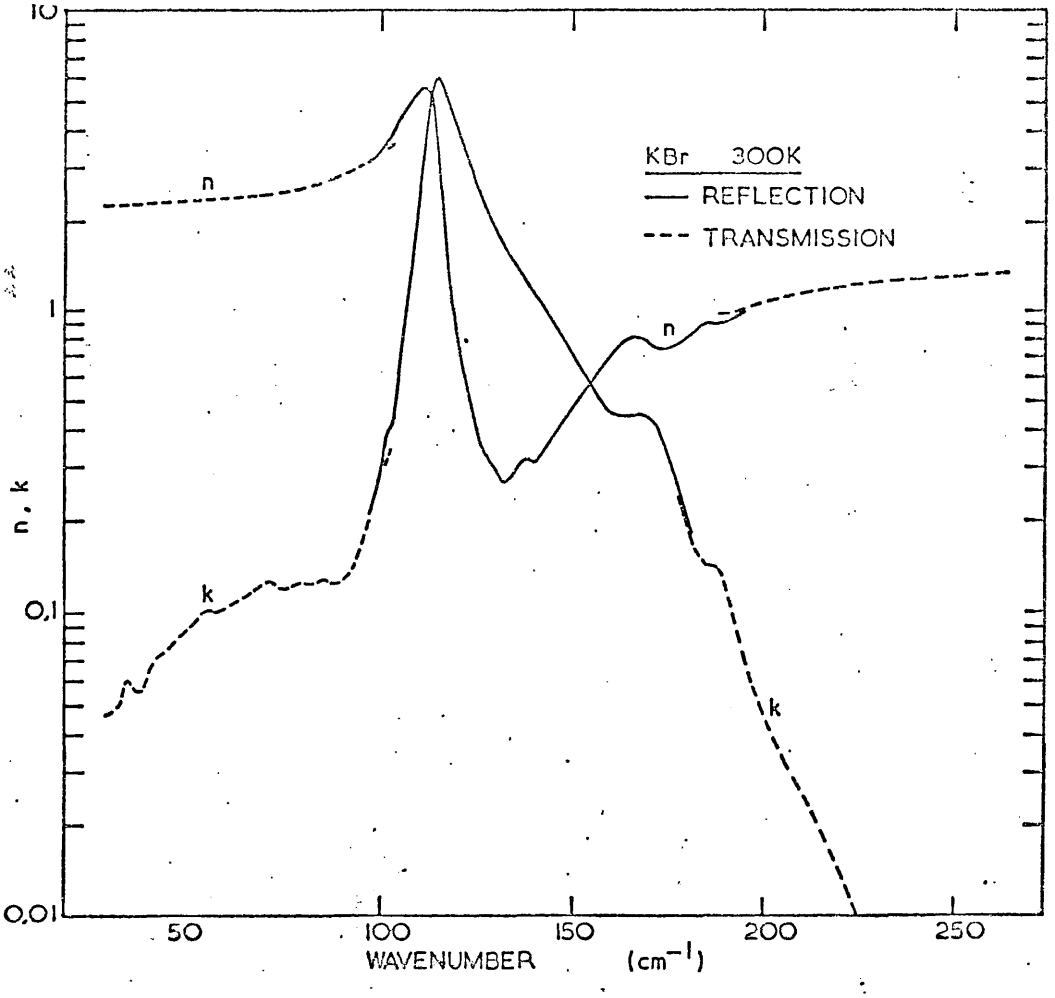

Fig. 7.10 Measured optical constants for KBr crystal at temperatures of 100K (a) and 300K (b).

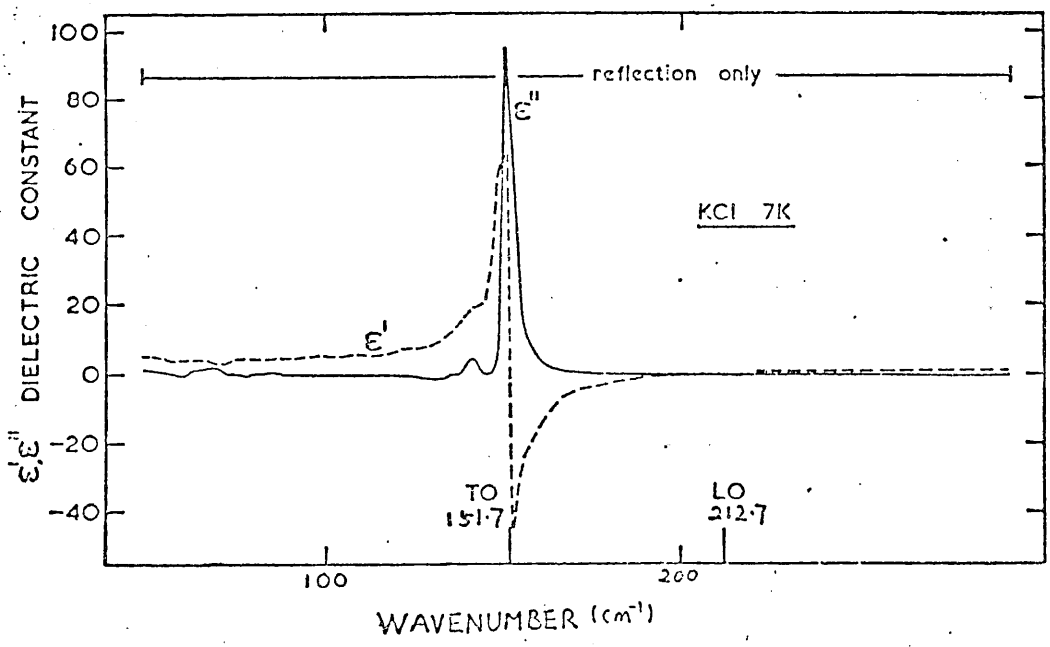

Fig. 7·11 (a)

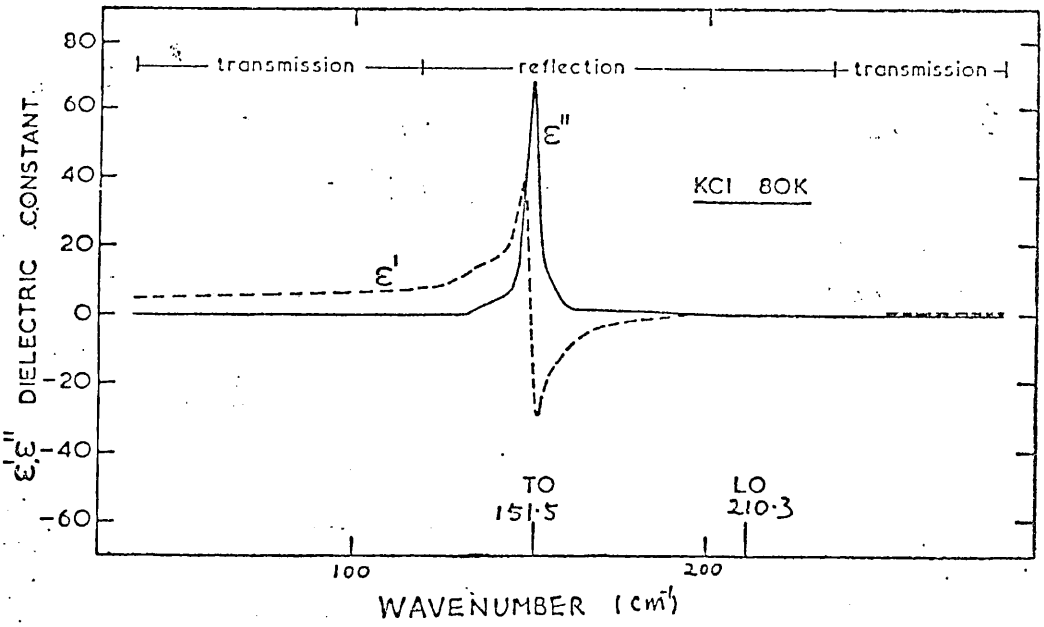

Fig. 7·11 (b)

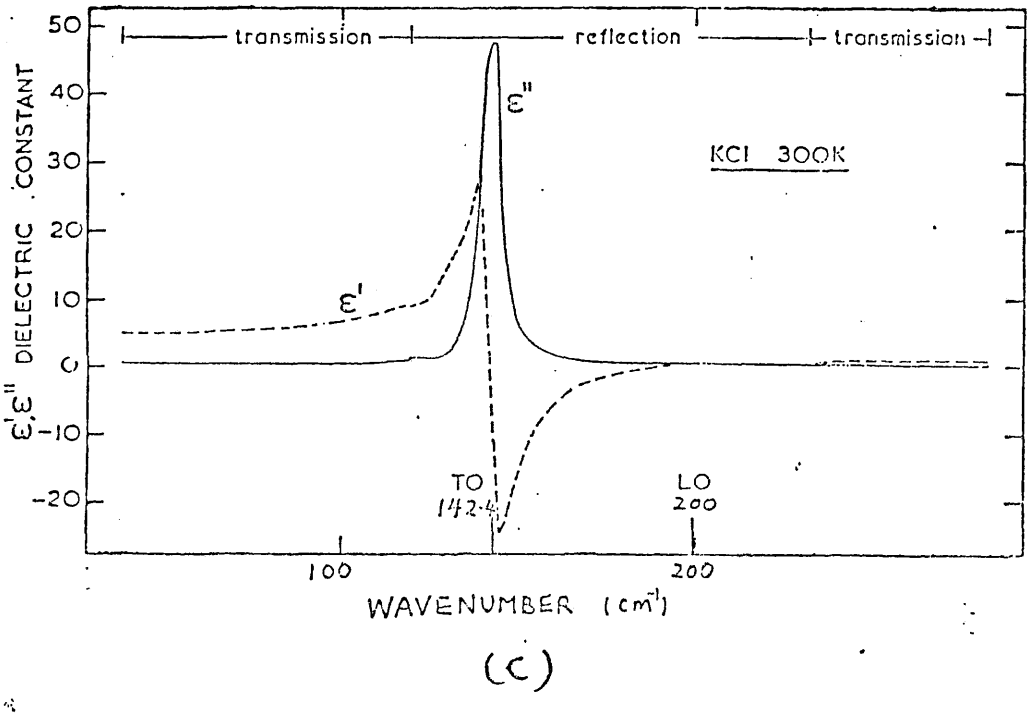

Fig. 7.11 Measured dielectric constants for KCl crystal at temperatures of 7K (a), 100K (b) and 300K (c).

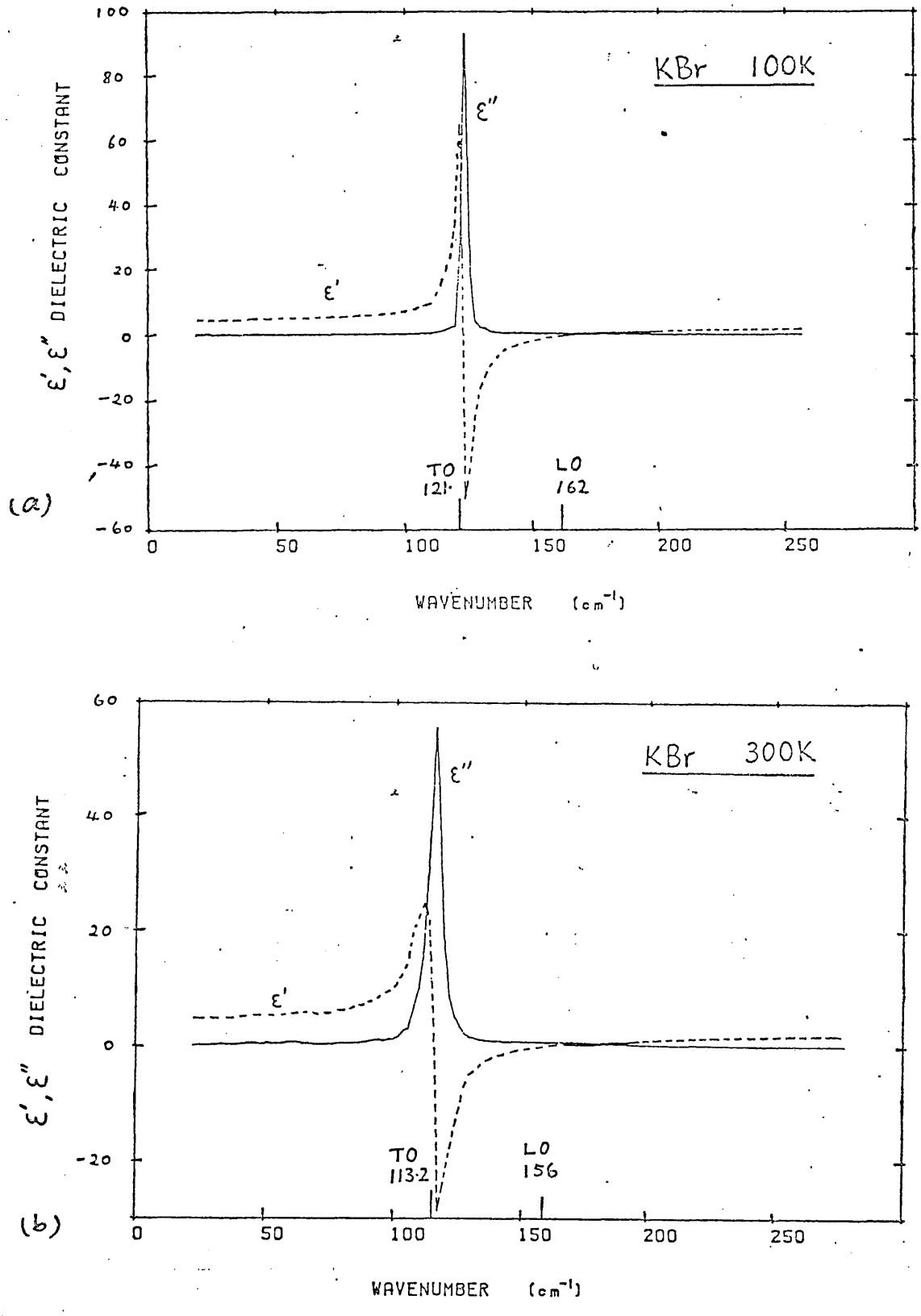

Fig. 7.12 Measured dielectric constants for KBr crystal at temperatures of 100K (a) and 300K (b).

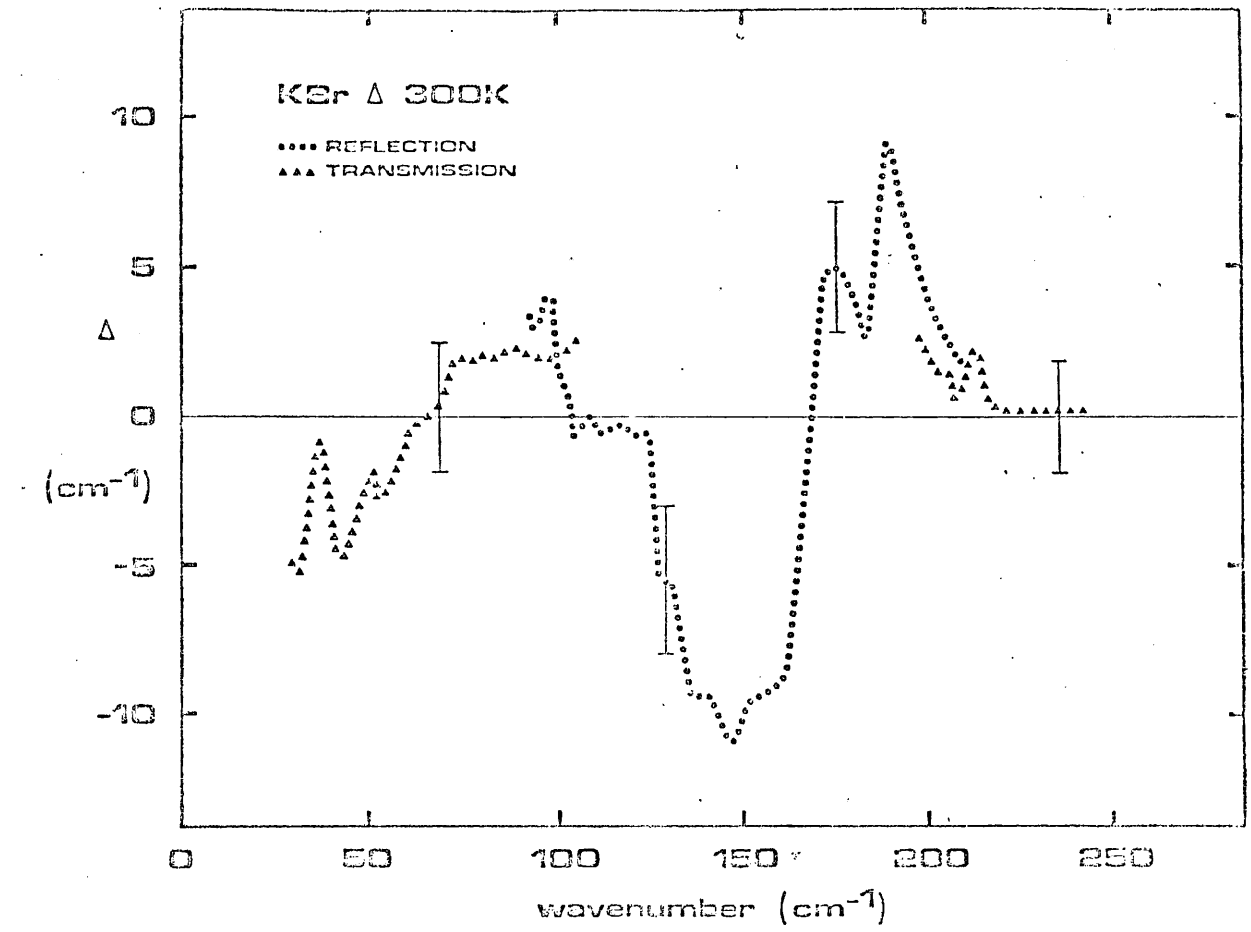

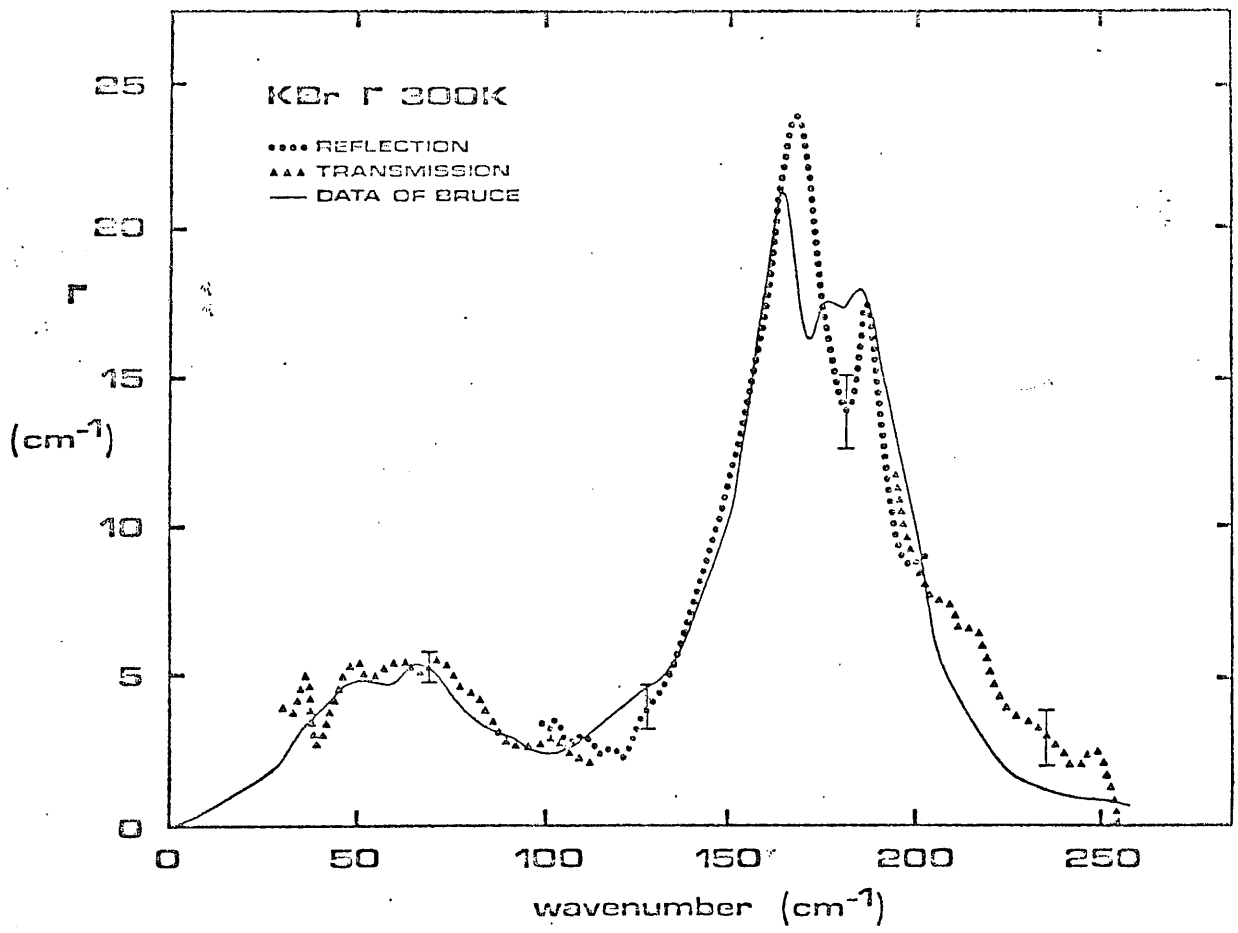

Fig. 7.13 Measured self-energy functions for KBr at 300K.

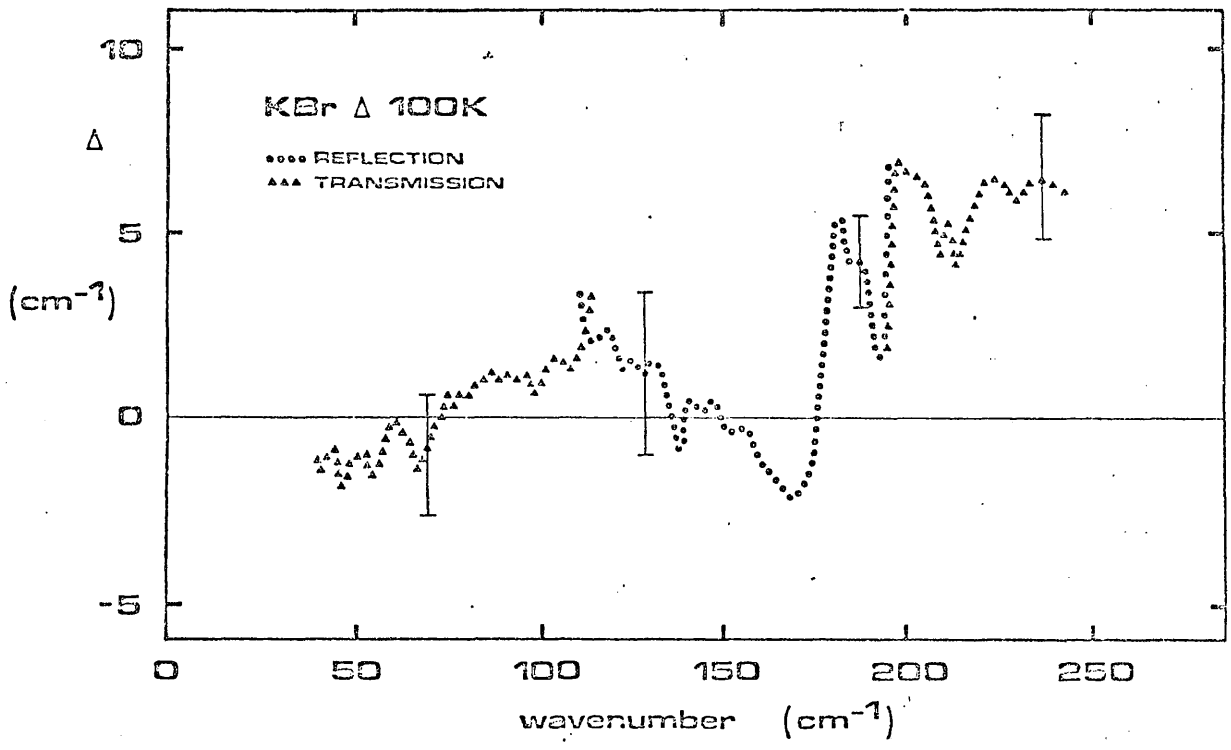

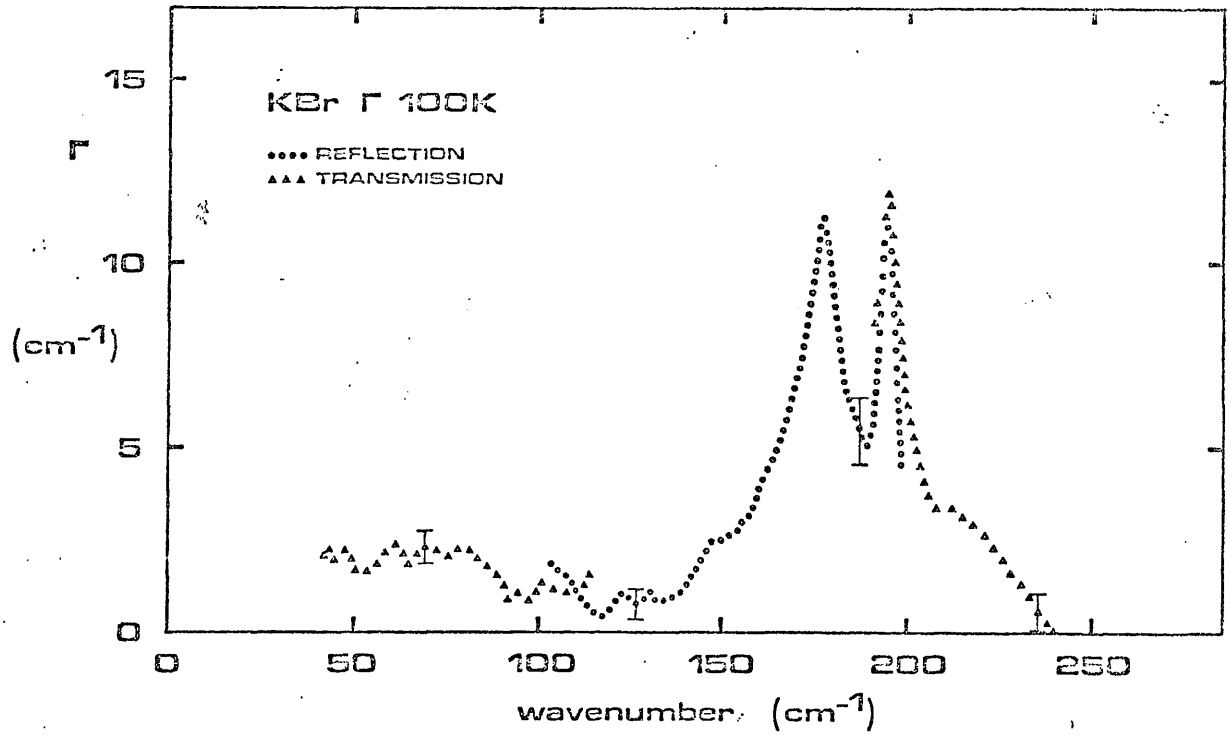

Fig. 7.14 Measured self-energy functions for KBr at 100K.

CHAPTER 8

CONCLUDING REMARKS

Dispersive Fourier transform spectrometry provides a simple direct method for the determination of the optical constants of materials in the far infrared region. This technique has formed the basis of the measurements presented in this thesis.

The performance of free-standing wire grids wound from 10 and 5 μm diameter tungsten wire has been investigated experimentally and compared with calculations based on the "least-squares" method developed by Beunen [1976].

In the case of 10 μm diameter wire grids the calculations are compared with measurements made at λ = 337 um (ν =29.7 cm^{-1}) using an HCN laser, and with broad band measurements made by dispersive Fourier transform spectrometry. At frequencies above 100 cm^{-1}, reasonable agreement is only obtained between experiment and theory away from the first diffraction peak (d/λ =1), although this peak is reproduced quite well with each grid for $\underset{\sim}{E} \parallel \underset{\sim}{S}$. The quantitative differences between measurement and theory are believed to be due to the effect of irregularities in the wire spacings. Thus, a number of wire grid spacings for each grid were measured, and the irregularities in the grid spacing found to correlate quite well with the observed discrepancies. The second diffraction peak in the d/λ =2 region was only measured for the grid with a spacing of 55 μm, because the peak frequencies for the other two grids were outside the measuring range of the interferometer. However, the predicted peak did not show up in the measurement, and this is also believed to be due to

the irregularities in the wire spacings. At frequencies below 100 cm^{-1} excellent agreement is obtained between theory and measurements. This is not surprising because small irregularities in the wire spacing are not expected to have a significant effect on the measured spectra when $\lambda \gg d$.

In the case of 5 um wire grids similar results were obtained, and the second diffraction peak appeared nicely for the grid with 100 um spacing. Again the discrepancies are believed to be due to the effect of irregularities in the wire spacings.

Free-standing grids wound from 5 μm diameter tungsten wire with 12.5 μm spacing have been used as beam dividers in a Fourier spectrometer. It has been shown [Ade et al 1979, Mok et al 1979] that the spectrometer can be operated at frequencies up to 700 cm^{-1}. It has also been shown that the performance of instruments in the low frequency region can be improved by polarising interferometry, using a free standing wire grid as the beam divider. If a liquid helium cooled detector is also used, the instruments can then be operated down to a frequency of about 3 cm^{-1}. Due to lack of time the above improvements have not been fully exploited in the work described in this thesis.

By interfacing a microcomputing system with a Fourier spectrometer, the data acquisition system has been improved and on-line data analysis facilities have been provided. The micro is a slow and small device when compared with a large main frame computer. However, this microcomputer system can store up to 24 thousand sampling points before transfer onto a floppy disc, and it can perform Fourier transformation for 4 thousand points in about 4 minutes. This is not fast but proved to be adequate for most applications. With the introduction of newer micro chips, the performance of such a system

will greatly improve in the near future.

The optical constants of KCl and KBr crystals have been measured by reflection and transmission dispersive Fourier transform spectroscopy and presented in the temperature range 7-300K. However, at present the transmission instrument only permits measurements to be made at temperatures between 77 and 300K. The results have been used to calculate the dielectric functions for each crystal, and the frequencies of the transverse optic (TO) and longitudinal optic (LO) modes obtained are in good agreement with the values determined else where [Lowndes 1970, Lowndes et al 1969]. The self-energy functions for KBr have also been determined and at room temperature $\Gamma(\omega, \nu)$ is in good agreement with calculations by Bruce [1973].

REFERENCES

Abramowitz, M. and I. A. Stegun eds. (1965), "Handbook of Mathematical Functions", Dover Publications.

Ade, P. A. R., A. E. Costley, C. T. Cunningham, C. L. Mok, G. F. Neill and T. J. Parker (1979), Infrared Phys 19, 599.

Bell, E. E. (1965). Japan. J. Appl. Phys. (Suppl. I) 4, 412.

Bell, R. J.(1972). "Introductory Fourier Transform Spectroscopy". Academic Press, New York.

Beunen, J. A.(1976). M. Sc. Thesis, University of Sydney.

Beunen, J. A., A. E. Costley, C. L. Mok, G. F. Neill, T. J. Parker and G. Tait.(1981). J. Opt. Soc. Am. 71, February Issue.

Birch, J. R. and T. J. Parker(1979). Chapter 3 in Vol. II of "Infrared and Millimetre Waves", Ed. K. J. Button. Academic Press, New York.

Born, M. and K. Huang(1966). "Dynamical Theory of Crystal Lattices". Oxford University Press, London.

Born, M. and E. Wolf(1970). "Principles of Optics", Pergamon Press, Oxford.

Bruce, A. D.(1973) J. Phys. C6, 174.

Chamberlain, J. E. and H. A. Gebbie(1965). Nature 206, 602.

Chamberlain, J. E.(1971). Infrared Phys 11, 25.

Chamberlain, J. E.(1972). Infrared Phys 12, 145.

Chamberlain, J. E.(1979). "The Principles of Interferometric Spectroscopy". Wiley Publication, New York.

Chantry, G. W.(1971). "Submillimetre Spectroscopy". Academic Press, New York.

Cooley, J. W. and J. W. Tukey (1965). Math. Comput. 19, 297.

Costley, A. E., K. H. Hursey, G. F. Neill and J. M. Ward(1977). J. Opt. Soc. Am. 67, 979.

Conte, S. D.,and de Boor, C.(1972). "Elementary Numerical Analysis." P.32. McGraw-Hill, New York and Kogakusha, Tokyo.

Cowley, R. A.(1963). Adv. Phys. 12, 421.

CP/M Manual.(1979). Digital Research, California, USA.

Davies, J. B.(1973). IEEE Trans Microwave Theory MIT-21, 99.

Donovan, B. and J. F. Angress.(1971). "Lattice Vibrations". Chapman and Hall, London.

Fellgett, P.(1958). J. Phys. Radium 19, 187.

Girard, A. and P. Jacquinot.(1967). "Advanced Optical Technique". p.71, North Holland Publications.

Huang, K.(1951). Proc. Royal Soc A, 208, 352.

Jones, D. S.(1964). "The Theory of Electromagnetism", Pergamon Press, Oxford.

Lowndes, R. P. and D. H. Martin.(1969). Proc. Roy. Soc. A308, 473.

Lowndes, R. P. and A. Rastogi.(1976). Phys. Rev. B14, 3598.

Martin, D. H. and E. Puplett.(1970). Infrared Phys. 10, 105.

Mok, C. L., W. G. Chambers, T. J. Parker and A. E. Costley.(1979). Infrared Phys. 19, 437.

Mok, C. L., T. J. Parker and W. G. Chambers.(1980). Solid State Comm. 34, 567.

Parker, T. J., W. G. Chambers, J. E. Ford and C. L. Mok.(1978). Infrared Phys. 18, 571.

Parker, T. J., R. P. Lowndes and C. L. Mok. (1978). Infrared Phys. 18, 565.

Parker, T. J., C. L. Mok and W. G. Chambers.(1979). IEEE Conference Pub. No. 177, 207.

Wallis, R. F., I. P. Ipatova and A. A. Maradudin.(1966). Sov. Phys. Solid St. 8, 850.

Z80 Assembly Language Programming Manual(1977), Zilog Inc.

Z80 Technical Manual(1977), Zilog Inc.

PUBLICATIONS BASED ON THE WORK DESCRIBED IN THIS THESIS

1. T J Parker, W G Chambers, J E Ford and C L Mok
A Fourier spectrometer for determining the optical constants of transparent solids in the far infrared from 77-300K.
Infrared Phys 18, 571 (1978)

2. T J Parker, R P Lowndes and C L Mok
A Fourier spectrometer for dispersive reflection measurements on highly absorbing solids in the far infrared at temperature down to 4.2K.
Infrared Phys 18, 565 (1978)

3. P A R Ade, A E Costley, C T Cunningham, C L Mok, G F Neill and T J Parker
Free-standing grids wound from 5 um diameter wire for spectroscopy at far infrared wavelengths.
Infrared Phys 19, 599 (1979)

4. C L Mok, W G Chambers, T J Parker and A E Costley
The far infrared performance and application of free-standing grids wound from 5 um diameter tungsten wire.
Infrared Phys 19, 437 (1979)

5. T J Parker, C L Mok and W G Chambers
Determination of the complex dielectric response of solids in the far infrared from 4 to 300K by dispersive Fourier transform spectrometry.
IEE Conference Publication No. 177, 207 (1979)

6. J A Beunen, A E Costley, C L Mok, G F Neill, T J Parker and G Tait
Performance of free-standing grids wound from 10 um diameter tungsten wire at millimetre and submillimetre wavelengths: computation and mesurement.
To be published in J. Opt. Soc. Am. 71, Feb. 1981

7. C L Mok, T J Parker and W G Chambers
Experimental determination of the Self-energy of the Transverse Optic Mode in KBr at 100 and 300K.
Solid State Comm 34, 567 (1980)